UNIVERSITAT POLITÈCNICA DE CATALUNYA BARCELONATECH

Computational analysis of ion cyclotron resonance frequency heating for JET experiments

Dani Gallart Escolà

ADVERTIMENT La consulta d'aquesta tesi queda condicionada a l'acceptació de les següents condicions d'ús: La difusió d'aquesta tesi per mitjà del repositori institucional UPCommons (http://upcommons.upc.edu/tesis) i el repositori cooperatiu TDX (http://www.tdx.cat/) ha estat autoritzada pels titulars dels drets de propietat intel·lectual **únicament per a usos privats** emmarcats en activitats d'investigació i docència. No s'autoritza la seva reproducció amb finalitats de lucre ni la seva difusió i posada a disposició des d'un lloc aliè al servei UPCommons o TDX. No s'autoritza la presentació del seu contingut en una finestra o marc aliè a UPCommons (*framing*). Aquesta reserva de drets afecta tant al resum de presentació de la tesi com als seus continguts. En la utilització o cita de parts de la tesi és obligat indicar el nom de la persona autora.

ADVERTENCIA La consulta de esta tesis queda condicionada a la aceptación de las siguientes condiciones de uso: La difusión de esta tesis por medio del repositorio institucional UPCommons (http://upcommons.upc.edu/tesis) y el repositorio cooperativo TDR (http://www.tdx.cat/?locale-attribute=es) ha sido autorizada por los titulares de los derechos de propiedad intelectual **únicamente para usos privados enmarcados** en actividades de investigación y docencia. No se autoriza su reproducción con finalidades de lucro ni su difusión y puesta a disposición desde un sitio ajeno al servicio UPCommons No se autoriza la presentación de su contenido en una ventana o marco ajeno a UPCommons (*framing)*. Esta reserva de derechos afecta tanto al resumen de presentación de la tesis como a sus contenidos. En la utilización o cita de partes de la tesis es obligado indicar el nombre de la persona autora.

WARNING On having consulted this thesis you're accepting the following use conditions: Spreading this thesis by the institutional repository UPCommons (http://upcommons.upc.edu/tesis) and the cooperative repository TDX (http://www.tdx.cat/?locale-attribute=en) has been authorized by the titular of the intellectual property rights **only for private uses** placed in investigation and teaching activities. Reproduction with lucrative aims is not authorized neither its spreading nor availability from a site foreign to the UPCommons service. Introducing its content in a window or frame foreign to the UPCommons service is not authorized (framing). These rights affect to the presentation summary of the thesis as well as to its contents. In the using or citation of parts of the thesis it's obliged to indicate the name of the author.

Computational Analysis of Ion Cyclotron Resonance Frequency Heating for JET Experiments

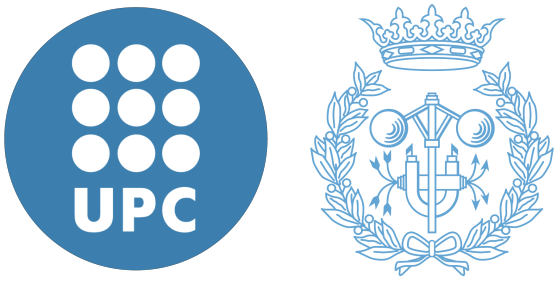

Dani Gallart Escolà

Director
Prof. Mervi Johanna Mantsinen
Co-director
Prof. Lluís Batet Miracle

Department of Physics
Universitat Politècnica de Catalunya

This dissertation is submitted for the degree of
PhD in Nuclear and Ionising Radiation Engineering

ETSEIB

September 2019

Per a Núria.
Per als meus pares, Ramon i M. Goretti.
Per a tots aquells que creuen que un món millor és possible.

Declaration

I hereby declare that except where specific reference is made to the work of others, the contents of this dissertation are original and have not been submitted in whole or in part for consideration for any other degree or qualification in this, or any other university. This dissertation is my own work and contains nothing which is the outcome of work done in collaboration with others, except as specified in the text and Acknowledgements.

Dani Gallart Escolà
September 2019

Acknowledgements

Canada Bill was probably the greatest hustler of all time, it might not be the nicest of the professions but it surely reported him lots of benefits. However, the reason why I am introducing this not so well-known gentleman is because he once said in a poker game "*I know it's crooked, but it's the only game in town*", of course one might make many interpretations of this sentence, all of them valid, but for me it was *one of these sentences*. The underlying meaning that I assumed is that one will pursuit his own goal, no matter what. For me, the goal was the text that you are now reading, a contribution in a field with the potential to change the way we live. Nuclear fusion is with no doubt such a field and I hope that this thesis which is nothing more than a small gear in a huge machinery helps in reaching the promised ultimate source of energy.

What I have learned during these four years is that nothing is done alone and that big projects need collective efforts, the first person that deserves a big *thank you* is Mervi Mantsinen, she has invested a lot of time in me and has led me in the right direction during these years, I realise how lucky I have been, *kiitos* Mervi. I want also to thank Lluís Batet for his valuable advice and the PhD sectretary Olga López for helping me with the bureaucracy all along this time. During these years I have met lots of interesting and truly smart people that somehow inspired me even when things were getting not so well and I cannot help but think that it is a bit unfair that I do not mention all of them but in this way I can disguise my bad memory. However, I want to have a special mention for some people that have always shown to be helpful when I had doubts or needed an additional opinion, thank you, Dirk van Eester, Ernesto Lerche, Yevgen Kazakov, Thomas Johnson, Ruben Otín, Joelle Mailloux and Henri Weisen. I would also like to specially thank Prof. Jean-Marie Noterdaeme and Prof. Jozef Ongena for their precious comments and carefully reading this thesis.

Els últims agraïments dins el món de la fusió són per a en Jerónimo García i en Josep Maria Fontdecaba, curiosament els dos catalans (n'he conegut poquíssims dins la fusió), amb el primer he tingut la sort de treballar-hi i publicar conjuntament i amb

el segon, no sé què faria sense ell quan vaig a JET... però el cert és que els menciono aquí pels bons moments que hem passat junts.

Finalment els agraïments més importants són per a la família i els amics. Aquí tampoc anomenaré a tothom perquè per fortuna és una llista molt llarga, però sí m'agradaria que tinguéssiu present que hi pertanyeu especialment els amics *de tota la vida*, els de la facultat, els de l'oficina i per suposat la meva família, germans, germana, pares i a aquells que considero els segons pares. No puedo terminar estos agradecimientos sin nombrar a mi hermano Ramon M. Gallart y a Garri, ellos han sido las figuras científicas más cercanas que he tenido desde pequeño y al final una persona es lo que es por la gente que le rodea, estoy seguro que mi interés por la ciencia empezó con ellos y entre *macarrones*, moltes gràcies. I ja només queda una última persona, m'agrada pensar que és la meva pedra angular, aquella pedra que s'adapta on sigui i quan sigui, sense tu aquest viatge com tants d'altres no hagués estat possible, gràcies Núria Guillem.

I would like to thank 'la Caixa' for the financial support to my PhD studies during these four years. I would also like to mention Fusenet which has funded some of my summer schools. This work has received funding from the Spanish Ministry of Economy and Competitiveness (MINECO) under grant ENE2015-67371-R. I would like to thank EUROfusion, the European consortium for fusion energy which has made all my trips to JET and AUG possible. Special thanks to the Severo Ochoa mobility and the Argos grants that made some of my trips for conferences and collaboration possible.

Abstract

Heating plasmas to a relevant fusion temperature is one of the key aspects of magnetically confined fusion plasmas. Radio frequency (RF) heating with electromagnetic waves in the ion cyclotron range of frequencies (ICRF) has been proven to be an efficient auxiliary method in present fusion devices such as tokamaks. Moreover, the International Thermonuclear Experimental Reactor (ITER) will be provided with ICRF antennas as one of the main heating mechanisms. Therefore, the study of different heating schemes to optimise the fusion performance is of utmost importance.

During the 2015-2019 Joint European Torus (JET) campaigns many efforts have been devoted to the exploration of high-performance plasma scenarios envisaged for D-T operation in JET. Experiments in D, H and T are expected to lead in 2020 to the first experiments with 50%:50% D-T mixtures. These last campaigns at JET have been focused on enhancing the fusion performance of the baseline and hybrid scenarios with the final goal of improving ITER's future operation. This thesis reports on the modelling study of plasma heating through ICRF waves and NBI for recent experiments at JET with special emphasis on plasma performance.

The modelling has been performed mainly with the ICRF code PION. Simulations are in excellent agreement with experimental results which proves the reliability of the results shown in this thesis. The assessment of the results offer an overview to understand and optimise plasma performance for high-performance hybrid discharges that were performed with D plasma and H minority.

Impurity accumulation control with ICRF waves was found to be efficient only for a range of central resonance locations while impurity accumulation occurred for off-axis resonance. Contribution to temperature screening from fast ions was calculated to be negligible when finite orbit widths (FOW) are taken into account, as opposed to previous studies that did not take into account FOW. Small differences in H concentration have a large impact on power partition between H and D. The lower the H concentration the larger the power channeled to D which is shown to substantially enhance the D-D fusion rate. The study of a neutron record high-performance discharge shows

high bulk ion heating and low H concentration as key ingredients for increased fusion performance.

Of especial relevance for ITER is the study of the D-T prediction from high-performance discharges. This analysis compares two ICRF schemes, H and ^{3}He minority. It is shown that ^{3}He is a strong absorber and provides higher bulk ion heating as compared to H. However, ICRF fusion enhancement is computed to be larger with H minority heating, as this scheme has stronger 2nd D harmonic heating as compared to the 2nd T harmonic heating of the ^{3}He scheme. In D-T, the neutron rate enhancement due to ICRF is computed to be significantly lower with regards to D-D plasmas due to different fusion cross sections. Results in preparation of the T and D-T campaigns at JET show that the extrapolation from T to D-T plasmas is not straightforward. PION predicts the T density to have a large impact on the T velocity distribution function for the ITER relevant 2nd T harmonic heating scheme. The results show that larger concentrations of T lead to higher bulk ion heating. The velocity distribution function of T in 50%:50% D-T plasmas show lower values around the critical energy as compared to the T case, resulting in a lower bulk ion heating.

Table of contents

List of figures

List of tables

Nomenclature

Convention

$\vec{x}$	Vector of x
$\bar{x}$	Tensor of x
$\mathbf{x}$	Volume of $\mathbf{x} = x_i x_j x_k$

Greek Symbols

ε_0	$\simeq 8.85 \cdot 10^{-12}\ Fm^{-1}$ Vacuum permittivity
ε	$= \varepsilon_r \varepsilon_0\ Fm^{-1}$ Absolute permittivity
i	$= \sqrt{-1}$ Unit imaginary number
μ_0	$\simeq 4\pi \cdot 10^{-7}\ Hm^{-1}$ Magnetic permeability
μ	$= \mu_r \mu_0\ Hm^{-1}$ Absolute magnetic permeability
π	$\simeq 3.14$
r_L	Larmor radius
ω_c	Cyclotron frequency

Acronyms / Abbreviations

$DEMO$	DEMOnstration Power Plant
$ECRH$	Electron Cyclotron Resonance Frequency Heating
ELD	Electron Landau Damping
FOW	Finite Orbit Widths

HFS High-Field Side

ICF Inertial Confinement Fusion

$ICRF$ Ion Cyclotron Range of Frequencies

$ICRH$ Ion Cyclotron Resonance Frequency Heating

$ITER$ International Thermonuclear Experimental Reactor

JET Joint European Torus

LFS Low-Field Side

$LHCD$ Lower Hybrid Current Drive

MC Mode Conversion

MHD Magnetohydrodynamics

NBI Neutral Beam Injection

NTM Neoclassical Tearing Mode

RF Radio Frequency

$TTMP$ Transit Time Magnetic Pumping

Foreword

This is an introduction on the thesis itself rather than on fusion energy concepts. Here, a motivation for this work is given, together with a related publication list and a brief description of the contributions and structure of the thesis.

The energy crisis that we are presently facing is the main driving force in the search for a robust, clean and durable source of energy. Together with the environmental impact that fossil fuels represent, it is clear that a solution to this problem needs to be sought. Fusion energy is a firm candidate to become the future energy source. Several approaches are being investigated to make the process of nuclear fusion an energy source. One of the main and most promising approaches is the tokamak, a fusion device that confines plasma at a high temperature using strong magnetic fields. Reaching high temperatures (millions of K) is essential in order to maximise the fusion cross section, i.e., maximise the number of fusion reactions.

A number of experiments in tokamaks are being developed all around the world. In particular, the International Thermonuclear Experimental Reactor (ITER), which is being built in the south of France, Cadarache, will be the first fusion device to confirm the capability of fusion to provide $Q = \frac{P_{out}}{Pin} = 10$, where P_{out} is the fusion power obtained and P_{in} is the input power to fully operate the experimental reactor. In preparation for ITER experiments, the Joint European Torus (JET) located in Culham, United Kingdom, which is presently the biggest tokamak worldwide, has been upgraded with a plasma wall similar to that of ITER (ITER-like-wall). Recently, several campaigns have been carried out in JET to provide a solid scientific support to guide experiments in ITER. Most importantly, a campaign in deuterium-tritium (D-T), which is the plasma composition that needs to confirm ITER's goals, will be performed in JET. Special attention has been given to plasma performance, i.e., maximise the number of fusion reactions and what is called the high-performance phase of the discharge by avoiding impurity accumulation and MHD activity.

This thesis tackles the heating of a fusion plasma in a tokamak using electromagnetic waves and neutral beams from the experimental and computational points of view.

The research is based on the last JET campaigns where, as mentioned, a special focus was given to plasma performance optimisation and assessment. In order to reach high-performance conditions it is of utmost importance to understand how different heating schemes will impact the plasma performance. The optimisation of such schemes is one of the main research tasks, i.e., to couple the wave energy in such a way that nuclear fusion reactions are maximised. This is a non-trivial task since many parameters play a role in the ways in which the wave energy is damped and the velocity distribution of resonant ions evolves during the process. This analysis serves as a guide to carry out future experiments at JET and eventually, to improve ITER's scenarios performance.

Contributions

This thesis has contributed in a number of aspects in the field of plasma heating and its effects on fusion performance and its optimisation. The following list summarises these contributions:

- First analysis of the temperature screening provided by fast ions using finite orbit width effects. The temperature sceening is the prevention of central impurity accumulation by peaking the central temperature profile of electrons (or ions). The result is that their contribution is much lower than it was thought in previous studies.

- Analysis of the impact of resonance position in central impurity accumulation. Central heating is the best scheme to avoid central impurity accumulation.

- Comprehensive analysis on the optimisation of neutron yield in deuterium (D) plasmas by changing the ICRH-heated minority ion concentration and studying the ICRF+NBI synergy.

- Study the impact of ICRF fusion rate enhancement in high-performance discharges in deuterium and its prediction to deuterium-tritium (D-T) discharges.

- Assessment of the integrated modelling of a high-performance discharge using two ICRF schemes with hydrogen and ^{3}He minority ions and its D-T prediction.

- Modelling of the heating differences between T and D-T plasmas and its impact in the velocity distribution of resonant ions.

List of publications

This thesis is based on the work carried out in the following papers.

Journal

- **Publication 1. D. Gallart**, et al., *Modelling of JET hybrid plasmas with emphasis on performance of combined ICRF and NBI heating*, Nuclear Fusion **58** 106037, 2018.
- **Publication 2. D. Gallart**, et al., *Modelling of combined ICRF and NBI heating in JET hybrid plasmas*, European Physical Journal **157**, 03015, 2017.
- **Publication 3.** M.J. Mantsinen, et al. (including **D. Gallart**), *The Role of Combined ICRF and NBI Heating in JET Hybrid Plasmas in Quest for High D-T Fusion Yield*, European Physical Journal **157**, 03032, 2017.
- **Publication 4.** J. Garcia, C. Challis, **D. Gallart**, et al., *Challenges in the extrapolation from DD to DT plasmas: experimental analysis and theory based predictions for JET-DT*, Plasma Physics and Controlled Fusion **59**(1), 014023, 2016.
- **Publication 5.** J. Garcia, et al. (including **D. Gallart**), *First principles and integrated modelling achievements towards trustful fusion power predictions for JET and ITER*, Nuclear Fusion **59**(08) 6047, 2019.
- **Publication 6. D. Gallart**, et al., *Modelling of ICRF heating for JET T and D-T plasmas*, submitted to AIP 2019.

Conference proceedings

- **D. Gallart**, et al., *Simulations of combined ICRF and NBI heating for high fusion performance in JET*, Europhysics Conference Abstracts vol **40A** P2.003 (http://ocs.ciemat.es/EPS2016PAP/pdf/P2.003.pdf), 2016.
- M.J. Mantsinen, **D. Gallart**, et al., *Optimising the use of ICRF waves in JET hybrid plasmas for high fusion yield*, Europhysics Conference Abstracts vol **41F** O3.110 (http://ocs.ciemat.es/EPS2017PAP/pdf/O3.110.pdf), 2017.
- **D. Gallart**, et al., *Heating modelling and extrapolation of hybrid plasmas at JET*, XXXVI Biennial Meeting of the Real Sociedad Española de Física, 2017.

- **D. Gallart**, et al., *Extrapolations of the fusion performance in JET*, 3rd BSC Severo Ochoa Doctoral Symposium (URI: http://hdl.handle.net/2117/90991), Barcelona, 2016.

- **D. Gallart**, et al., *On the quest to reach nuclear fusion as a future energy source*, 5th BSC Severo Ochoa Doctoral Symposium (URI: http://hdl.handle.net/2117/124930), 2018.

Other publications

Throughout the completion of this thesis I had the opportunity to collaborate with people studying topics that are not strictly related with this work. This is a publication list of these collaborations that do not appear in the text.

- Ye.O. Kazakov, et al. (including **D. Gallart**), *Efficient generation of energetic ions in multi-ion plasmas by radio-frequency heating*, Nature Physics **13**, 973-978, 2017.

- S.E. Sharapov, et al. (including **D. Gallart**), *The effects of electron cyclotron heating and current drive on toroidal Alfvén eigenmodes in tokamak plasmas*, Plasma Physics and Controlled Fusion **60**(1), 014026, 2017.

- H. Meyer, et al. (including **D. Gallart**), *Overview of progress in European medium sized tokamaks towards an integrated plasma-edge/wall solution*, Nuclear Fusion **57**(10), 102014, 2017.

- X. Litaudon, et al. (including **D. Gallart**), *Overview of the JET results in support to ITER*, Nuclear Fusion **57**(10), 102001, 2017.

- N. Bonanomi, et al. (including **D. Gallart**), *Role of fast ion pressure in the isotope effect in JET L-mode plasmas*, Nuclear Fusion **59**(09) 6030, 2019.

- M.J. Mantsinen, V. Bobkov, **D. Gallart**, et al., *Third harmonic ICRF heating of deuterium beam ions on ASDEX Upgrade*, Europhysics Conference Abstracts vol **40A**, P1.035 (http://ocs.ciemat.es/EPS2016PAP/pdf/P1.035.pdf), 2016.

- M.J. Mantsinen, V. Bobkov, **D. Gallart**, et al., *Modelling of ICRF heating in ASDEX Upgrade discharges with pure wave heating relevant to the ITER baseline scenario*, Europhysics Conference Abstracts vol **42A**, P1.1072, 2018.

- F.N. de Oliveira, et al. (including **D. Gallart**), *Nonlinear electromagnetic stabilisation of ITG microturbulence by fast ions in ASDEX Upgrade*, to be submitted to Nuclear Fusion, 2019.

Seminar/Oral presentations

- Modelling of ICRF heating for JET T and D-T plasmas *Task Force Meeting at JET* 30/04/2019.
- ICRH modelling for high-performing hybrid and baseline scenarios: from TT to DT - *Task Force Meeting at JET* 12/03/2019.
- Modelling of ICRF in JET hybrid scenario and prediction for DT - *Seminar at Commissariat à l'énergie atomique et aux énergies alternatives (CEA)* 10/07/2018.
- Modelling of combined ICRF and NBI Heating in JET Hybrid Plasmas - *Task Force Meeting at JET* 23/05/2017.
- On the quest to reach nuclear fusion as a future energy source, *5th BSC Severo Ochoa Doctoral Symposium* 25/04/2018

Stays at JET

I have been actively involved in the Joint European Torus (JET) campaigns since the beginning of my PhD in 2015. During this time, I have made 12 stays for a total of 136 days at the Culham Centre for Fusion Energy (CCFE) through the EUROfusion consortium. EUROfusion is the European consortium that manages fusion research in Europe.

My stays had two different purposes, as scientific participation in JET experiments and as scientific participation in the analysis and modelling of JET experiments. My participation in JET experiments has been carried out through the analysis and modelling of plasma heating with radio frequency (RF) waves and neutral beam injection (NBI). This modelling provides necessary information to set up further experiments at JET and to understand the physics involved.

I have worked mainly in the development of the hybrid scenario for D-T experiment and I am currently involved in 5 experiments. I have also worked in the D-T extrapolation task where we have performed several predictions for the forthcoming D-T campaign at JET during my PhD.

Thesis outline

The thesis is structured in eight chapters. Each chapter is self-contained, i.e., it gives an introduction, the analysis of the results and a conclusion for a specific problem or physical concept. The underlying idea to organise the chapters is that each of them introduces a different concept. Chapter 1 is an introduction to fusion energy and gives an overview for the not so expert reader. Chapter 2 explains briefly the physics of electromagnetic propagation in a plasma and shows how to obtain the dielectric tensor in the cold plasma model. Chapter 3 describes the mathematical model of the main code used in this thesis, the ICRF code PION. From chapter 4 to chapter 7 the results obtained are described. Chapter 4 is an explanation of the effects of ICRF to central impurity accumulation, chapter 5 describes the effect of minority concentration on plasma performance and the impact of ICRF enhancement in neutron yield with emphasis on ICRF+NBI synergy. Chapter 6 extrapolates results from a high-performance discharge to the maximum external heating power available at JET for a D and a D-T plasma. Chapter 7 models the future T and D-T discharges at JET making a particular emphasis on the expected heating differences. Finally, chapter 8 is a summary of the overall work carried out in this thesis.

Chapter 1

Fusion energy

This chapter serves as an introduction to the nuclear fusion process. It is intended to give the reader a basic notion of what a plasma is and an overview of how the so-called tokamak fusion device works. If the reader is already familiar with these concepts he/she might consider skipping this chapter.

1.1 A note on world energy consumption

Energy is the cornerstone of our society. Such is the prevalence and importance of energy that the lack or inability to sustain the increasing supply demands would constitute a complete collapse of our society. Since the present world energy supply is mainly covered by fossil fuels, it is necessary to find other alternatives capable of providing the same power load [1, 3]. This necessity lies on two facts, first, the limited number of fossil fuel sources and, second, its environmental impact due to green-house gases.

Therefore, it is necessary to find a solution to the energy issue before the energy supply capacity becomes unable to meet the increasing energy demand or the fossil fuels' environmental impact becomes no longer acceptable. Renewable energies such as solar and wind energies could be a plausible solution. However, their dependence on weather forecast and their lack of robustness in terms of power load makes the study of other alternatives necessary. In this regard, nuclear power is a promising candidate. In fact, fission nuclear power has been offering a substantial amount of energy since the 1960s and has demonstrated its capacity to provide energy to a whole country such as France. Nevertheless, the production of long term radioactive wastes and some major accidents such as Three mile island, Chernobyl or more recently Fukushima have

forced some countries, for example Germany, to take drastic actions such as closing their nuclear power plants.

The other nuclear energy option is the so-called fusion energy. Fusion offers the capacity to provide society with a robust power load, a virtually unlimited source of energy and free of green-house gases and radioactive wastes. Moreover, the safety of such power plants would be guaranteed since a fusion reactor needs to be constantly fuelled as opposed to a fission nuclear power reactor which contains all the fuel until it is consumed. Unfortunately, fusion energy supply is still not yet a reality. This thesis aims at making fusion energy one step closer of becoming a readily accessible energy source.

1.2 The nuclear fusion reaction

One of the main interests in nuclear engineering is the amount of energy released per nuclear reaction. In chemical reactions such as burning fossil fuels like gasoline, the typical energy provided is around 1 eV per atom while in nuclear reactions becomes 1 MeV per nucleon, i.e. 10^6 times higher [1]. This is the strength of nuclear reactions as a source of energy. In a nuclear fusion reaction several nuclei undergo a process, typically through collisions, by which they form a single heavier nucleus. If the process occurs for elements with an atomic number below $Z < 26$ the process is said to be exothermic, i.e. delivers energy in form of kinetic energy. This kinetic energy is the result from the mass difference between the initial nuclei that fuse and the final nucleus by applying Einstein's famous equation $E = mc^2$. The mass defect is equal to the energy holding the nucleus together, the so-called binding energy. Therefore, a reaction will be exothermic in those cases where the average binding energy increases. From figure 1.1 it is clear that fusion as a source of energy is only possible for elements lighter than iron while fission is viable for heavier elements.

An example of the fusion process occurring naturally is the nuclear reactions that are taking place in the star's core, starting with hydrogen (H) and finalising with iron (Fe). The star extracts energy from these reactions and maintains in this way a pressure against gravity force which might eventually lead to the whole star's collapse. The moment the initial elements become Fe, the star will be unable to carry on the fusion process since fusion reactions beyond Fe are endothermic. Therefore, the star will start to collapse. This process has several possible endings: from white dwarfs and supernovas to black holes.

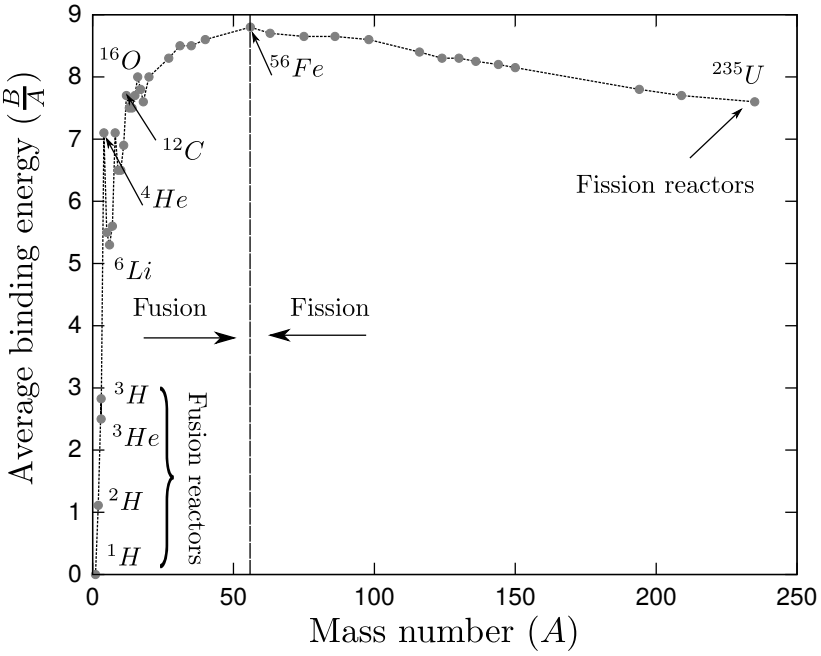

Fig. 1.1 *Average binding energy of elements, showing the fusion and fission exothermic regions.*

This thesis tackles fusion reactions for light nuclei, mainly those of H, deuterium (D=^{2}H) and tritium (T=^{3}H). It is important to notice that H and D are naturally present in sea water and, therefore, the fuel is virtually unlimited. Tritium has a short half-life of around 12.26 years and it is thus necessary to obtain by producing it. Many efforts are being devoted to design blankets, integrated in the reactor first wall, capable of producing T in a fusion reactor by using lithium. The main fusion reaction studied in the Joint European Torus (JET) during the completion of the present thesis was the D-D reaction [2]:

$$D + D \rightarrow \begin{cases} T\ (1.01\ MeV) + p\ (3.02\ MeV) \\ {}^3He\ (0.82\ MeV) + n\ (2.45\ MeV) \end{cases}$$

where the numbers in parenthesis stand for the kinetic energy of the end product particles assuming no kinetic energy from the initial nuclei. There are several other fusion reactions that may occur in a fusion device. However, special emphasis must be given to the D-T reaction,

$$D + T \rightarrow^4 He\ (3.5\ MeV) + n\ (14.1\ MeV).$$

This reaction is intended to be the workhorse for the eventual fusion power plants, not only because of the higher amount of energy delivered as compared to D-D reactions but also because of it being the easiest fusion reaction to be reached. At this point it is necessary to introduce the concept of cross section. These reactions do not occur spontaneously in ambient conditions. The cross section gives information about the probability of a reaction to occur, it is a magnitude in surface units. It is clear from figure 1.2 that the D-T reaction is the easiest fusion reaction to obtain because of two reasons: it has the highest peak and its maximum is located at the lowest energy among the other options, around 100 keV. This difference in fusion cross section between D-D and D-T reactions has an important impact when results from a D-D experiment are extrapolated to D-T, as discussed in chapter 6.

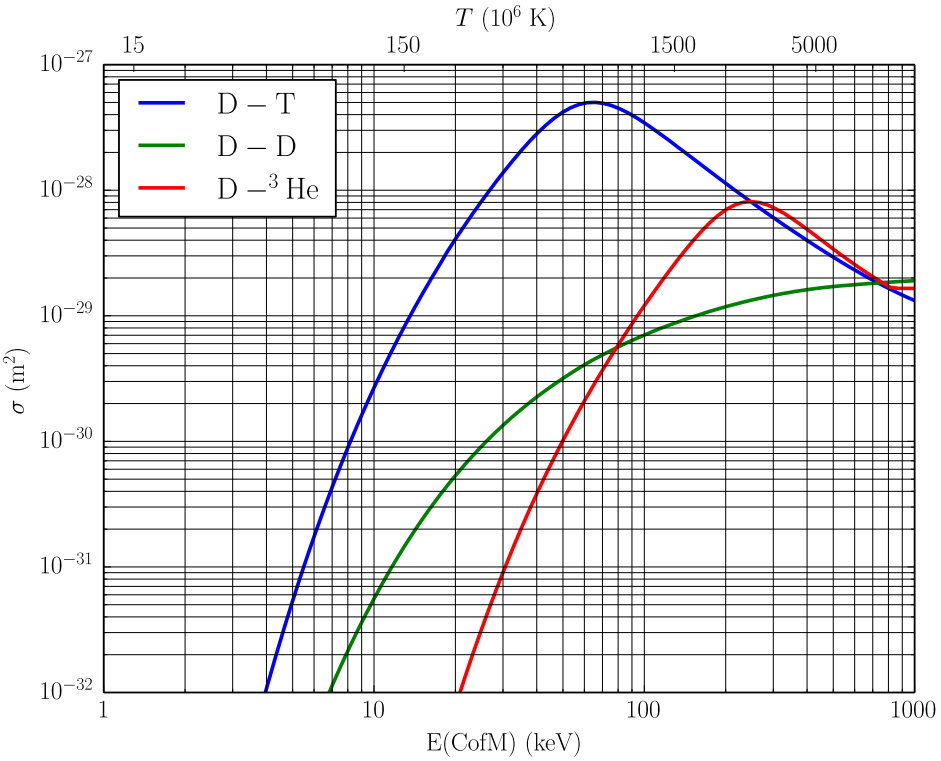

Fig. 1.2 *Fusion cross sections for typical fusion reactions from the centre of mass frame of reference (CofM).*

Fusion energy is environmentally friendly as compared to nuclear fission. For example in the chain reaction happening in the present fission nuclear power plants, where ^{235}U is bombarded with thermalised neutrons, many of the lighter products formed have long half-lifes and are extremely radioactive. However, notice from D-T reactions that no radioactive wastes are produced. Only one of the initial isotopes, T,

being radioactive as it undergoes β-decay but with a short half-life of 12.26 years as mentioned previously. Thus, in contrast with fission energy, fusion provides not only a carbon-free source of energy but also no radioactive wastes apart from the neutron activation of the reactor wall.

1.3 Brief description of a plasma

In figure 1.2 it is clear that in order to reach the maximum of the D-T fusion cross section, a temperature of the order of $1.5 \cdot 10^8$ K needs to be achieved. At such a high temperature, matter and in particular H and its isotopes become fully ionised. This gas of free electrons and nuclei is known as plasma. Plasma is the state of matter in which fusion reactions occur in many fusion devices and specially in the fusion device considered in this thesis (see section 1.4). Therefore, all the physics described in this thesis take into account that matter is in plasma state.

Plasma is typically referred as a state of matter in which a gas has been ionised. However, the ionised gas needs to fulfill a set of further requirements to be considered a plasma. In particular, there are three main parameters that need to be compared with macroscopic properties. These are the Debye length λ_{De}, the plasma frequency ω_{pe} and the plasma parameter Λ_D. These characteristic plasma parameters are defined as [2, 4],

$$\lambda_{De} = \left(\frac{\varepsilon_0 T_e}{e^2 n_0}\right)^{1/2}, \tag{1.1a}$$

$$\omega_{pe} = \left(\frac{n_0 e^2}{m_e \varepsilon_0}\right)^{1/2}, \tag{1.1b}$$

$$\Lambda_D = \frac{4\pi}{3} n_e \lambda_{De}^3. \tag{1.1c}$$

The characteristic lenght λ_{De} and the characteristic inverse time ω_{pe} of a plasma are related to the ability of the plasma to shield out external DC and AC electric fields as a result of its high conductivity. For that to occur the Debye length needs to be much smaller as compared to the device dimensions, i.e. $\lambda_{De} << L$. Additioanlly, the plasma frequency has to be much higher than any of the characteristic frequencies in a plasma. If compared with the inverse thermal transit time of an electron $\omega_{pe} >> v_{Te}/L$ this is equivalent to the previous statement. Finally, the last requirement is that the plasma parameter $\Lambda_D >> 1$. From the definition in equation 1.1c this means that many particles need to be located in a sphere of radius λ_{De}. This condition needs to

be fulfilled for a plasma to be dominated by long range collective effects instead of collisionality effects.

These are the main requirements that define a general plasma. However for specific plasmas such as a fusion plasma, there exist other requirements. In any case, if an ionised gas is unable to meet any of this requirements, it cannot be considered a plasma.

1.4 Magnetic confinement fusion

In this thesis the focus is given to magnetic confinement fusion. For other techniques such as Inertial confinement fusion (ICF) refer to Ref.[5]. By using the fact that a plasma is a good conductor, confinement is achieved by applying a magnetic field. The Lorentz force will cause ions and electrons to spin around the magnetic field lines and thus being effectively confined by a force perpendicular to their velocity. Their trajectory in cylindrical coordinates is given by

$$\begin{aligned} \vec{z} &= (v_{\parallel}t)\hat{z} \\ r_{\perp} = r_c\hat{\rho} &= \frac{v_{\perp}}{\omega_c}\cos(\omega_c t+\phi)\hat{i} + \frac{v_{\perp}}{\omega_c}\sin(\omega_c t+\phi)\hat{j}, \end{aligned} \tag{1.2}$$

where $v_{\parallel}$ is the parallel velocity to the magnetic field, ϕ is an arbitrary phase angle and the cyclotron radius and the cyclotron frequency are defined as,

$$r_c = \frac{v_{\perp}}{\omega_c} \tag{1.3a}$$

$$\omega_c = \frac{ZeB}{Am_p}, \tag{1.3b}$$

respectively. A scheme of this motion is presented in figure 1.3.

Both electrons and ions obey equation 1.2. However, they rotate in opposite directions as they have different charge signs. Early approaches for magnetic confinement fusion devices such as the mirror effect or the z-pinch were found to be very leaky in the sense that many particle losses occurred at the endings of these devices. A solution to address this issue was found with the advent of toroidal fusion devices such as the tokamak (axial symmetry) [2] and the stellarator (non axial symmetry) [6] where due to their toroidal topology the magnetic field lines cover the whole machine with no endings. The tokamak (figure 1.4) is a symmetric toroidal fusion device which is composed by an array of toroidal magnets that produce a constant magnetic toroidal field B_T inside the vacuum vessel and a central solenoid that induces a plasma current

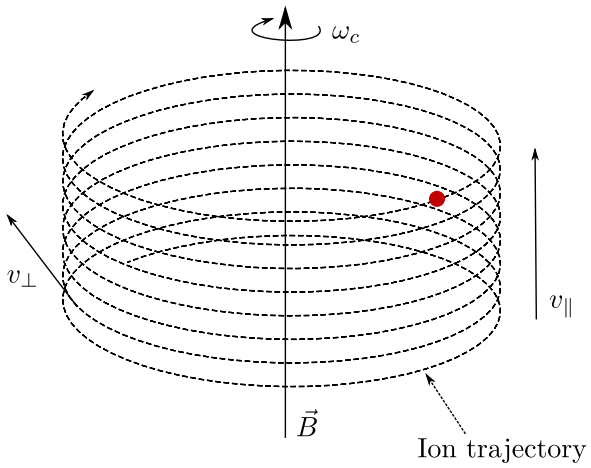

Fig. 1.3 *Cyclotron motion of an ion under Lorentz force produced by a magnetic field.*

I_p which in turn produces a poloidal magnetic field B_θ forming a helical magnetic field line, where $B_\theta << B_T$. This magnetic field shape is able to confine plasma and keep radial equilibrium by avoiding vertical drifts, charge separation and resulting radial drifts. Due to geometry effects, i.e. due to the fact that the toroidal magnets are closer at the centre of the torus than at the edge, the toroidal magnetic field decreases as it approaches the outer edge as $B_T \propto \frac{1}{R}$ where R is the radial distance from the torus axis. Furthermore, there exist several particle drifts related to various effects such as the gradient of the magnetic field ∇B or the existence of electric fields. They make confinement more complicated than as explained here. For more information refer to [1, 2].

As opposed to tokamaks, stellarators (figure 1.5) have no axial symmetry and no central solenoid as no induced plasma current is needed. Many instabilities related to plasma current are avoided in stellarators and their operation is not limited by the pulse time as in tokamaks. The final goal of a stellarator is to confine particles by bending the magnetic field lines with twisted coils that produce a helical magnetic field around the torus.

The main fusion device modelled in this thesis is the tokamak and at the time of writing this thesis the tokamak concept is the leading candidate to become the world's first fusion reactor due to its better performance as compared to other concepts. This is mainly because of the values reached in plasma pressure and energy confinement time $p\tau_E$ at high temperatures.

The goal of fusion research is to achieve $Q > 1$, where the Q-factor measures the ratio of input (net power into plasma) to output (total fusion power) power in a fusion device. At the moment fusion devices are getting closer to breakeven conditions, i.e.,

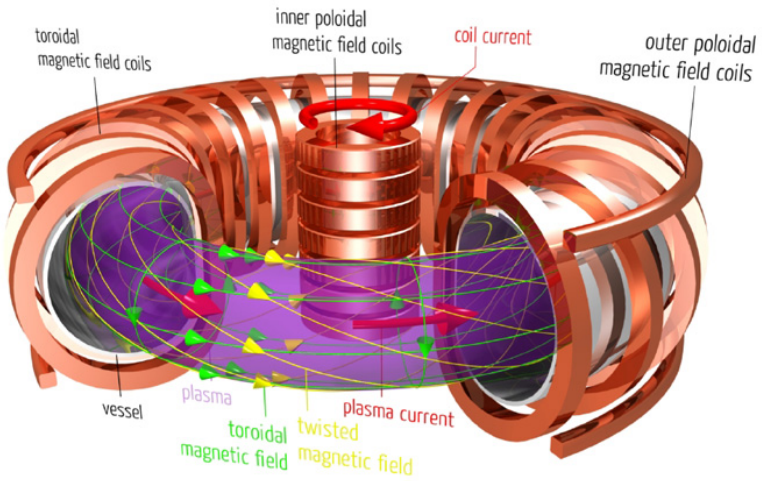

Fig. 1.4 *Main scheme of a tokamak. Courtesy of Max-Planck Institute for Plasma Physics.*

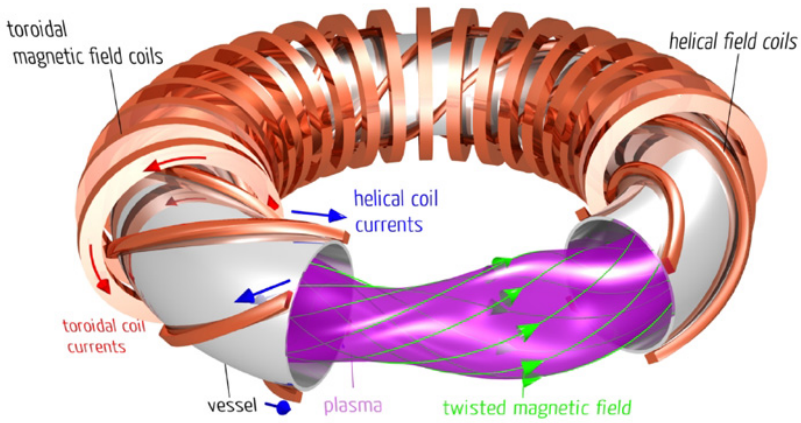

Fig. 1.5 *Main scheme of a stellarator. Courtesy of Max-Planck Institute for Plasma Physics.*

$Q = 1$. The ignition condition $Q \to \infty$ where no external energy is needed to maintain the fusion process is not a main goal as keeping some external power is beneficial for control purposes [7]. In this regard, the construction process of the International Thermonuclear Experimental Reactor, ITER, is being finalised in Cadarache, south of France. ITER is the result of a large international effort to make fusion a reality. This new fusion machine is designed to reach $Q > 10$. The next step is to build a DEMOnstration Power Plant, DEMO, which will be the first fusion device producing

electricity after the expected success of ITER. For a review of past achievements and present efforts in magnetic confinement fusion refer to Ref. [8].

The author of this thesis has worked very closely and devoted this thesis to the Joint European Torus (JET) in Culham, UK, which is presently the biggest experimental fusion experiment (see 1.7).

1.5 Basic parameters of a tokamak

The fundamental parameters of a tokamak are described and displayed in table 1.1 for DEMO, ITER and JET. Notice the difference in size between the largest, DEMO and the smallest JET, since the approach adopted to increase the fusion power in ITER and DEMO is to increase the geometrical size. Nevertheless, there exist other approaches such as increasing the magnetic field but this is limited by technological constraints for high superconducting magnets. Fusion power scales as [9],

$$P_{fus} = c_{fus} \frac{\beta_N^2 B^4 R^3}{q^2 A^4} \tag{1.4}$$

where β_N is the normalized plasma pressure to magnetic pressure, B is the magnetic field, R is the toroidal radius, q is the safety factor and A is the aspect ratio.

Parameter	DEMO[1]	ITER	JET
Major radius R_0 (m)	9.25	6.2	2.96
Minor radius r (m)	2.64	2	1.25-2.10
Toroidal magnetic field B (T)	6.8	5.3	3.45
Plasma current Ip (MA)	18.6	15	4.8
Safety factor q_0	1.1	1.0	1.0
Safety factor q_{95}	3	3.5	5.0
Elongation κ	1.52	1.7	1.68
Triangularity δ	0.33	0.33	0.4
Plasma volume (m^3)	2009	831	100
Fusion power (MW)	2119	400-500	16
Electric output power	500	-	-

Table 1.1 DEMO, ITER and JET parameters [1, 2].

[1]We are grateful to Dr. T. Franke and Dr. R. Wenninger (PPPT, Garching) for DEMO parameters. They are for the EU DEMO design optimised for a maximum pulse length of 2.3 hrs (with CD 2.7hrs)

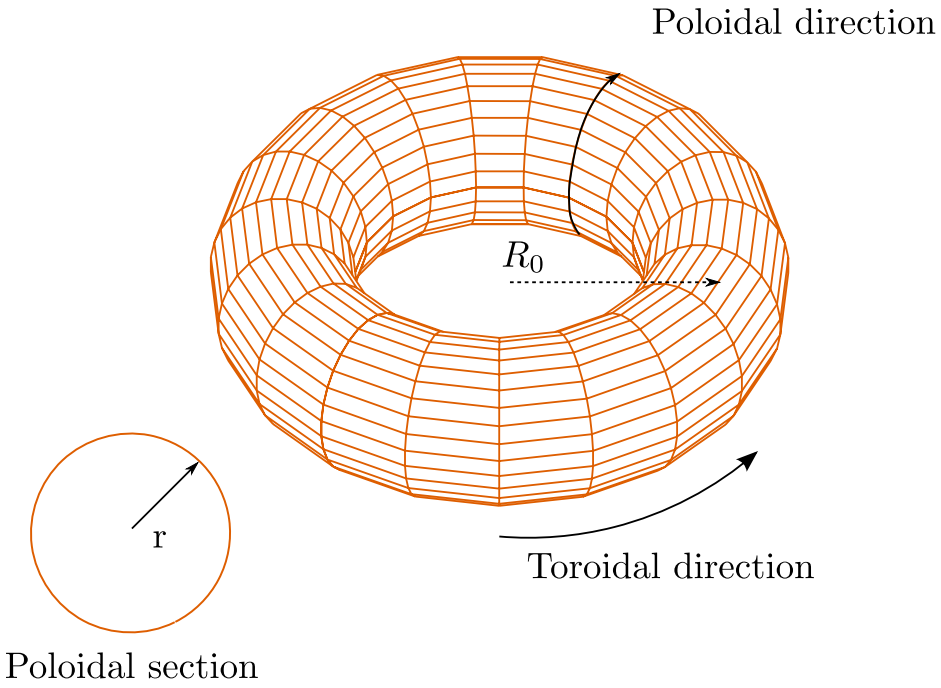

Fig. 1.6 *Simplified tokamak geometry.*

The major radius R_0 is the radial distance from the center of the tokamak to the center of the poloidal section. The minor radius is the radial distance from the center of the poloidal section to the surface of the torus (figure 1.6). In fact, the actual geometry of the poloidal section is not circularly shaped but D-shaped (figure 1.7). First tokamaks had circular sections but plasma physics showed that D-shaped sections lead to a better performance improving turbulence in the plasma. Elongation and triangularity are two parameters that arise from D-shape poloidal sections. Elongation is the ratio between both minor radii (figure 1.7),

$$\kappa = \frac{b}{a}, \tag{1.5}$$

triangularity is the ratio of the difference between the major and top radii R_{top} and the minor radius a,

$$\delta = \frac{R_0 - R_{top}}{a}. \tag{1.6}$$

The safety factor is the inverse of the rotational transform: the rotational transform is defined as the mean number of toroidal cycles (m) over the poloidal cycles (n),

$$q = \frac{d\phi}{d\theta} \simeq \frac{rB_t}{RB_p}. \tag{1.7}$$

Here, ϕ is the toroidal angle and θ is the poloidal angle, B_t is the toroidal magnetic field and B_p is the poloidal magnetic field generated by the current I_p. The safety factor needs to have a value higher than 2 at the edge of the plasma surface, typically at the flux surface that encloses the 95% of the plasma. If not, the plasma is magnetohydrodynamically unstable.

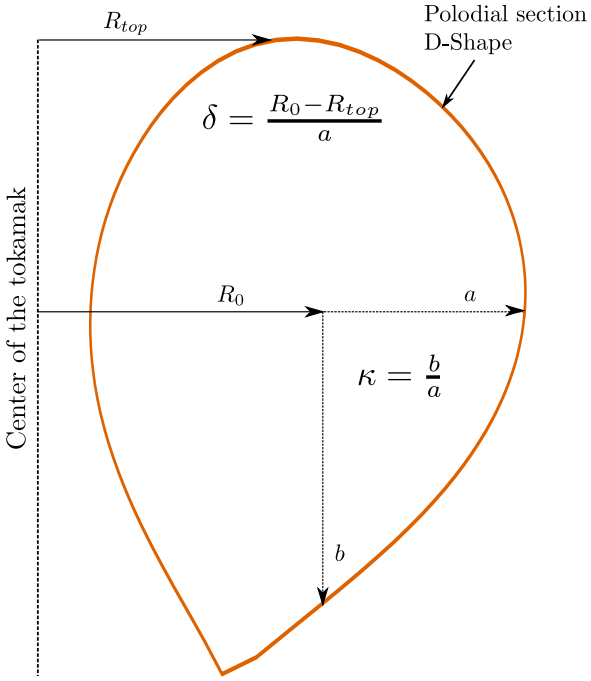

Fig. 1.7 *Detail of the D-shape poloidal cross section.*

1.6 Plasma heating methods

As shown in section 1.3, the cross section of fusion reactions makes plasma heating necessary in order to make fusion a viable source of energy. There are several mechanisms to heat the plasma. Ohmic heating alone, i.e., the joule effect due to the induced current in the plasma, is not enough to reach the necessary temperatures in tokamaks. Plasma resistivity decreases rapidly with electron temperature effectively limiting ohmic heating, following the Spitzer resistivity [10],

$$\eta = \frac{\pi Z e^2 m_e^{1/2} ln\Lambda}{(4\pi\varepsilon_0)^2 (k_B T)^{3/2}}, \tag{1.8}$$

where $ln\Lambda$ is the Coulomb logarithm. Therefore, auxiliary heating methods become necessary. The so-called neutral beam injection (NBI) and radio-frequency (RF) heating

systems have been developed in order to further increase the plasma temperature. The neutral beam injection consists of launching beams of neutrals (so they are not affected by the magnetic field), typically H, D or T at a high energy, which in JET it is typically of the order of 100 keV. The range of beam energies varies with the size of the machine. The energy must be high enough as to have good penetration and reach the plasma core. Radio frequency heating consists of launching electromagnetic (EM) waves with antennas placed inside the vacuum vessel, the EM waves become eventually damped by ions and electrons effectively rising the plasma temperature. A more comprehensive explanation on plasma heating will be given in the following chapters.

These mechanisms have shown to be capable of rising the plasma thermal temperature to tens of keV. Furthermore, RF heating is able to develop a high energy population of ions in the range of MeV under appropriate conditions.

1.6.1 Ion Cyclotron Resonance Frequency Heating (ICRH)

There are numerous ways to heat a plasma using RF waves. Depending on the frequency of the wave one can heat electrons (ECRH) or ions (ICRH), or produce non inductive currents in the plasma (LHCD). The topic of this thesis is the modelling and analysis of ICRH in a variety of scenarios, for more details on other uses of RF waves see Refs. [1, 2]. The fundamental mechanism by which ions absorb or damp the wave's energy is due to a resonance condition in the equation of motion for ions under the effect of the wave's electric field. This condition is met when the Doppler shifted wave frequency matches the ion cyclotron frequency or its harmonic,

$$\omega = k_{\|} v_{\|} + l\omega_c \quad l = 0,\ 1,\ 2,\ ... \tag{1.9}$$

Here $k_{\|}$ is the parallel wave number, (parallel to the background magnetic field), ω_c is the cyclotron frequency, l stands for the harmonics of the wave, where $l = 1$ is the fundamental while $l > 1$ is for the higher harmonics. Notice that the cyclotron frequency 1.3b is proportional to the magnetic field which is inversely proportional to the major radius, thus allowing to place the resonance (heating) at a specific location (figure 1.8). The electric field of an electromagnetic wave can be divided in two components. A component parallel to the background magnetic field and another which is perpendicular. The parallel is small for waves in the ion cyclotron range of frequencies (fast wave mode) and can be neglected while the perpendicular can be divided in two components, a left circularly polarized component (E_+) and a right circularly polarized component (E_-). E_+ rotates in the same direction as ions while

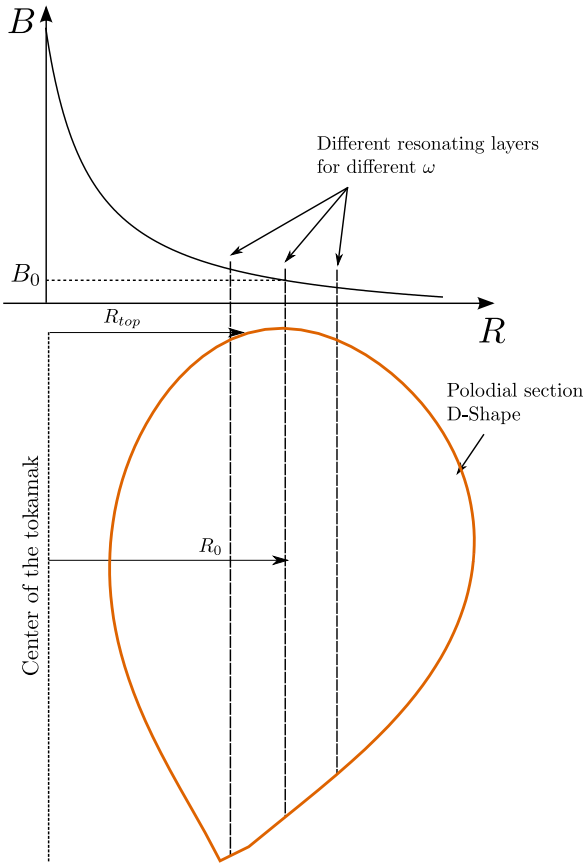

Fig. 1.8 *Magnetic field (B) profile with different resonating layers. B_0 is the value of the magnetic field at the center of the poloidal section.*

E_- is counter-rotating. These components typically increase the energy of the ions and modify the tail (high energy part) of the distribution function, more detail on it will be given in sections 2.3.2 and 2.4.1.

For the fundamental harmonic heating, neglecting the perpendicular wave number ($k_\perp \approx 0$) and assuming $v_\perp = v_x + iv_y$, and then, solving the differential equation for the evolution of the velocity yields,

$$v_\perp = v_0 e^{-i\omega_c t} + \frac{eE_+}{m} t e^{-i\omega_c t}, \tag{1.10}$$

where v_0 is the initial velocity and m is the ion mass. The first and second terms are always in phase thus experimenting a net acceleration.

The absorption on higher harmonics is more complicated. However, if the wave changes its amplitude in space, the particles will not be driven by a spatially uniform sine wave in time anymore. This fact can lead to resonance condition again. It occurs

when the wavelength and the Larmor radius (r_L radius of the ions orbit around the magnetic field) are comparable. Therefore, the perpendicular wave number is no more negligible $k_\perp \neq 0$. This is called finite Larmor radius effect (FLR) and is the responsible for absorption at higher harmonics.

1.7 High-performance scenario at JET and preparation for the next D-T campaign

The focus of the first D-T campaign (DTE1) performed at JET in 1997 [11–13] was to maximise the neutron yield, even if it was only during transient conditions. The second JET D-T campaign (DTE2) planned for 2020 has the goal not only to maximise the fusion yield but also to show that such fusion yield can be maintained in steady state. For this reason, during the 2015-2016 JET campaigns with the ITER-like-wall (ILW) many efforts have been devoted to the exploration of high-performance plasma scenarios envisaged for ITER operation [14]. In this context, high-performance scenario stands for a plasma configuration capable of delivering a large number of fusion reactions. The inductive (baseline) scenario [15] and the hybrid scenario [16] have achieved major improvements during these campaigns surpassing the previous ILW fusion record of $2.3 \cdot 10^{16}$ neutrons/s, thus showing good progress towards demonstrating the fusion rate goal for D-T. The objective for DT-ready plasma is $6 \cdot 10^{16}\ s^{-1}$ for 5s [17]. Figure 1.9 shows record DTE1 discharges and the equivalent D-T hybrid plasma 92398 together with the DTE2 ILW goal [18]. The goal for DTE2 is to achieve 15 MW of fusion power in steady state conditions which is around three times the power reached in 1997 with 1.7 times the heating power used. Notice that a fusion power of 16 MW was obtained in 1997 but it was not in steady state conditions but transiently.

The hybrid scenario reached with 33 MW of combined ICRF and NBI power a record neutron rate R_{NT} of $2.9 \cdot 10^{16}$ s^{-1}. The hybrid scenario is an advanced regime expected to be applied in ITER. It is characterized by a low plasma current I_p which allows operation at a high normalised beta $\beta_N = \langle\beta\rangle\, aB_T/I_p$ and a q profile ($q(0) \geq 1$) that prevents sawtoothing m=1, n=1 (1/1) magnetohydrodynamic (MHD) activity in the core from triggering large neoclassical tearing modes (NTMs) [16]. In preparation for the next D-T campaign at JET with the ILW, the analysis of this scenario's heating performance is of great relevance as it gives insight on the strategy to follow in order to obtain the D-T ready plasma objective. This thesis delves in the heating performance of the recent hybrid discharges and serves as a guideline on how to improve such performance.

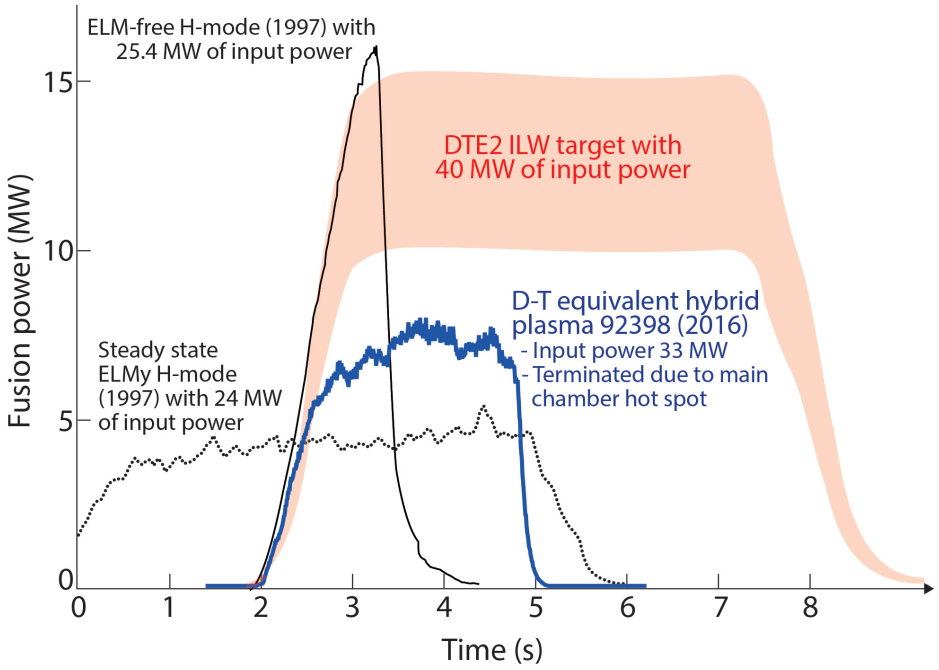

Fig. 1.9 *Fusion power of several JET discharges and DTE2 ILW target.*

One of the key aspects to analyse in order to reach steady state high-performance conditions is to avoid central impurity accumulation. The previous JET carbon wall was identified to have a high erosion rate and to retain fuel which is not tolerable for an eventual commercial reactor. For this reason, the JET plasma facing components were upgraded to the ILW which consists of beryllium (Be) in the main chamber and tungsten (W) in the divertor. In particular, W has a low erosion rate and a high temperature tolerance which make it ideal for the divertor. However, the maximum tolerable quantity of high-Z impurities such as W in a plasma is quite small (a concentration below 10^{-4} to achieve high-performance), if not, losses due to radiation become too large. Several studies have been performed at JET regarding the control of central impurity accumulation using ICRF waves [19–23]. Typically, it was found that central ICRH was capable of avoiding central impurity accumulation by outward convection and temperature impurity screening provided by fast ions. In chapter 4 we tackle the differences in the capability of ICRH to avoid impurity accumulation when the resonance is placed at different locations. Furthermore, we analyse the impurity screening due to fast ions and show that it is negligible as compared to the main ion contribution when finite orbit width (FOW) effects are taken into account. Other previous studies that neglected FOW found much larger contributions from fast ions [19, 22].

Detailed analysis of D-D and D-T plasmas for several ICRH schemes in the JET carbon wall has been performed in Refs [12, 13, 24, 25]. The present thesis provides analysis of the heating performance for the recent D-D hybrid discharges for the JET ILW (2015-2016). The heating physics leading to an improved performance are analysed in detail and discussed in chapter 5. The analysis of the impact on the plasma performance of several parameters is discussed, such as the energy transfer through the thermalisation process of the fast ions with the background ions and electrons [13, 24, 26], the plasma composition or the ICRH fusion enhancement [27, 28].

Given the relevance and interest shown in the forthcoming 2020 JET D-T campaign in preparation for ITER operation, a number of predictions based on high-performance D plasmas have been conducted [14, 29]. In chapter 6 predictions based on high-performing D hybrid discharges show the heating extrapolation performance in D-T plasmas. Furthermore, JET will undergo a T campaign before the first D-T experiments in order to assess the isotope effect and be able to interpolate between D and T experiments as to improve the D-T predictions accuracy. For this reason, chapter 7 studies the ICRH schemes for a T and a D-T scenario and highlights the similarities and differences from the heating point of view. In most of the cases, predictions are found not to be straightforward.

Chapter 2

Physics of Ion Cyclotron Resonance Frequency Heating

How does a wave propagate in a plasma? How is this wave damped by the plasma? These kind of questions are answered in this chapter. The first step to understand how a wave will propagate is by means of solving the Maxwell equations with a proper plasma model that relates the plasma current and the electric field. After that, the dielectric tensor of the plasma is found. The basic physics and formalism used in ICRH physics, as well as the derivation of the most important formulas are shown in this chapter. An explanation of the most relevant concepts will be made such as cutoffs, wave resonances, polarization, mode conversion, accessibility and the plasma model used to describe the wave propagation. As a continuation of these general concepts, several ICRF schemes are introduced as a natural consequence of polarisation effects and their wave damping strength is discussed. The chapter ends with a description of the computational model of this class of problems, a self-consistent model involving the computation of the propagation of an electromagnetic wave (EM) and the distribution function of the resonant particles.

2.1 Wave propagation in a plasma

The propagation of EM waves in any media and for all range of frequencies is governed by Maxwell equations. Our interest is to understand how the EM wave launched by the antenna propagates in a plasma medium. In order to solve the wave propagation it is necessary to calculate the wave equation and the permittivity (ε) of the material, i.e., the material response to an electric excitation. Typically, the response of the material is described by the magnetisation $\vec{M}$ and the polarisation $\vec{P}$. However, in plasma

physics, the information regarding the plasma response is preferred to be explicitly kept in the plasma current $\vec{J}$ rather than in $\vec{P}$ or $\vec{M}$. The Maxwell equations in a material medium are,

$$\nabla \cdot \vec{D} = \rho_{free}, \tag{2.1a}$$

$$\nabla \times \vec{E} = -\frac{\partial \vec{B}}{\partial t}, \tag{2.1b}$$

$$\nabla \times \vec{H} = \vec{J}_{free} + \frac{\partial \vec{D}}{\partial t}, \tag{2.1c}$$

$$\nabla \cdot \vec{B} = 0, \tag{2.1d}$$

where $\vec{E}$ is the electric field, $\vec{B}$ is the magnetic induction (magnetic field), $\vec{H} = \frac{\vec{B}}{\mu_0} - \vec{M}$ is the magnetic intensity, ρ_{free} is the free charge density and $\vec{D} = \varepsilon_0 \vec{E} + \vec{P}$ is the displacement electric field. Taking into account that the magnetization current is defined as $\nabla \times \vec{M} = \vec{J}_{mag}$ and the polarization current as $\frac{\partial \vec{P}}{\partial t} = \vec{J}_{pol}$ we can rewrite equation 2.1c so that the plasma response is kept explicitly in $\vec{J}$,

$$\nabla \times \vec{B} = \mu_0 \left(\vec{J}_{free} + \vec{J}_{mag} + \vec{J}_{pol} \right) + \varepsilon_0 \mu_0 \frac{\partial \vec{E}}{\partial t}. \tag{2.2}$$

The total plasma current is $\vec{J} = \vec{J}_{free} + \vec{J}_{pol} + \vec{J}_{mag}$ and $\varepsilon_0 \mu_0 = 1/c^2$. The solution for the electric field of the wave equation is found by applying the curl to Faraday's law (equation 2.1b),

$$\nabla \times \nabla \times \vec{E} = -\mu_0 \frac{\partial \vec{J}}{\partial t} - \frac{1}{c^2} \frac{\partial^2 \vec{E}}{\partial t^2} \tag{2.3}$$

To proceed it is necessary to find a relation between the plasma current and the electric field. For a conductor it is typically described as $\vec{J} = \bar{\sigma} \vec{E}$, where $\bar{\sigma}$ is the conductivity and it needs to be computed by solving the momentum equations of the plasma. We assume harmonic like solutions in space and time, i.e., $Q(t) \sim e^{i(kx - \omega t)}$, therefore, we can rewrite equation 2.3 as an algebraic equation using $\nabla \to i\vec{k}$ and $\frac{\partial}{\partial t} \to -i\omega$,

$$\vec{k} \times \vec{k} \times \vec{E} + i\omega \bar{\sigma} \vec{E} + \frac{\omega^2}{c^2} \vec{E} = 0 \tag{2.4}$$

Rearranging terms and taking into account that the index of refraction is defined as $\vec{n} = \frac{c}{\omega} \vec{k}$, equation 2.4 can be rewritten as

$$\vec{n} \times \vec{n} \times \vec{E} + \bar{K} \vec{E} = 0, \tag{2.5}$$

where we have used the permittivity, defined as,

$$\bar{K} = \frac{\bar{\varepsilon}}{\varepsilon_0} = \bar{I} + i\frac{\bar{\sigma}}{\omega\varepsilon_0}, \tag{2.6}$$

which can also be calculated by using the constitutive relation $\vec{D} = \varepsilon\vec{E}$ and the Ampère's law. We can express equation 2.5 in matrix form by making use of the identity ($\nabla \times \nabla \times \vec{A} = \nabla(\nabla \cdot \vec{A}) - \nabla^2\vec{A}$),

$$\begin{pmatrix} K_\perp - n^2\cos^2\theta & -iK_{xy} & n^2\cos\theta\sin\theta \\ iK_{xy} & K_\perp - n^2 & 0 \\ n^2\cos\theta\sin\theta & 0 & K_\parallel - n^2\sin^2\theta \end{pmatrix} \begin{pmatrix} E_x \\ E_y \\ E_z \end{pmatrix} = \begin{pmatrix} 0 \\ 0 \\ 0 \end{pmatrix}. \tag{2.7}$$

As this is an homogeneous set of equations $\mathbf{A}\vec{x} = 0$, solving $det(\mathbf{A}) = 0$ is equivalent to solve the dispersion relation $D(\omega, \vec{k}) = 0$, i.e., the relation between $\vec{k}$ and ω. In general, many roots will exist, bringing many solutions, called modes. Each mode is a different type of wave with a different perpendicular refractive index. However, we need a plasma model to compute the conductivity tensor before we can solve the dispersion relation.

2.2 The Cold Plasma Model

In order to compute the conductivity we need to find the velocity of electrons and ions as $\vec{J} = en_0(\vec{v_i} - \vec{v_e}) = \bar{\sigma}\vec{E}$. We express the equations of motion for ions and electrons assuming that the plasma is in an equilibrium and, therefore, only perturbations of small amplitude are taken into account,

$$m_e\left(\frac{\partial\vec{v_e}}{\partial t} + \vec{v_e}\cdot\nabla\vec{v_e}\right) = -e(\vec{E} + \vec{v_e}\times\vec{B}) - \nabla\cdot\bar{\Phi}_e \tag{2.8a}$$

$$m_i\left(\frac{\partial\vec{v_i}}{\partial t} + \vec{v_i}\cdot\nabla\vec{v_i}\right) = -e(\vec{E} + \vec{v_i}\times\vec{B}) - \nabla\cdot\bar{\Phi}_i. \tag{2.8b}$$

The cold plasma model assumes that the fluid stress tensor is $\bar{\Phi}_e = \bar{\Phi}_i = 0$. This approximation is valid when the phase velocity of the wave is much greater than the thermal velocity of ions and electrons which is not true in regions of intense heating such as in the resonance layer or in the wave resonance region where the phase velocity tends to zero. However, the cold plasma model is useful to describe the propagation of the wave in a wide range of scenarios and it typically gives accurate information even in

hot plasmas. As we assume small perturbations, second order terms can be neglected. Thus, we can linearise the equations and make them algebraic by implementing the Fourier analysis. Taking into account that the propagation inside the plasma the x axis, $k_x = k_\perp$. The components of the perturbed momentum equation become (both for electrons and ions),

$$-i\omega m v_x = q(E_x + v_y B_0), \tag{2.9a}$$

$$-i\omega m v_y = q(E_y - v_x B_0), \tag{2.9b}$$

$$-i\omega m v_z = q E_z. \tag{2.9c}$$

It is straightforward to obtain the velocities for these three algebraic equations,

$$v_x = \frac{q}{m}\frac{i\omega E_x - \omega_c E_y}{\omega^2 - \omega_c^2}, \tag{2.10a}$$

$$v_y = \frac{q}{m}\frac{i\omega E_y + \omega_c E_x}{\omega^2 - \omega_c^2}, \tag{2.10b}$$

$$v_z = \frac{iq}{m\omega} E_z, \tag{2.10c}$$

where $\omega_c = \frac{qB_0}{m}$ is the cyclotron frequency. Taking into account that $\vec{J} = \bar{\sigma}\vec{E}$ and $\vec{J} = en_0(\vec{v_i} - \vec{v_e})$ the conductivity tensor is,

$$\bar{\sigma} = \begin{pmatrix} \sigma_{xx} & \sigma_{xy} & 0 \\ \sigma_{yx} & \sigma_{yy} & 0 \\ 0 & 0 & \sigma_{zz} \end{pmatrix}. \tag{2.11}$$

We can now build the dielectric tensor $\bar{K}$ recalling equation 2.6,

$$\bar{K} = \begin{pmatrix} K_\perp & -iK_{xy} & 0 \\ iK_{xy} & K_\perp & 0 \\ 0 & 0 & K_\parallel \end{pmatrix}. \tag{2.12}$$

Here,

$$K_\perp = K_{xx} = K_{yy} = 1 - \sum_j \frac{\omega_{pj}^2}{\omega^2 - \omega_{cj}^2}. \tag{2.13a}$$

$$K_{xy} = -K_{yx} = \sum_j \frac{\omega_{cj}\omega_{pj}^2}{\omega(\omega^2 - \omega_{cj}^2)}. \tag{2.13b}$$

$$K_\parallel = K_{zz} = 1 - \sum_j \frac{\omega_{pj}^2}{\omega^2} \tag{2.13c}$$

and the sums are over all particle species including electrons and ion species and $\omega_{pj} = \frac{n_j(Z_j e)^2}{\varepsilon_0 m_j}$ is the plasma frequency. As the conductivity has been calculated, we can now obtain the different roots for $n_\perp$ from the dispersion relation (equation 2.7). In the ion cyclotron range of frequencies the two different roots or modes are the shear Alfvén or slow wave (2.14a) and the fast magnetosonic or compressional Alfvén wave (2.14b) [30],

$$n_{\perp_{SW}}^2 = \frac{(\varepsilon_\perp - n_\parallel^2)\varepsilon_\parallel}{\varepsilon_\perp} \qquad \textit{Slow wave} \tag{2.14a}$$

$$n_{\perp_{FW}}^2 = \frac{(\varepsilon_\perp - n_\parallel^2)^2 - \varepsilon_{xy}^2}{\varepsilon_\perp - n_\parallel^2} \qquad \textit{Fast wave} \tag{2.14b}$$

2.3 Basic concepts on wave propagation

Now that we have calculated in section 2.2 the two modes that propagate in the ion cyclotron range of frequencies, we need to assess whether they are able to reach the wave-particle resonance before encountering especial regions in the plasma where the energy or the properties of the wave might change in an undesirable way. Moreover, the study of the wave polarisation is crucial if optimisation of ion absorption is sought.

2.3.1 Cutoffs and wave resonances

In the plasma there are regions where the refractive index ($\vec{n}$) or equivalently the wave number ($\vec{k}$) can take extreme values. These regions are of especial interest as they give information regarding the wave propagation. We identify $k_z = k_\parallel = \vec{k} \cdot \frac{\vec{B}_0}{||B_0||}$ in the toroidal direction and $k_x = k_\perp$ in the radial direction.

As the modes (equations 2.14a and b) propagate in the radial direction, $k_\perp^2$ needs to stay positive in order to reach the plasma center, otherwise the wave might become evanescent as the amplitude will decrease like $\sim e^{-k_\perp x}$. The value of $k_\perp^2$ might become negative when $k_\perp^2 \to 0$ in the so-called cutoff region. In this region, the wave gets partially reflected and partially transmitted. The wave that goes through this region, called an evanescent region, will exponentially decay as explained. It is important to mention that the phase velocity goes to infinity although the group velocity remains finite and under the speed of light.

Another case of interest, the resonance region, is where $k_\perp \to \infty$. Here the phase and group velocity tend to zero, and the transport of energy slowly decreases. In the cold plasma model, the energy is absorbed. However, if kinetic effects are taken into account as in the hot plasma model, the wave properties change through mode conversion which is discussed later in section 2.3.5.

Notice that wave resonance is not equivalent to wave-particle resonance, which is the basic mechanism in which the plasma absorbs energy from the waves. Wave-particle resonance occurs when the velocities of particles are set properly permitting a large absorption of the wave energy by the resonant ions and/or electrons. The condition of wave-particle resonance is given by equation 1.9.

2.3.2 Polarization

Once the dispersion relation (equation 2.7) and its solutions (modes) have been found, the polarization of the wave, i.e., the relation between the electric field components (E_x, E_y, E_z) for each mode, can be established. In optics, the polarization of a wave is defined as the ratio between the perpendicular components of the electric field to $\vec{k}$, as they are always perpendicular to the propagation. In plasma physics the wave can have an electric field component parallel to $\vec{k}$ which means that longitudinal waves exist in plasma. Therefore, there exist numerous ways to classify this *zoo* of waves. However, we will derive the polarization for ion heating for typical propagations perpendicular to the background magnetic field that correspond to the solutions found in equations 2.14a and b.

We define the wave based on the fact whether the wave has an electric field component in the magnetic background direction or not.

$$\text{O Mode} \implies E_\parallel \neq 0, \tag{2.15a}$$

$$\text{X Mode} \implies E_\parallel = 0. \tag{2.15b}$$

We might have "O" mode, ordinary wave (equation 2.14a), or "X" mode, extraordinary wave (equation 2.14b), whether we have an electric field component in the background magnetic field or not, respectively. It is convenient in this kind of analysis to define a new set of electric field components, which rotate clockwise and anticlockwise, similarly as those defined in [30]. For that, we combine equation 2.9a with equation 2.9b multiplied by the imaginary number,

$$-i\omega m(v_x + iv_y) = q(E_x + iE_y + v_y B_0 - iv_x B_0) \tag{2.16a}$$

$$-i\omega m(v_x - iv_y) = q(E_x - iE_y + v_y B_0 + iv_x B_0). \tag{2.16b}$$

These equations can be rewritten in the more familiar form,

$$-iv_+(\omega - \omega_c) = \frac{q}{m}E_+, \tag{2.17a}$$

$$-iv_-(\omega + \omega_c) = \frac{q}{m}E_-, \tag{2.17b}$$

where,

$$E_\pm \equiv \frac{1}{\sqrt{2}}(E_x \pm iE_y), \tag{2.18a}$$

$$v_\pm \equiv \frac{1}{\sqrt{2}}(v_x \pm iv_y). \tag{2.18b}$$

This is the typical way to define the electric field as particles rotate clockwise or anticlockwise around the magnetic field depending on their charge. Therefore, anticlockwise polarisation or left circularly polarized wave (E_+) maximises ion absorption while clockwise polarization or right circularly polarized wave (E_-) enhances electron absorption.

In order to assess whether ion absorption is possible we need to study the wave polarization in the resonant region. Typically, the fast wave that reaches the resonant region is elliptically polarized. Therefore, the fraction of power absorbed depends upon the ratio of E_+/E_-. For a single ion species and using equation 2.7 assuming $E_z \sim 0$,

$$\frac{E_+}{E_-} \simeq \frac{\varepsilon_{xy} + \varepsilon_\perp - n_\parallel^2}{\varepsilon_{xy} - \varepsilon_\perp + n_\parallel^2}. \tag{2.19}$$

Assuming $n_\parallel \sim 0$, equation 2.19 reduces to

$$\frac{E_+}{E_-} = \frac{\omega - \omega_{ci}}{\omega + \omega_{ci}}. \tag{2.20}$$

For $\omega = \omega_{ci}$ the left circularly polarized wave (E_+) completely vanishes for a single species plasma. This means that absorption is very small since the wave is completely right polarized. There are three main ways to avoid this undesirable situation: using higher harmonics of the ion cyclotron frequency, minority heating or the recently investigated three ions-scheme. The first way solves this situation trivially, substituting in equation 2.19, $E_+ \neq 0$. As $\omega = l\omega_{ci}$ where $l = 1, 2, ...$ it implies that,

$$\frac{E_+}{E_-} = \frac{l-1}{l+1}$$

On the other hand, the second way, minority heating, is based in adding a small amount, normally a few percent, of an ion species with higher ion cyclotron frequency. The point is to choose the ICRH frequency to correspond $l = 1$, the fundamental of the minority species. The dispersion relation is mostly determined by the majority species and therefore E_+ should not vanish.

However, a deeper analysis shows that E_+ turns to be small at both ion cyclotron frequencies, for majority and minority. The polarisation changes very rapidly near the minority cyclotron frequency, producing a substantial damping strength. In fact, Doppler broadening of the resonance is enough to widen the resonance and obtain a good damping.

Finally, in plasmas with three ion species, there is third way to provide $E_+ \neq 0$. The key idea is to locate the left-hand polarized fast wave cutoff $n_\parallel^2 = \varepsilon_\perp - \varepsilon_{xy}$ (see equation 2.19), which largely enhances the associated RF field component E_+, close to the fundamental cyclotron resonance of a minority ion species. This can be achieved by adjusting the density ratio between the two main ion species. Such three-ion scenarios can substantially facilitate the use of ICRF for the generation of high-energy ions in fusion plasmas and also suggested for bulk ion heating with intrinsic impurity species in mixture plasmas [31, 32].

2.3.3 Accessibility

So far we have defined the capability of a wave to actually heat ions through polarization and we have studied two regions of especial interest for wave propagation, the cutoff and the wave resonance regions. The final goal is to assess whether the wave is able to reach the particle-wave resonance region. Accessibility is a concept that refers to the possibility of a plasma wave to reach the desired location in which it can be absorbed. This is the analysis that takes into account all of the phenomena involving the plasma

propagation and confirms whether a certain type of wave can reach the center or not. It is not trivial to avoid all the cutoff regions and reach the resonant region.

So, when a certain wave is said to have a good accessibility it means that it is able to propagate until it reaches the desired region. Accessibility also takes into account where the waves are launched, i.e the wave can avoid certain cutoff layers if the antenna is well positioned. In a tokamak there exist two regions of special interest, the low-field side (LFS) located at the outer boundary of the torus, and the high-field side (HFS) located at the inner boundary. In ICRH, waves are usually launched from LFS to avoid technical difficulties associated with locating antennas at the HFS.

2.3.4 Accessibility of slow and fast waves

We will limit our accessibility study to the ICRH modes found. The idea is to look for the zeros in the numerator and the denominator for the cuttof and wave resonance regions, respectively, of equations 2.14a and b. Simplified forms for the elements of the dielectric tensor can be introduced. Making use of the small electron mass expansion, for most present day experiments the following expansion is applicable,

$$\frac{\omega_{pe}^2}{\omega_{ce}^2} \approx O(1), \tag{2.21a}$$

$$\frac{\omega_{pi}^2}{\omega_{ci}^2} \approx O\left(\frac{m_i}{m_e}\right), \tag{2.21b}$$

$$\frac{\omega^2}{\omega_{ci}^2} \approx O(1), \tag{2.21c}$$

$$\frac{\omega_{pe}^2}{\omega^2} \approx O\left(\frac{m_i}{m_e}\right)^2. \tag{2.21d}$$

In order to make the analysis simpler, we will assume that in eqs. (2.13a) and (2.13b) the parallel refractive index is zero, so $n_\parallel = 0$. Using the previous expansions we can see immediately that the slow wave dispersion relation reduces to,

$$n_\perp^2 = \frac{-\omega_{pe}^2}{\omega^2} \tag{2.22}$$

Since it is negative, there is no accessibility to the center of the plasma, so we must rely on the fast wave. More sophisticated analysis can be done by assuming a value for $n_\parallel \neq 0$, but one finds out that it cannot be applied in all cases. A bit more explanation can be done for the fast wave where if we assume again $n_\parallel$ to be negligible and for

simplicity a plasma of only one ion species. We end up with

$$n_\perp^2 = \frac{\omega_{pi}^2}{\omega_{ci}^2}. \tag{2.23}$$

As we have a positive refractive index we assume that we have good accessibility to the center of the tokamak. However, this simple analysis does not offer any idea about the cuttoff or wave resonance regions. A more detailed analysis should be done taking into account multiple ion species and $n_\parallel \neq 0$. For the fast wave (equation 2.14b) the wave resonance occurs at $\varepsilon_\perp = n_\parallel^2$. This leads to the Alfvén resonance frequency $\omega^2 = \omega_{ci}^2 k_\parallel^2 c^2/(k_\parallel^2 c^2 + \omega_{pi}^2)$ for a single ion species. This is always smaller than the ion cyclotron frequency, and if it occurs it is in the inner plasma, on the high-field side. For two ion species there are additional resonances of the fast wave, if we again assume $n_\parallel$ to be negligible, the resonances turn to be identical to the ion-ion hybrid resonances given by $\varepsilon_\perp = 0$. This frequency for a case of two species plasma is [33],

$$\omega_{ii}^2 = \omega_{c1}^2 \frac{1 + f_1 Z_1 \left(\frac{Z_2 m_1}{Z_1 m_2} - 1\right)}{1 + f_1 Z_1 \left(\frac{Z_1 m_2}{Z_2 m_1} - 1\right)} \tag{2.24}$$

Here we have used the charge neutrality condition $Z_1 f_1 + Z_2 f_2 = 1$ where $f_j = \frac{n_j}{n_e}$. Mode conversion occurs at the ion-ion hybrid resonance which is not explained by the cold plasma model. The mode converted ion Bernstein wave is rapidly absorbed via electron Landau damping.

On the other hand, the cutoff layers are given by $n_\parallel^2 = \varepsilon_\perp + \varepsilon_{xy} = R$ and $n_\parallel^2 = \varepsilon_\perp - \varepsilon_{xy} = L$. Here, R and L refer to right and left in the Stix notation [30]. The cutoff $n_\parallel^2 = R$ is one of the main issues in ICRH since it gives a cutoff layer on the low-field side. This fact forces the antennas to be placed as close as possible to the plasma, in order to avoid the evanescent region associated with the cutoff layer. If we force equation 2.14b to be $n_\perp > 0$ we find a threshold for the plasma density (one species),

$$\omega_{pi}^2 > (\omega + \omega_{ci})\omega_{ci} n_\parallel^2 \tag{2.25}$$

The $n_\parallel^2 = L$ gives the cutoff associated with the ion-ion hybrid resonance. For a two species plasma this cutoff is approximately,

$$\omega_{cut} = \omega_{c1}\left[1 + f_1 Z_1 \left(\frac{Z_2 m_1}{Z_1 m_2} - 1\right)\right] \tag{2.26}$$

If we compare equations 2.24 and 2.26 we realise that $\omega_{ii} < \omega_{cut}$ for a given magnetic field. This implies that for a given frequency the ω_{ii} will be on the left of ω_{cut}. So we could place the antenna in the high-field side and work in the mode-conversion regime. This in practice is presently no longer done due to technical problems associated with the limited space and access on the inside of the torus. The heating of tokamak plasmas is carried out via ion cyclotron resonance instead of mode-conversion regime. All the modelling shown in this thesis is by means of ion cyclotron resonance using the fast wave launched from the LFS.

2.3.5 Mode conversion

Mode conversion (MC) involves two different plasma waves. They both have the same ω and $k_{\parallel}$ but different values for $k_{\perp}$. They are different roots of the same dispersion relation (different modes). When at a certain point inside the plasma the profile of $k_{\perp}$ evolves in such a way that both values coalesce, mode conversion occurs. In the cold plasma model this happens in the resonance region. The final result is that some energy of the initial wave is transferred to the second wave which will propagate further into the plasma according to its own dispersion characteristics. The study performed in this thesis does not involve MC for any of the experiments considered.

2.4 Damping Mechanisms

The relevant electric field component of the electromagnetic wave is the one perpendicular to the background magnetic field. In fact, for practical cases one can assume the parallel electric field component to be negligible. As the perpendicular electric field component rotates in the same direction as ions, absorption at the fundamental and at higher harmonics (FLR effects) can be important.

Direct electron damping is important although the electric field component for this process to occur is the one parallel to the background magnetic field. The parallel gradient of the wave magnetic field can accelerate electrons, this is known as transit-time magnetic pumping (TTMP). The fast wave can also undergo mode conversion.

2.4.1 Damping at the ion cyclotron resonance

Damping of the electromagnetic wave at the ion cyclotron resonance is produced when the wave frequency matches the ion cyclotron frequency or its harmonics. Considering the fundamental harmonic an ion will remain in phase with the wave which in turn will

be damped and transfer its energy to the ion. This is only true for small or negligible Larmor radius. If r_L is not small compared with the perpendicular wavelength $\lambda = \frac{2\pi}{k_\perp}$, the wave electric field will not be only time dependent but also space dependent. So the electric field will change all along the cyclotron trajectory.

Taking into account a finite Larmor radius with respect to the perpendicular wavelength at the fundamental ion cyclotron frequency means that either the kick in energy to the ions can be positive or negative. In other words, the ion can win or lose energy. As FLR effects are important in both, fundamental and higher harmonics, one must consider this effect. Moreover for $r_L > \lambda$, not only E_+ but also E_- can produce absorption.

The kick in energy for the perpendicular velocity to the background magnetic field that an ion experiences when passing through a resonance region scales as [34],

$$\Delta v_\perp \propto \left[E_+ J_{n-1}\left(\frac{k_\perp v_\perp}{\omega_{ci}}\right) + E_- J_{n+1}\left(\frac{k_\perp v_\perp}{\omega_{ci}}\right)\right], \tag{2.27}$$

where n is the cyclotron harmonic number and J_n is a Bessel function of the first kind. The relative phase between the ions and the wave is normally modified by collisions and non-linearly as result of the wave-particle interaction between successive transits of the ion through the ICRH resonance region. In this way, ions undergo random kicks and can either gain or lose net energy from the wave. If more ions gain energy than lose energy then there is transfer of energy from wave to particles. In any case, when the distribution of the ions is similar to a Maxwellian distribution (much more ions with low perpendicular velocities), or in general if $df/dv < 0$ the net energy transfer is from the wave tends the ions.

From equation 2.27 many physical effects can be inferred from the bessel functions. For the fundamental ion cyclotron resonance the kick in the perpendicular velocity is rather uniform in the velocity space. Low energy ions are also well accelerated by the wave. For higher harmonics $n \geq 2$, low energy ions are not efficiently accelerated while absorption increases as the perpendicular velocity does. Normally a maximum is reached in the MeV range, after that absorption decreases. Thermal plasmas are not properly heated by ICRH for harmonics $n \geq 2$. Moreover, the damping strength decreases with the harmonic number.

In principle, in order to heat the plasma at higher harmonics it is not necessary to use any other external method to heat it previously. If initially the density is high enough and the energy of the plasma is not too low, a tail of energetic ions will start

to form in the distribution function. If these ions are confined, more ions will interact with the electromagnetic wave, improving the absorption.

2.4.2 Direct electron damping

Electrons are also heated by the fast wave. The parallel field component of the wave accelerates the electrons along the magnetic field. This is called electron Landau damping and as the fast wave has low parallel electric field the absorption is weak. Electrons have a magnetic moment associated to their cyclotron motion and are also accelerated by the parallel gradient of the wave magnetic field. This is the transit-time magnetic pumping (TTMP). Both processes counteract each other, reducing the total absorption.

2.5 The distribution function

For a complete definition of a plasma composed by N particles one must solve the 3N equation of motion $\vec{F_i} = m_i\vec{a_i}$ where the force acting on the i-th particle is composed by the influence of all the other particles. Furthermore, one needs to know the initial position and velocity of each particle leading to a total of $6N$ parameters. This is not only prohibitive from the analytic point of view but also from the computational one. The treatment of the system on a macroscopic scale turns to be simpler. Pressure, temperature, density and flow are magnitudes that can describe the system also locally. In kinetic theory, the most important quantity is the distribution function $f(\mathbf{r}, \mathbf{v}, t)$. It expresses the density of particles in a six-dimensional phase space, $\int d\mathbf{r}d\mathbf{v}f = N$. However, the distribution function can be normalized as $\int d\mathbf{r}d\mathbf{v}f = 1$, in this case $fd\mathbf{r}d\mathbf{v}$ represents the probability of finding a particle in the volume $d\mathbf{r}d\mathbf{v}$.

As the number of particles must be conserved, f must satisfy the continuity equation

$$\frac{\partial f}{\partial t} + \nabla_{\mathbf{r},\mathbf{v}}((\vec{v}, \vec{a})f) = 0.$$

If the Hamiltonian equations of motion are satisfied, the kinetic equation becomes the Boltzmann equation,

$$\frac{\partial f}{\partial t} + \vec{v} \cdot \nabla_r f + \frac{\vec{F}}{m} \cdot \nabla_v f = \left.\frac{\partial f}{\partial t}\right|_{coll}. \tag{2.28}$$

Here $\vec{F}$ refers to the external forces, while the term on the right refers to the internal forces (collisions between particles).

In the ICRH field, the evolution of the velocity distribution function of the resonating ions is described by the Fokker-Planck equation. Formally the equation is as follows [35],

$$\frac{\partial f}{\partial t} = -\frac{\partial}{\partial X} \cdot (\langle \Delta X \rangle f) + \frac{1}{2} \frac{\partial^2}{\partial X^2} : (\langle \Delta X \Delta X \rangle f). \tag{2.29}$$

Here X represents a point in the phase-space and the double dot (:) is the double dot product. The quantities in brackets are the mean values during a time Δt, these average changes are called, ΔX (friction coefficient) and $\Delta X \Delta X$ (diffusion coefficient),

$$\langle \Delta X \rangle \equiv \frac{1}{\Delta t} \int d(\Delta \mathbf{X}) \Delta X \psi(X, \Delta X).$$

The function $\psi(X, \Delta X)$ gives the probability that X changes by an amount ΔX. The distribution function is a key concept in the ICRF heating study as it has a strong influence on wave damping and neutron rate generation. Its effects are analysed in detail in chapter 5 where different concentrations of minority ions produced different distributions for the majority ions with an important impact on the neutron production and ICRF absorption. In chapter 7, different plasma compositions lead to large differences between scenarios, largely due to different distributions of resonant ions.

2.5.1 Collisional heating

We have seen how ions absorb the wave energy and we have stressed the importance of maximising ion absorption. However, resonant ions will slow-down via collisions either on ions or electrons and, therefore, potentially delivering energy to electrons. A key quantity for the collisional frequency on ions or electrons is given by a threshold energy, the so-called critical energy [36],

$$E_{crit} = 14.8 A T_e \left[\sum_j \frac{n_j Z_j^2}{n_e A_j} \right]^{\frac{2}{3}}. \tag{2.30}$$

Here A is the atomic number and T_e is the electron temperature, the sum is over thermal ion species. At this energy ions transfer energy equally to both, ions and electrons. Above this energy ions collide with electrons and, as ions are much more massive, during the deceleration they will not change much their trajectory. Therefore, the pitch angle $cos\theta = v_{\parallel}/v$ will remain almost constant. Below this energy fast ions

will collide with thermal ions. In this regime pitch angle scattering is important and also energy diffusion. It is important to keep resonating ions below this energy in order to obtain bulk ion heating. In chapter 5 we discuss the impact of bulk ion heating in order to achieve the so-called high-performance discharges and improve the fusion rate. As a means of visual understanding of the wave damping and slow-down processes, figure 2.1 shows a scheme of such phenomena. The collision frequency decreases sharply

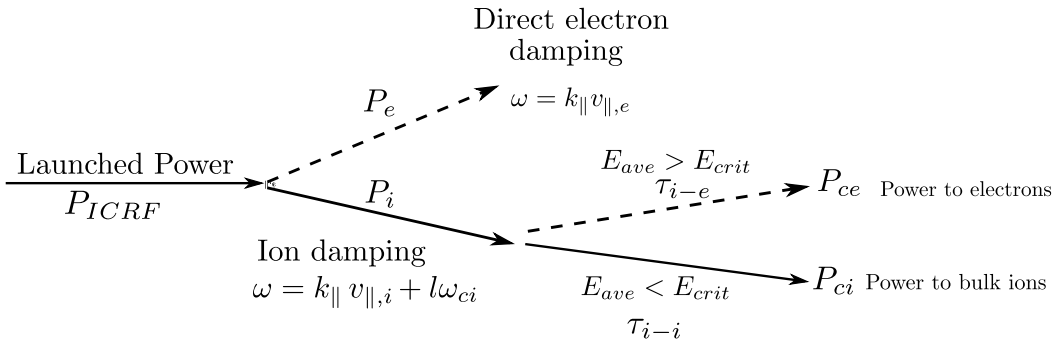

Fig. 2.1 *Scheme of the power deposition in the ICRF heating process.*

with velocity, scaling as v^{-3} at high velocities. This means that collisions are not fast enough to relax the fast ions and often the distribution function becomes strongly non-Maxwellian. The fast wave accelerates ions mainly in the perpendicular direction of the magnetic field. So ions increase their perpendicular velocity $v_\perp \gg v_\parallel$, producing an anisotropic tail in the perpendicular direction with a large number of trapped ions. These trapped ions experience an orbit shift from the magnetic flux surface on which they are confined, effectively changing of magnetic flux surface with turning points close to $\omega = l\omega_{ci}$ (figure 2.2). This effect tends to spatially broaden the collisional power to electrons and is taken into account in all of the simulations performed in this thesis. It becomes particularly important in chapter 4 where the broadening of the orbit tends to avoid sharp gradients of fast ions temperature, effectively reducing their capability to control impurities.

2.6 Modelling of ICRF heating

The modelling of ICRF heating is crucial to calculate the power absorption of each resonant species and to compute the evolution of the resonant ions velocity distribution function in ICRF heated plasmas. This information allows us to compute several important quantities, such as the neutron yield, plasma energy, ion-electron and ion-ion

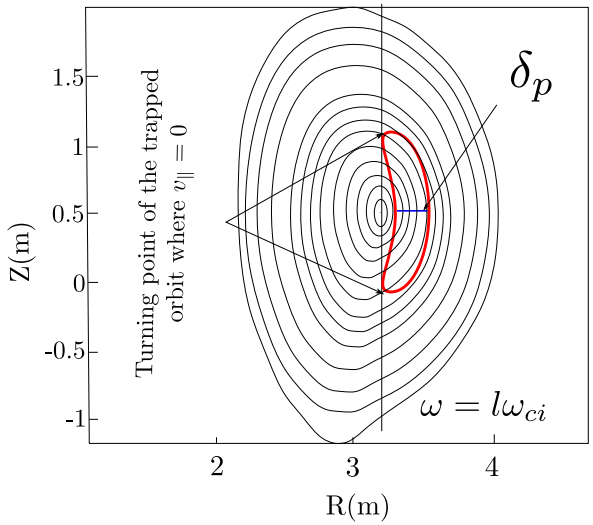

Fig. 2.2 *Approximated magnetic surfaces (black), orbit of the trapped particle (red) and δ_p (blue).*

collisionality energy transfer. ICRF modelling helps us understand plasma behaviour under external heating conditions such as ICRF heating.

The modelling of ICRF heating can be divided into two main parts. The first one is coupling, propagation and absorption of the wave in the plasma, while the second one is the evolution of the distribution function of the resonating species. Since the propagation and absorption of the wave depend on the distribution function of the resonating ions, which also depends on the absorbed power, the two problems are coupled and have to be solved self-consistently (figure 2.3).

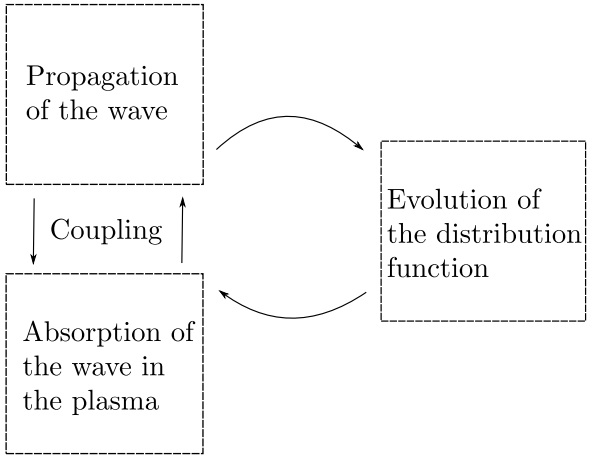

Fig. 2.3 *Scheme of the coupled problem. The propagation and absorption are computed using the dispersion relation while the evolution of the distribution function uses the Fokker-Planck model.*

2.6.1 Modelling of the deposition power

As stated in section 2.1 all the physics of the wave is contained in equation 2.5. In order to compute the propagation, coupling and absorption of the wave, the equation must be solved. The dielectric tensor $\bar{K}$ (2.6) must be known to effectively solve the equation.

Decomposing the dielectric tensor into its Hermitian and anti-Hermitian parts as $\bar{K} = \bar{K}^H + i\bar{K}^A$, the irreversible dissipation of the wave is governed by the anti-Hermitian part $\bar{K}^A$. While the Hermitian part of the dielectric tensor is almost not affected by deviations from the thermal equilibrium, they can have an important impact on the anti-Hermitian part. As the anti-Hermitian part is proportional to the particle distribution functions and their gradients in velocity space, it is affected by the presence of energetic ions [37]. The presence of energetic ions strongly modify the absorption of the fast wave as stated in section 2.4.1.

The parallel velocity of the particles, although not directly affected by the absorption or the propagation of the wave, is important for the Doppler effect involved in the resonant condition of equation 1.9. The parallel velocity distribution function determines the broadening of the deposition profile, affecting the absorption. While the perpendicular velocity of the particles affects the absorption strength.

The mode-converted waves require more study, not only for the power deposition but also for the frequency at which they are produced. The Budden model [38] which describes the physics of a cutoff-resonance pair gives a simple description of resonant absorption and tunneling. The Budden model states that the transmission coefficient, T, defined as the fractional power transmitted across the wave resonance for unit incident power, is given by $T = e^{-\pi k_0 \Delta x}$, where k_0 is the wave number far from the cutoff and Δx is the separation between the cutoff and the resonance. T does not depend whether the wave encounters the cutoff or the resonance first. However, for reflection there exist an asymetry, if the wave encounters resonance region first the reflection coefficient is described as $R = 0$. If the wave encounters the cutoff first, then $R = (1 - T)^2$. This is the case relevant for most present day fusion experiments.

2.6.2 Modelling of the evolution of the distribution function

The evolution of the velocity distribution function of the resonating ions can be described by an orbit-averaged Fokker-Planck equation

$$\frac{\partial f}{\partial t} = \langle Q(f) \rangle + \langle C(f) \rangle. \tag{2.31}$$

Here the brackets represent the average over a drift orbit, $Q(f)$ is a quasi-linear diffusion operator describing wave-particle interaction and C is a collision operator. In the orbit-averaged Fokker-Planck equation, the distribution function is a function of the constants of motion describing the single particle motion. For small orbit width, the equation is two dimensional in velocity space with the velocity and the magnetic moment as constants of motion. The two dimensional equation was used by Stix [39], who was the first to study the velocity distributions of the resonating ions in the presence of ICRF heating.

However, if the radial widths of the orbits are taken into account, equation 2.31 becomes three dimensional, and three invariants are required. With the invariants (E, Λ, P_ϕ), where $\Lambda = \frac{\mu B_0}{E}$, and B_0 is the magnetic field at the axis, the orbit averaged quasi-linear operator takes the form [40]

$$\langle Q(f) \rangle = \sum_N L_N (D^N_{RF} L_N f) \tag{2.32}$$

where

$$L_N = \frac{\partial}{\partial E} + \frac{n\omega_{c0} - \Lambda\omega}{\omega E} \frac{\partial}{\partial \Lambda} + \frac{N}{\omega} \frac{\partial}{\partial P_\phi}, \tag{2.33}$$

and the diffusion coefficient is given by

$$D^N_{RF} = \frac{1}{4\omega^2} \sum_R \frac{(Ze)^2}{|n\dot{\omega}_{cR}|} v^2_{\perp R} \left[E_+ J_{n-1} \left(\frac{k_\perp v_{\perp R}}{\omega_{cR}} \right) + E_- J_{n+1} \left(\frac{k_\perp v_{\perp R}}{\omega_{cR}} \right) \right]^2, \tag{2.34}$$

the subscript R refers to a quantity evaluated at a resonance.

Chapter 3

Modelling of ICRH with the PION code

In this chapter an explanation of the steps to model ICRH and of the PION code used for the analysis at JET is made. As mentioned in section (2.6), the modelling of ICRH can be divided into two main parts. Here a description of the way to perform the power deposition calculation, the Fokker-Planck calculation and the coupling of both calculations is made.

In the late eighties at JET, quantities directly affected by ICRF heated fast ions began to be measured routinely: non-thermal neutron rates, fast ion energy contents, etc. PION was designed as a simplified wave modelling code. The PION approach includes the most important effects of ICRH and the results obtained are robust. PION has been extensively used and benchmarked against JET results [12, 13, 24, 41–45] and also other fusion devices such as AUG [46–49], Tore Supra[50, 51], DIII-D [52], ITER [53, 54] and DEMO [55].

3.1 The PION code

PION is a code based on simplified models to obtain results in a fast way. PION is able to solve the evolution in time of the distribution function and to compute the absorption of the electromagnetic wave. As commented in section 2.6 this problem must be solved self-consistently. PION simulations consist of a number of time steps. First of all, for each time step, the power absorbed is calculated. This information is then used for computing the distribution function with a Fokker-Planck model, which will be used to compute the absorption power at the beginning of the next time step, and so on.

Other codes can be used, for example, using a full wave code coupled with a two dimensional Fokker-Planck code, but these codes need long execution times, while PION, solving a 1D Fokker-Planck equation, is an ideal code to analyze a big number of discharges performed in tokamaks. A discharge stands for an experiment with plasma performed in a tokamak. Typically, the experiment is set up in such a way so that a particular physical aspect is assessed. The scheme that PION uses to compute the power deposition and the evolution of the distribution function is now presented.

3.1.1 Power deposition

The power deposition model was developed by Hellsten and Villard [56]. It is based on fundamental observation of wave fields in a tokamak. The model was partly obtained by analysing results from the full wave code LION [57, 58]. Therefore, the deposition profiles are in good agreement with those obtained with LION.

By Fourier decomposing the launched wave in the toroidal direction and calculating the power deposition for each toroidal mode number one can compute the power deposition [56, 59]. The model is based on a superposition of two components, one in the limit of strong absorption and the other in the limit of weak absorption. For a strong absorption, the damping is focused at the first passage of the wave, and the power deposition is controlled by Doppler broadening of the cyclotron resonance (equation 1.3b). While for weak absorption, the wave field fills much of the poloidal cross section, and the power deposition is determined by the wave field distribution and the absorption strength along the cyclotron resonance.

The averaged Poynting flux within a flux surface for a toroidal mode number N and a given Fourier mode is

$$P(s) = \alpha_s P_s(s) + (1 + \alpha_s) P_2(s), \tag{3.1}$$

where $P_s(s) = \sum_j P_{sj}(s)$ and $P_2(s) = \sum_j P_{wj}(s)$ stand for strong and weak absorption, respectively. The sum runs over all the resonating ion species and electrons, α_s is a constant and $s = \left(\frac{\psi_p - \psi_{p0}}{\psi_{pa} - \psi_{p0}}\right)^{\frac{1}{2}}$ is a normalized flux surface, where ψ_p is the poloidal flux and the subscripts a and 0 represent the plasma boundary and the center of the magnetic axis, respectively. As commented before, P_s and P_w depend on different quantities, $P_{sj} = P_{sj}(s, N, \langle v_{\|j}^2 \rangle)$ and $P_{wj} = P_{wj}(s, a_j(s), F(s))$, where $\langle v_{\|j}^2 \rangle$ is the averaged square parallel velocity of species j. $a_j(s)$ is the absorption strength of species j along the cyclotron resonance and the function $F(s)$ represents the averaged electric wave field strength along the cyclotron resonance in the limit of weak absorption. The

expressions for direct electron damping, which is due to electron Landau damping (ELD) and Transit Time Magnetic Pumping (TTMP) are more complicated and can be found in [59].

The locally averaged flux surface power density is

$$p(s) = \frac{\frac{dP(s)}{ds}}{\frac{dV}{ds}} \tag{3.2}$$

where dV is the volume enclosed by a flux surface. The constant α_s is given by $\alpha_s = a_s^2(2 - a_s)$ which is obtained empirically [56], and

$$a_s = \frac{\omega}{2\pi P_x} \int Im(\vec{E}^* \cdot \bar{\varepsilon} \cdot \vec{E}) dx \tag{3.3}$$

is the single pass absorption coefficient calculated in the mid-plane (the horizontal plane through the magnetic axis),* denotes a complex conjugated quantity, P_x is the incoming Poynting flux and the x axis is across the resonance layer. It is important to mention that, recently, a study of a statistical model of the wave field in a bounded domain found the value $\alpha_s = a_s^2(2 - a_s)$ from theoretical principles [60]. The contributions from different particle species to the single pass absorption coefficient are calculated using the Wentzel-Kramers-Brillouin (WKB) approximation, which in the absence of mode conversion gives

$$a_s = \sum_j a_{sj} = \sum_j \int_{-\infty}^{\infty} \frac{k_0^2}{|k_\perp|} \left\{ Im(\varepsilon_{xx}^j) \left| \frac{\varepsilon_{xy}}{\varepsilon_{xx} - n_\parallel^2} \right|^2 + Im(\varepsilon_{yy}^j) + 2Re(\varepsilon_{xy}^j) Im \left[\frac{\varepsilon_{xy}}{\varepsilon_{xx} - n_\parallel^2} \right] \right\} \times e^{-\int_{-\infty}^{x} 2Im(k_\perp(x'))dx'} dx \tag{3.4}$$

where ε^j is the contribution of the ion species j to the dielectric tensor, and $k_0 = \frac{\omega}{c}$.

3.1.2 Fokker-Planck calculation

The evolution of the velocity distribution function can be described by a Fokker-Planck equation 2.31. In order to reduce the computing time, the full two-dimensional velocity distribution is not solved. Instead, the one-dimensional pitch-angle-averaged Fokker-Planck equation is solved [41],

$$\frac{\partial f}{\partial t} = \frac{1}{v^2} \frac{\partial}{\partial v} \left[-\alpha v^2 f + \frac{1}{2} \frac{\partial}{\partial v} (\beta v^2 f) \right] + \frac{1}{v^2} \frac{\partial}{\partial v} \left[v^2 D_{RF} \frac{\partial f}{\partial v} \right] + S, \tag{3.5}$$

where the first term on the right-hand side is the collisional operator while the second term is the wave-particle interaction operator. The S term is a source term for the NBI, this is especially important in those discharges where beams are in resonance with the wave. This term allows to take into account the ICRF+NBI synergy and it becomes specially important in chapter 5. The diffusion coefficient is

$$D_{RF} = \sum_N K \left| J_{n-1}\left(\frac{k_\perp v_\perp}{\omega_{ci}}\right) + \frac{E_-}{E_+} J_{n+1}\left(\frac{k_\perp v_\perp}{\omega_{ci}}\right)\right|^2, \tag{3.6}$$

where K is a constant proportional to $|E_+|^2$, the collisional coefficients α and β can be found in [13].

The averaged square parallel velocity $\langle v_{\|j}^2 \rangle$ which is needed for the power deposition calculation is obtained with an *ad hoc* formula [26],

$$\langle v_{\|j}^2 \rangle = \frac{\int \mu_{eff}^2 v^2 f(v) dv}{\int v^2 f(v) dv} \tag{3.7}$$

where the effective averaged-pitch-angle is calculated as,

$$\mu_{eff}^2 = \frac{1}{3} \frac{1 + \left(\frac{v}{v_*}\right)^2}{1 + \left(\frac{v}{v_*}\right)^2 + \left(\frac{v}{v_*}\right)^4}, \tag{3.8}$$

with $v_* = 0.5 v_\gamma$. Here, v_γ is a characteristic velocity above which pitch angle scattering becomes weak [39]. The ratio between v_* and v_γ has been obtained by fitting the expression in equation 3.8 to calculations of μ_{eff}^2 made with the 2D Fokker-Planck code BAFIC [61].

Finite orbit widths can play an important role for the fast ions produced by ICRH. For example, the energy density of the fast ions and the collisional power transfer to the background plasma can be significantly affected. Finite orbit width effects are taken into account in PION by assuming that the fast ICRH accelerated ions are trapped and that they have turning points close to the cyclotron resonance ($\omega \approx n\omega_{ci}$). The collision coefficients used in the Fokker-Planck calculation are then averaged over the resulting orbits. This means that a fast trapped ion is identified with the flux surface it has its turning point on, which is also near where the ion interacts resonantly with the wave field.

3.1.3 Coupling of Fokker-Planck and power deposition calculations

The model for the distribution function presented above is sufficient to calculate most of the quantities which are normally of interest, such as the collisional power density transfer from resonating ion species to the background ions and electrons, energy density (parallel and perpendicular) of the resonating ion species and fusion reactivity. The Fokker-Planck calculation also provides parameters which are needed to evaluate the dielectric tensor components used in the power deposition calculation (including finite Larmor radius terms to all orders in the anti-Hermitian part). In order to make the absorption strength in the power deposition calculation consistent with the Fokker-Planck calculation, we use a simplified model for the dielectric tensor [62]. This model requires three parameters, in addition to $\langle v_{\|j}^2 \rangle$. These parameters are described below.

For each toroidal mode number N, the ICRH diffusion tensor, D_{RF}, can be divided into three components:

$$D_{RF,N}^{+} = K_N \left| J_{n-1}\left(\frac{k_\perp v_\perp}{\omega_{ci}}\right)\right|^2 \tag{3.9a}$$

$$D_{RF,N}^{-} = K_N \left| \frac{E_-}{E_+} J_{n+1}\left(\frac{k_\perp v_\perp}{\omega_{ci}}\right)\right|^2 \tag{3.9b}$$

$$D_{RF,N}^{c} = 2K_N Re\left[\frac{E_-}{E_+} J_{n+1}\left(\frac{k_\perp v_\perp}{\omega_{ci}}\right) J_{n-1}\left(\frac{k_\perp v_\perp}{\omega_{ci}}\right)\right] \tag{3.9c}$$

The power density absorbed due to these components by species j from a wave with a toroidal mode number N can be written as,

$$p_{\sigma,N}^{j} = 2\pi m_j \int_0^\infty \frac{1}{v^2}\frac{\partial}{\partial v}(v^3 D_{RF,N}^{\sigma}) f_j v^2 dv, \quad \sigma = +,-,c. \tag{3.10}$$

There are three factors used in the power deposition calculations,

$$\gamma_{+,N}^{j} = \frac{p_{+,N}^{j}}{p_{+,N}^{jM}}, \quad \gamma_{-,N}^{j} = \frac{p_{-,N}^{j}}{p_{-,N}^{jM}}, \quad \gamma_{c,N}^{j} = \frac{p_{c,N}^{j}}{p_{c,N}^{jM}}, \tag{3.11}$$

where the superscript M stands for Maxwellian. So these are the ratios between the actual distribution function and a Maxwellian function with the same density as the actual distribution function but with temperature $n_j kT = \frac{1}{2} m \langle v_{\|j}^2 \rangle$.

These three factors are used to compute the dielectric tensor $\bar{\varepsilon}$. Neglecting the parallel electric wave field, the local absorbed power can be written as,

$$\begin{aligned} p^j_{RF} =& \frac{\omega}{2\pi} Im(\vec{E}^* \cdot \bar{\varepsilon} \cdot \vec{E}) = \frac{\omega}{2\pi}\{|E_+|^2 \left[Im(\varepsilon^j_{xx} + \varepsilon^j_{yy}) - 2Re\varepsilon^j_{xy}\right] + \\ &+ |E_-|^2 \left[Im(\varepsilon^j_{xx} + \varepsilon^j_{yy}) + 2Re\varepsilon^j_{xy}\right] + 2Re(E_+E^*_-)Im(\varepsilon^j_{xx} - \varepsilon^j_{yy})\}. \end{aligned} \tag{3.12}$$

Thus, the absorption strength in the power deposition calculation is consistent with that in the Fokker-Planck calculation when the following relations hold:

$$Im(\varepsilon^j_{xx} + \varepsilon^j_{yy}) - 2Re(\varepsilon^j_{xy}) = \gamma^j_{+,N}\left[Im(\varepsilon^{j,M}_{xx} + \varepsilon^{j,M}_{yy}) - 2Re(\varepsilon^{j,M}_{xy})\right] \tag{3.13a}$$

$$Im(\varepsilon^j_{xx} + \varepsilon^j_{yy}) + 2Re(\varepsilon^j_{xy}) = \gamma^j_{-,N}\left[Im(\varepsilon^{j,M}_{xx} + \varepsilon^{j,M}_{yy}) + 2Re(\varepsilon^{j,M}_{xy})\right] \tag{3.13b}$$

$$Im(\varepsilon^j_{xx} - \varepsilon^j_{yy}) = \gamma^j_{c,N}\left[Im(\varepsilon^{j,M}_{xx} - \varepsilon^{j,M}_{yy})\right]. \tag{3.13c}$$

From the above equations one can find the anti-Hermitian parts of the dielectric tensor, $Im(\varepsilon^j_{xx})$, $Im(\varepsilon^j_{yy})$ and $Re(\varepsilon^j_{xy})$, in terms of the gamma factors (equation 3.11) and the Maxwellian contributions to the dielectric tensor which can be found in textbooks. Corrections to the Hermitian parts are more difficult to calculate and a simple approximation is used [62] in PION.

The flow chart presented in figure 3.1 summarizes the logical sequence of the PION code. First, the background plasma parameters are read, such as plasma temperature and density, the magnetic equilibrium and the antenna configuration. If this is the first call to the code, Maxwellian distribution functions are assumed for resonant species. The dielectric permittivity is computed with the calculated distribution function of resonant species and the power deposition is then obtained. After the resonant ions have damped the wave, a new Fokker-Planck calculation is performed to obtain the new distribution function at $t_{n+1} = t_n + \Delta t$. The calculation then computes the new permittivity to obtain a new deposition profile and so on.

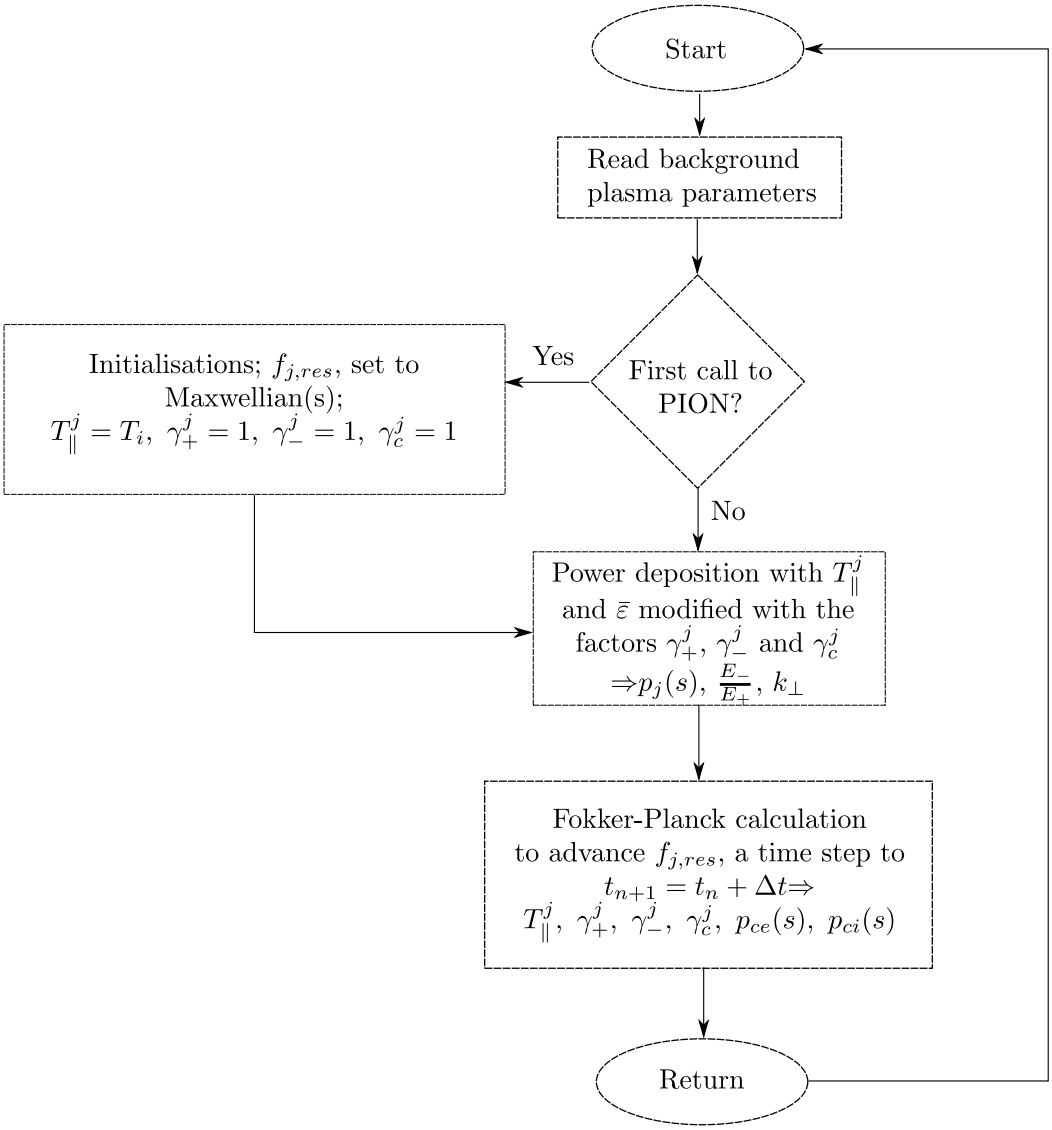

Fig. 3.1 Flow chart of the PION code.

Chapter 4

Impurity accumulation control with ICRH waves

One of the main concerns for reaching high-performance discharges is to control impurities. More precisely, to avoid high-Z impurities to reach the plasma core where plasma densities and temperatures are typically higher. The reason for this is that radiation losses increase with density and exponentially with the atomic number and temperature, therefore, it is necessary to keep the plasma core clean from impurities to avoid radiative collapse of the discharge. In this chapter a study of the impurity accumulation control with ICRH waves is given for a set of hybrid discharges. Furthermore, the role of fast ions in controlling core impurity accumulation is studied taking into account finite orbit width (FOW) effects. This study shows that fast ions' contribution is small as compared to the thermal part. In previous studies such as in [19, 22] it was shown that fast ions played an important role in temperature screening. Temperature screening is the ability of ions and electrons to prevent impurity accumulation by the peaking of their central temperature profile and reaching steep temperature gradients which favours outward impurity flux (see equation 4.1). However, when FOW effects are modelled, the gradient of the fast ion temperature is effectively reduced and their contribution tends to be negligible. Therefore, the most important effect on temperature screening is by the peaking of the electron temperature through ion-electron collisions [63]. Other publications have now taken into account FOW effects and obtained similar results as shown here [20].

This work has been published in Publications 1-3 (c.f. pages xxii-xxiii).

4.1 Introduction

The current plasma wall facing components of the installed ITER-Like-Wall (ILW) at JET are made of tungsten (W) in the divertor, beryllium (Be) for the limiters

and exposed inconnel in the main chamber. Tungsten possesses a high temperature tolerance and low erosion rate which make it a strong candidate for the future ITER reactor. However, dilution by any high-Z impurities need to be controled and minimised to a concentration below 10^{-4} in a fusion plasma reactor in order to achieve high-performance discharges.

Following the discussion in [19, 22] the W flux can be described as:

$$\Gamma_W \sim n_i T_i \nu_{iW} Z_W \left(\frac{R}{L_{n_i}} - 0.5 \frac{R}{L_{T_i}} \right). \tag{4.1}$$

Here, n_i and T_i are the ion density and temperature, respectively, $\nu_{iW} \sim T_i^{-3/2}$ is the background ion-tungsten collision frequency, R is the major radius and L_{n_i} and L_{T_i} are the inverse of the logarithmic gradient of ion density and temperature, respectively. For ion temperature gradient terms larger than the ion density gradient term, central W accumulation is avoided as the flux convection becomes outward.

Recent studies [19, 21–23] have proved ICRF heating as an efficient mechanism to avoid central impurity accumulation, mainly through avoidance of poloidal asymmetries and enhancement of temperature screening. Poloidal asymmetries are the higher concentration of high-Z impurities found at the LFS as a result of their higher mass and, therefore, their centrifugal force. In the presence of ICRF heating, temperature screening in equation 4.1 is effectively increased by the fast minority temperature screening $\sim n_f T_f^{-1/2} R/L_{T_f}$ as n_f and ∇T_i tend to increase under these conditions. Furthermore, fast minority ions tend to become trapped in banana orbits that are localised at the low-field side (LFS) and create a poloidal varying potential that push W to the high-field side (HFS), effectively reducing the poloidal asymmetries as a result of W accumulation at the LFS by plasma rotation. Poloidal asymmetries have been identified to enhance neoclassical transport and to be the main mechanism for central tungsten accumulation [19, 64].

In this study the analysis has been focused on JET hybrid discharges with different ICRF resonance positions. Two discharges suffered central impurity accumulation accompanied by MHD activity. MHD activity has been reported as the cause of triggering impurity accumulation in hybrid discharges in Ref. [65]. Here, an analysis of the differences of ICRF heating profiles for a scan in the resonance position is performed and temperature screening factors associated with fast minority ions are calculated taking into account orbit width effects. However, modelling of W transport has not been carried out as it is out of the scope of the present thesis.

4.2 Effect of resonance position on ICRF heating and impurity control

This first analysis was necessary as to know the limits for off-axis heating and proceed with the rest of the discharges. The resonance position has an impact on the heating profile and also on the impurity accumulation. The analysis of impurity accumulation is complex as many mechanisms are involved in the transport of high-Z impurities. One of such mechanisms is the temperature screening provided by fast ions generated through ICRF heating. Here, the impurity screening associated to H minority and the ICRF heating profiles are computed using PION for discharges where the resonance position was varied.

The ICRF resonance position was varied in a total of five hybrid discharges in order to assess its impact on the ICRF impurity control. As $R_{res} \propto B_T$, the magnetic field B_T was modified accordingly so as to place the ICRF resonance at different major radii ranging from $R_{res} = 2.75$ m (high-field-side) to $R_{res} = 3.2$ m (low-field-side) while the magnetic axis was located at around $R_0 = 3.0$. There are only a limited sets of antenna frequencies available at JET. Therefore, in order to scan the resonance position, the toroidal magnetic field is varied for a given antenna frequency. Notice that all evolving input parameters such as magnetic field or antenna frequency are taken into account in PION. A total of 30 MW of combined external heating power was used [66], consisting of 25 MW of NBI and 5 MW of ICRF at a frequency of 42 MHz. An overview of these discharges is shown in figure 4.1. In order to keep a similar central safety factor among these discharges, the starting time of the external power heating, i.e. ICRF and NBI heating, was delayed 0.25 s for each B_T change of 0.1 T. Figure 4.1 shows that those discharges with a resonance $|R_{res} - R_0| > 15$ cm suffered from MHD activity and impurity accumulation in these plasma conditions. The MHD modes (m/n) that were present in the HFS discharge 92311 were 3/2 and 4/3 and assuming the EFIT safety factor profile they were located at s = 0.28 and s = 0.03, respectively. For the LFS discharge 92313 the modes were 5/3 and 4/3 located at s = 0.34 and s = 0.03, respectively. We have selected three discharges as shown in table 4.1 for detailed analysis. Two discharges that had radiation peaking (92311 and 92313) and a central discharge that did not show radiation peaking, we selected 92314, however, 92306 is very similar too.We refer to them from now on by their ICRF resonance position: HFS, central and LFS.

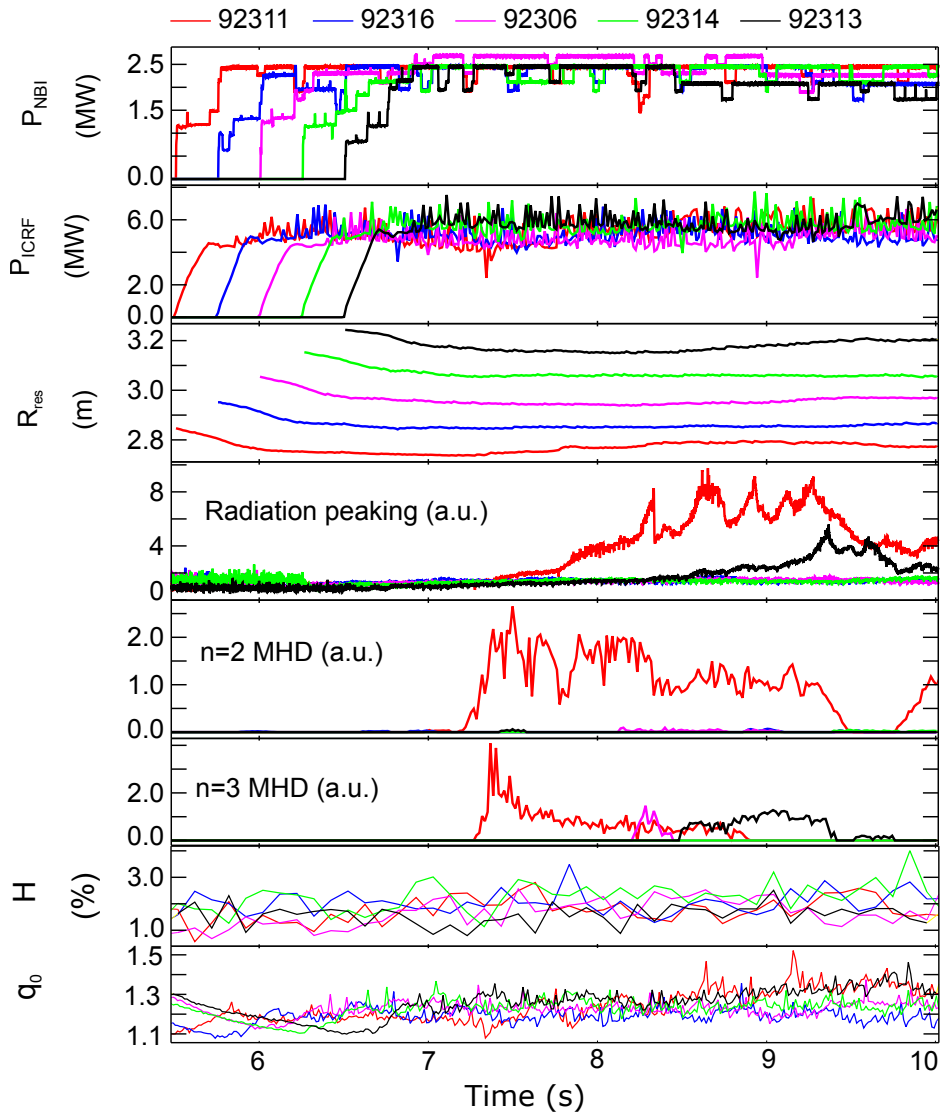

Fig. 4.1 *Overview of five hybrid discharges with combined NBI+ICRF heating at different toroidal magnetic fields to vary the ICRF resonance location: 2.6, 2.7, 2.8, 2.9 and 3.0 T in discharge 92311, 92316, 92306, 92314 and 92313, respectively. The start time of external heating was modified to match the central safety factor at the heating onset.*

	92311	92314	92313
ICRF resonance pos.	HFS	Central	LFS

Table 4.1 ICRF resonance position for discharges 92311, 92313 and 92314.

Figure 4.2 shows the electron temperature and density for the HFS, central and LFS discharges. During the MHD activity that occurred in the HFS and LFS discharges the central electron density became peaked.

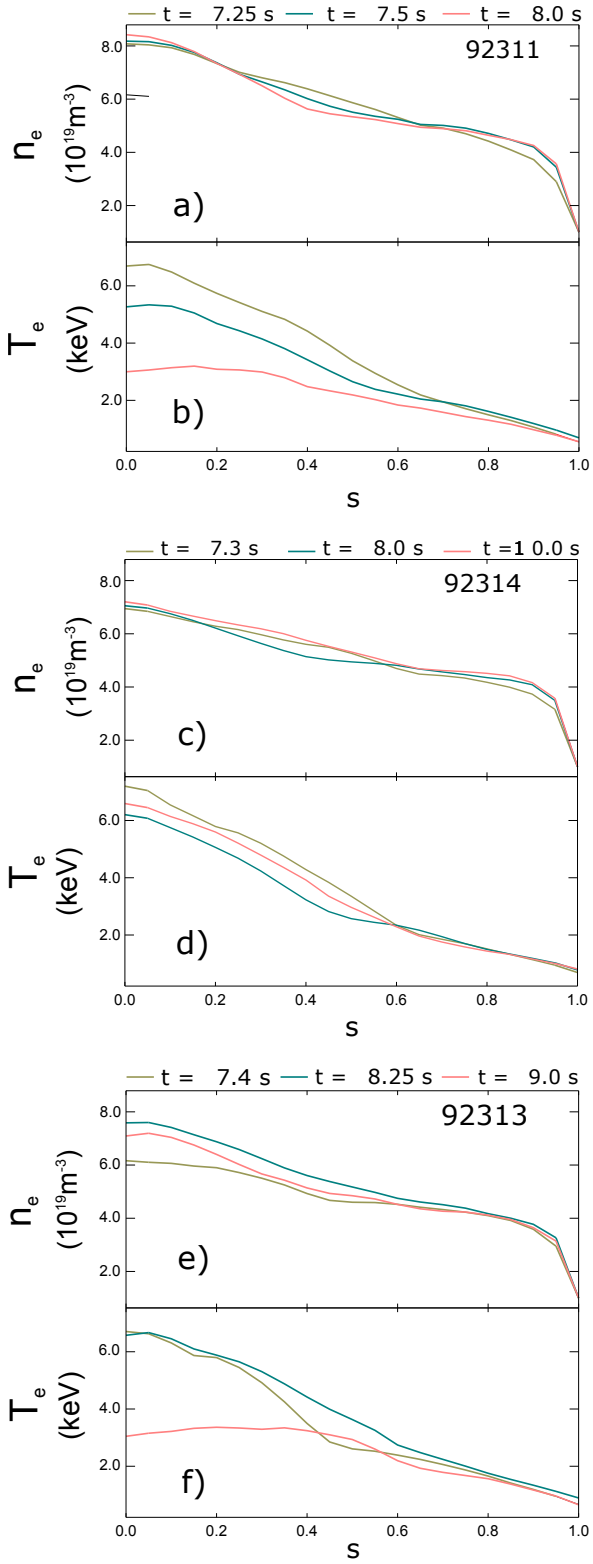

Fig. 4.2 *Electron density and temperature as measured by the LIDAR, for HFS discharge 92311 a) and b), central discharge 92314 c) and d) and LFS discharge 92313 e) and f) at different time points. Here, s is the square-root of the normalised poloidal flux. Appearance of MHD and impurity accumulation take place around 7.5 s and 8.5 s for discharges 92311 and 92313, respectively.*

While the central electron temperature decreased and became flat in the centre, both effects enhance inward convection (4.1) which resulted in central impurity accumulation. Most of the impurity radiation is due to W, the central W concentration ranges from $2.0 \cdot 10^{-5}$ at the early phase of the discharges to $1.5 \cdot 10^{-4}$ at the end. The concentration stays relatively constant at $1.5 - 2.0 \cdot 10^{-4}$ during the MHD activity. However, using the bolometer signals and assuming $Z_{\text{eff}} = 2.0$, taking Be as the only other impurity there is 10-30% missing radiation which belongs to a contribution of other mid-/high-Z impurities such as Ni and Mo. Regarding fusion performance, figure 4.3 shows that only the discharge with a central resonance avoided impurity accumulation and maintained steady values for β_N, neutron production rate and electron temperature.

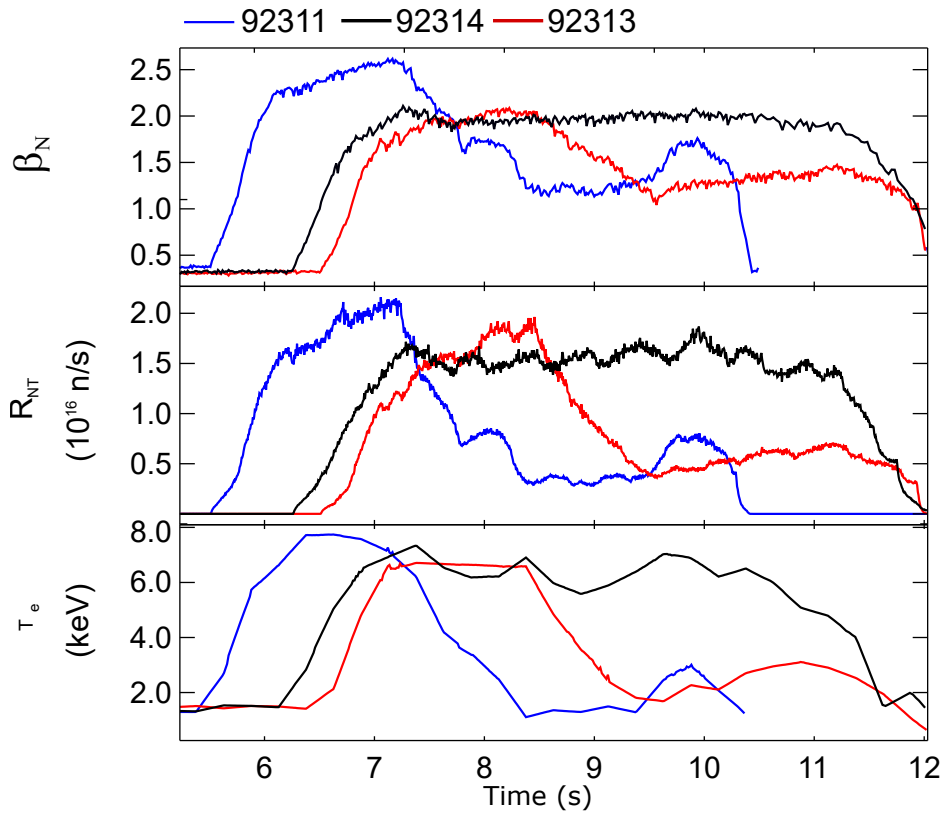

Fig. 4.3 *Measured values for β_N, neutron production rate and electron temperature for discharges 92311 (HFS), 92314 (central) and 92313 (LFS).*

The modelled heating profiles (figure 4.4) show differences as the resonance changes from the HFS to the LFS. The evaluation of the heating profile provides valuable information regarding where the wave energy is being deposited and how strong the fast ion pressure can be expected. Typically, central power deposition is preferable ($s < 0.3$) in order to obtain peaked plasma temperature profiles. PION takes into account

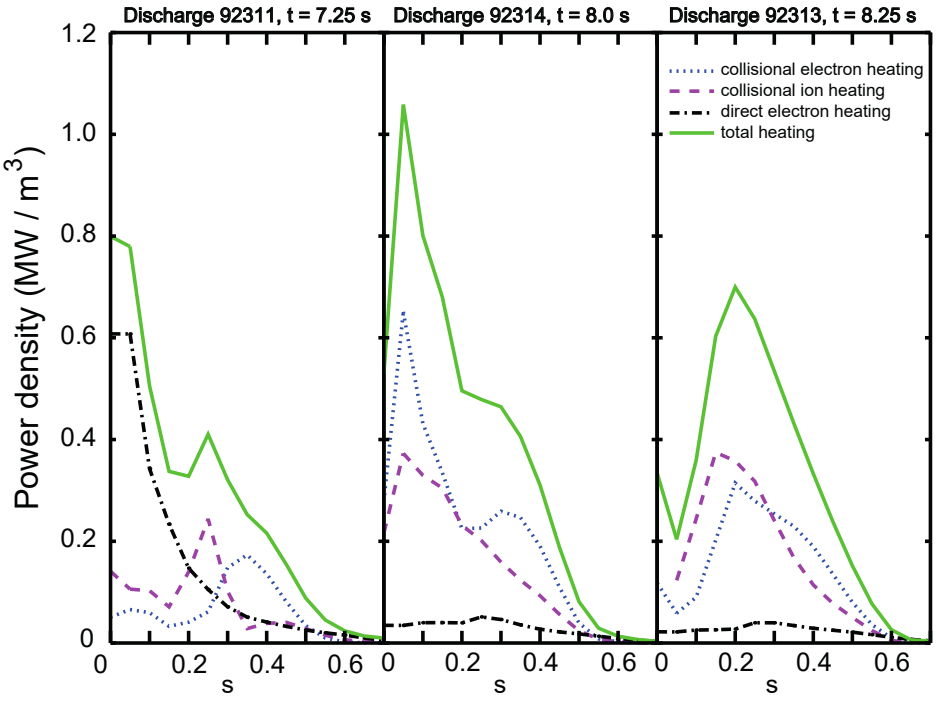

Fig. 4.4 *Power density profiles for collisional ion heating, collisional electron heating, direct electron heating and total plasma heating due to ICRF waves as given by PION for discharges 92311, 92314 and 92313 with a HFS, central and LFS ICRF resonance, respectively.The profiles are shown after 1.75 s from the start of the main heating. The right y-axis has been normalised to the average ICRF input power of 5MW.*

orbit width effects which tend to broaden the orbits of the fastest ions and, therefore, collisional electron heating profile broadens with respect to bulk ion heating. Notice that changes in the toroidal magnetic field affect the orbit width as it is proportional to the Larmor radius, however it is limited to variations of ±10% for these set of discharges. Figure 4.4 shows that ion heating is marginally central for the HFS discharge as bulk ion heating peaks at s = 0.25 and collisional electron heating at s = 0.35, for the central discharge the power deposition peaks at the centre around s = 0.1 and for the LFS around s = 0.2. PION predicts strong central direct electron damping for HFS resonance discharge as T_e peaks at the centre (equation 5.1) and there are no other competing damping mechanisms. It becomes almost negligible as the resonance is placed towards the LFS, increasing from the edge until the competing ion damping mechanisms become dominant. In fact, the highest electron temperature was obtained in the HFS discharge until the appearance of MHD and impurity accumulation (figure 4.3). The power density of bulk ion heating and collisional electron heating are higher for central and LFS discharges. The dominant heating mechanism in the central

discharge is collisional electron heating which is beneficial to avoid central impurity accumulation as higher fast ion pressure and more peaked plasma temperature profiles are expected. The LFS discharge shows a similar bulk ion heating and collisional electron heating with the total heating power peak located off-axis around s = 0.2 while in the other two cases the total heating power peak is located in the centre. The ICRF power partition varies with the resonance position, however, other factors such as different temperatures and densities also play a role. The volume integrated average heating fractions as computed by PION are shown in table 4.2 for each discharge.

	HFS (%)	Central (%)	LFS (%)
Fundamental H	50	60	50
2^{nd} harmonic D	15	30	40
Direct electron damping	35	10	10

Table 4.2 ICRF volume integrated power fraction for fundamental H, 2^{nd} harmonic D and direct electron damping as calculated by PION.

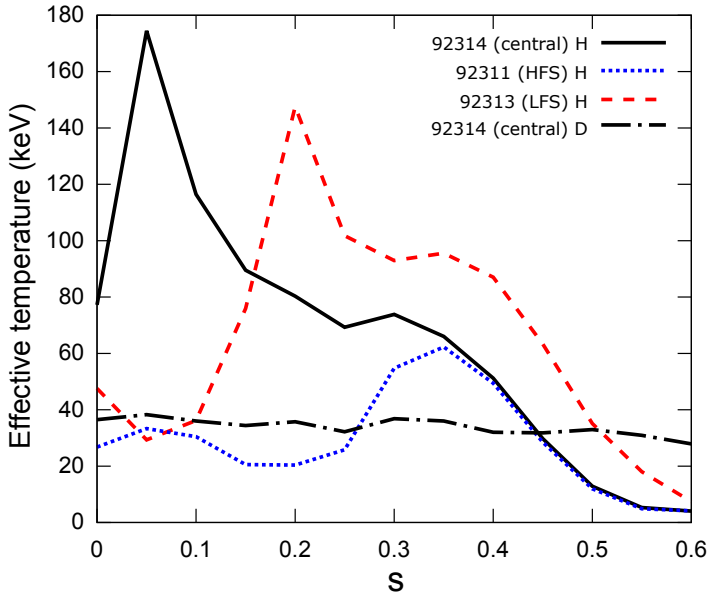

Fig. 4.5 *Effective temperature of hydrogen minority ions for discharges 92311 (dotted), 92313 (dashed) and 92314 (solid). The dotted-dashed line is the D effective temperature for the central discharge.*

The heating profiles predicted by PION have a direct impact on the calculated fast ion effective temperature; not only on the average energy of the fast ion population but also on the position where the effective temperature is maximum which is important in order to compute the temperature gradients associated with the impurity screening (4.1).

Figure 4.5 shows the effective temperature of fast minority for the HFS, central and LFS discharges. Also shown is the effective temperature for D for the central case, which is virtually the same in all discharges. The effective temperature for D has no gradient as predicted by PION and, therefore, only temperature screening associated to H minority ions is calculated. The effective temperature has been computed using $T_{\rm f} = \frac{2E_{\rm f}}{3n_{\rm f}}$ where $n_{\rm f}$ and $E_{\rm f}$ refer to the fast H minority density and energy density, respectively. Notice that the effective temperature broadens due to orbit width effects. We have evaluated the temperature screening by fast minority ions in comparison to the relative temperature screening associated to thermal D as $\Gamma_{\rm f,H}/\Gamma_{\rm th,D} = n_{\rm f,H}T_{\rm th,D}^{1/2}L_{\rm th,D}/(n_{\rm th,D}T_{\rm f,H}^{1/2}L_{\rm f,H})$, where $L_{th,D}$ and $L_{f,H}$ are the inverse of the logarithmic temperature gradient for thermal D and fast H. The gradient has been calculated over the s values shown in table 4.3, such as L_i uses $\mathrm{s}_{i+1} - \mathrm{s}_i$. The thermal and fast densities of H and D are shown in figures 4.6 and 4.7.

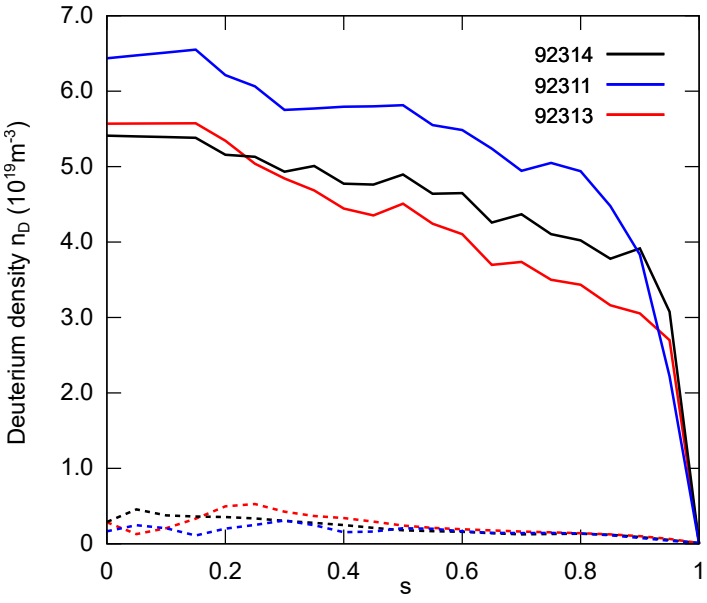

Fig. 4.6 *Thermal (solid) and fast ion densities (dashed) for D for discharges 92311 (blue), 92313 (red) and 92314 (black).*

The results of our analysis are shown in table 4.3. These results show that under these conditions impurity screening from fast minority ions is of the order of few percent with respect to that from thermal D. The central discharge shows the highest values for temperature screening in the centre. The HFS discharge has the lowest values of temperature screening except at s = 0.15 and a negative value at s = 0.25 as a result of a positive temperature gradient which enhances the inward flux. In a similar way the LFS discharge has negative values at s = 0.10 and s = 0.15. These modelling results

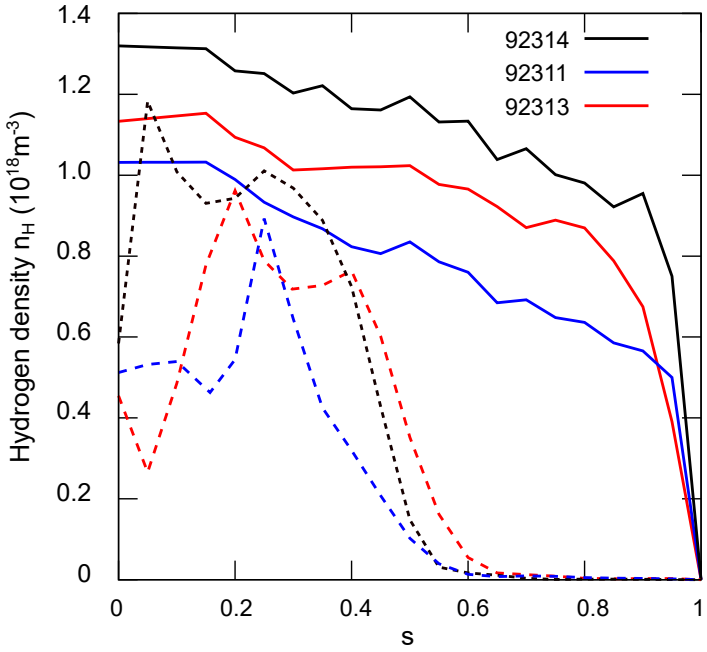

Fig. 4.7 *Thermal (solid) and fast ion densities (dashed) for H for discharges 92311 (blue), 92313 (red) and 92314 (black).*

s	HFS (%)	Central (%)	LFS (%)
0.05	0.8	2.0	1.3
0.10	0.2	1.4	-1.2
0.15	2.0	1.0	-2.7
0.20	0.8	1.3	2.6
0.25	-4.0	0.0	-0.1

Table 4.3 Computed temperature screening factor of H minority normalised to temperature screening factor provided by thermal D ($\Gamma_{f,H}/\Gamma_{th,D}$) for discharges 92311 (HFS), 92314 (central) and 92313 (LFS).

show that central ICRF heating is beneficial to avoid impurity accumulation as in other studies where it has been studied in detail [15, 22, 23]. However, it is difficult to draw firm conclusions regarding the relevance of fast minority ions among other mechanisms in these conditions as the experimental data show MHD activity and radiation peaking at the same time. For the rest of the hybrid discharges, central ICRF resonance was used.

4.3 Conclusions

Avoidance of impurity accumulation to prevent disruptions and radiation losses is critical to reach high-performance conditions. In particular, high-Z impurities such as W or mid-Z impurities such as Be, both present in JET-ILW, need to be controlled and minimised. In this chapter, a review of the role of fast resonant ions and the localisation of the resonance position has been given. As shown in previous works, central deposition reaches the best results in terms of controlling impurities in the plasma core by peaking the electron temperature (through ion-electron collisions) and flattening the plasma density. Off-axis deposition experiments performed poorly in terms of impurity control and they eventually were dominated by MHD activity and important radiation losses until disruption. However, HFS deposition is an interesting scheme which tends to enhance direct electron absorption and reaches good performance until the appearance of the MHD activity.

The PION code which computes the finite orbit widths, was updated to compute the impurity screening due to fast resonant ions. It was shown that their contribution is small as compared to the background plasma and can be neglected. The finite orbit width tends to broaden the effective temperature profile which effectively decreases the impurity screening strength of fast ions, this effect was not taken into account in other publications and lead to the understanding that fast ions were playing a bigger role. Moreover, heating off-axis makes fast ions to contribute negatively in the impurity screening. The contribution to impurity screening from D beams was also found to be small since the effective temperature remains flat with no gradient.

The conclusion from this study is that under this hybrid configuration in order to avoid MHD activity and impurity accumulation the ICRF resonance must be placed in a region around $|R_{res} - R_0| \leq 15$cm, i.e., central deposition.

Chapter 5

High-Performance at JET

This chapter tackles the heating characteristics of a hybrid high-performance discharge and its main features are analysed, especially those related to plasma performance. Following the results obtained in chapter 4 a series of high-performing discharges were performed in JET. In particular, one discharge reached a neutron rate record which is studied in detail in this chapter.

This study hinges around a D-D plasma and how to maximise its performance from the heating point of view. A series of guidelines are presented and demonstrated through a number of experiments that culminated in a neutron record discharge. An extrapolation to a D-T plasma is also studied, nevertheless, a more comprehensive study on D-T prediction is given in chapter 6. The material of this chapter has been published in Publications 1-2 (c.f. pages xxii-xxiii).

5.1 Introduction

Three damping mechanisms compete in the discharges studied in this chapter, i.e., the ion cyclotron resonance of H through fundamental hydrogen resonance ($\omega = \omega_H$) and of D through 2$^{\text{nd}}$ D harmonic resonance ($\omega = 2\omega_D$), direct electron damping via electron Landau Damping (ELD) and transit time magnetic pumping (TTMP). Direct electron damping may play an important role in discharges with high electron densities and temperatures and when the resonance position is located at the high-field side (HFS). For the plasma temperatures and densities of this hybrid high-performing discharges, direct electron damping typically damps 10-20% of the wave energy. As a reference, a theoretical expression for direct electron damping in H minority and bulk D plasmas is

given as in[67]

$$2\eta \simeq L\frac{\pi^{1/2}}{2}\frac{\omega}{\Omega_D}\frac{\omega_{pD}}{c}\beta_e\zeta_e e^{-\zeta_e^2}, \tag{5.1}$$

where 2η is the optical depth where the wave arriving at the minority cyclotron resonance is absorbed by a single-pass absorption factor, $A = 1 - e^{-2\eta}$, $L \simeq 2a/3$ is an effective radial absorption length assuming $\zeta_e \simeq 1$, $\zeta_e = \omega/k_\parallel v_{te}$, $v_{te} = (2T_e/m_e)^{1/2}$, β_e is the bulk electron beta, Ω_D is the fundamental D cyclotron angular frequency and ω_{PD} is the deuterium angular plasma frequency. Direct electron damping is typically maximum on axis where T_e peaks.

Fundamental H damping is particularly important during the ramp-up, when the plasma is still cold and in the absence of D beams. The 2$^{\text{nd}}$ D harmonic depends strongly on the velocity distribution of D, becoming more relevant as an energetic D tail develops, i.e. with the D beams. The local power partition between D harmonic and H fundamental can be approximated by calculating the second moment of the Fokker-Planck RF operator and including FLR effects to the lowest order in the Taylor expansion of the diffusion coefficient for the 2$^{\text{nd}}$ D harmonic as done in [24, 41]:

$$\frac{p_2}{p_1} = c_{21}\frac{k_\perp^2 w_2}{n_1 m_1 \omega_{c2}^2}. \tag{5.2}$$

Here, the subscripts 1 and 2 refer to the resonant species with a fundamental and a 2$^{\text{nd}}$ harmonic resonance, respectively, p_1 and p_2 are the local power densities absorbed by H and D, respectively, $k_\perp$ is the perpendicular wavenumber, w_2 is the energy density of deuterium, n_1 and m_1 are the hydrogen density and mass, respectively, ω_{c2} is the cyclotron frequency of D and c_{21} is a constant. The analysis of JET high-performance hybrid discharges with PION shows that $c_{21} \approx 0.2-0.3$. This parameter is not universal as it may vary for different scenarios. The value is calculated as an average for different power absorption ratios given by PION for discharges presented in this study.

In the experiments we lowered the H concentration so the D power absorption increased, as can be seen in (5.2). Another important factor is the D beam injection which increases substantially the D energy density and consequently the D power absorption. These two joint effects contributed to achieving the highest fusion yield that has been reached in the hybrid discharges.

For the D-T prediction we have considered two ICRF scenarios, ^{3}He minority and H minority. Strong ion cyclotron damping by ^{3}He minority is predicted by PION. ^{3}He absorbs most of the wave energy during all the stages of the discharge, in contrast with the H minority damping performance which typically becomes weaker as D beams are

injected. For this scenario the equation (5.2) is still valid, taking into account that subscripts 1 and 2 refer to ^{3}He and T, respectively. The computed value of constant c_{21} based on PION results is $c_{21} \approx 0.01 - 0.02$.

The 3$^{\text{rd}}$ harmonic resonance must be taken into account in the D-T prediction with D and T beams when the minority species considered is H. For H minority in D-T plasma, the damping performance from resonant H and D ions is similar to that from a pure D plasma. In fact, the 3$^{\text{rd}}$ T harmonic resonance does not play a relevant role as it absorbs a small fraction of the wave energy, which is negligible compared to that absorbed by H or D. In order to understand this behavior, we have obtained an equation that describes the local power partition for the 3$^{\text{rd}}$ harmonic using the same procedure to compute (5.2), for a full derivation of this formula we refer to annex A. The local power partition between the 3$^{\text{rd}}$ harmonic, fundamental and 2$^{\text{nd}}$ harmonic resonant ions scales as,

$$\frac{p_3}{p_1} = c_{31}\frac{m_3 k_\perp^4}{m_1 n_1 \omega_{c3}^4}\int v_3^4 f_3 dv,\ \frac{p_3}{p_2} = c_{32}\frac{m_3 k_\perp^2 \omega_{c2}^2}{\omega_{c3}^4 w_2}\int v_3^4 f_3 dv. \tag{5.3}$$

The main difference from (5.2) comes from the presence of the 4th moment of the distribution function which needs to be computed numerically and the different exponents in the wave number and the cyclotron frequency. However, by assessing the order of magnitude of the terms $k_\perp^2 w_2/\omega_{c2}^2$ from (5.2) and $k_\perp^4 m_3 \int v_3^4 f_3 dv/\omega_{c3}^4$ from (5.3). For typical values of the scenarios studied we find that there are approximately two orders of magnitude of difference between the term in (5.2) and (5.3), the higher being the term in (5.2). This theoretical approximation explains the weak damping strength observed for the 3$^{\text{rd}}$ T harmonic resonance in the simulations performed with PION.

Bulk ion heating is beneficial to increase the number of thermal fusion reactions. In order to obtain strong bulk ion heating the fast ions average energy should not surpass a threshold energy, the so called critical energy. In the process of thermalisation, energetic ions will slow-down by colliding with background ions and electrons, this effect increases the thermal ion and electron temperature, respectively. The energy threshold at which thermal ions and electrons are equally heated, the so-called critical energy, was introduced in chapter 2 and is reintroduced here for convenience,

$$E_{crit} = 14.8 A T_e \left[\sum_j \frac{n_j Z_j^2}{n_e A_j}\right]^{\frac{2}{3}}. \tag{5.4}$$

Here A is the atomic mass of the resonant ion species, T_e is the electron temperature, n_j and n_e are the densities of the j-ith ion species and electrons, respectively, Z_j and A_j are the atomic number and atomic mass of the j-ith ion species, respectively.

The velocity distribution of the resonant ions plays a crucial role in the way the collisional power is transferred. The average fast ion energy must be kept below the critical energy for dominant bulk ion heating. An energetic ion of energy E transfers its energy following $\dot{W}_i/\dot{W}_e = (E_{crit}/E)^{3/2}$ where $\dot{W}_i$ and $\dot{W}_e$ are the rate of energy transfer to thermal ions and electrons, respectively, while E is the energy of the non-thermal ion [36]. This is the instantaneous ratio of energy transfer from an ion to thermal ions and electrons, for a complete slowing-down one needs to integrate over all the energy states of the ion until thermalisation is reached. Here, we show the ratio of the total energy given up by a single ion of energy E to thermal ions after a complete thermalisation as done by Stix in [36] and, as an extension to this work, we have integrated this ratio over a gaussian centered at the average ion temperature T_i and a Maxwellian for D and H, respectively, which gives an approximation of the energy transferred from fast ions to thermal ions in a simplified case. However, ICRF heating through 2$^{\text{nd}}$ D harmonic resonance drives a strong tail in the D velocity distribution function which is non-Maxwellian and, therefore, figure 5.1 must be understood as a rough estimation. It has been computed as $\int_0^E G(E)f(E)dE$, where $G(E)$ is the average fraction of the energy transferred from fast ions to thermal ions as defined in [36] and $f(E)$ is a maxwellian distribution for fast ions (figure 5.1). From the

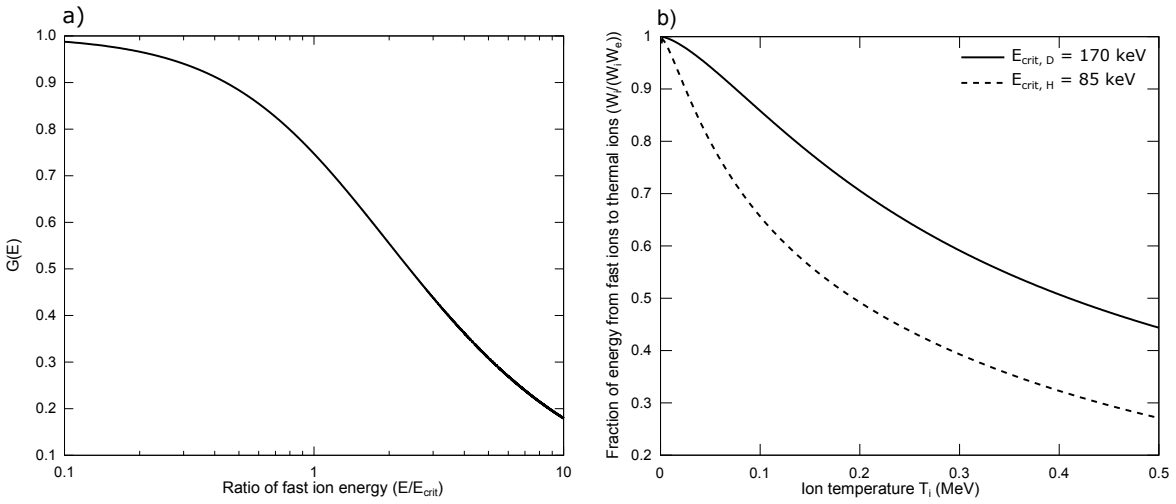

Fig. 5.1 *a) Ratio of energy $G(E)$ given up by a fast ion to thermal ions over a complete thermalisation as in [36], b) $G(E)$ averaged over a gaussian and a maxwellian for different thermodynamic ion temperatures T_i and fixed critical energies for D and H, respectively, $E_{crit,D} = 170$ and $E_{crit,H} = 85$ keV.*

simplified calculation shown in figure 5.1b) one expects to have dominant bulk ion heating from fast H ions for the discharges considered in this chapter. This is not the case during the ramp-up where resonant H ions typically reach an average energy in the range of 500 keV and, as will be shown, collisions with electrons are dominant. The average fast ion energy is calculated using the fast ion density energy content and the fast ion density $\langle E_f \rangle = \frac{w_f}{n_f}$ as predicted by PION.Taking into account that D beams are injected at an energy around 110 keV, dominant bulk ion heating is expected (figure 5.1 b), and the addition of ICRF heating can bring a fraction of D ions to energy levels closer or even above the D critical energy. This high energy tail in the D distribution function will lead to a different behaviour for D-D and D-T plasmas in terms of neutron rate production due to differences in the fusion cross section.

5.2 Effect of hydrogen concentration on plasma performance

One of the goals was to assess the impact of the H concentration on the ICRF heating and optimisation of fusion performance. It is known that the H minority concentration plays a key role in the ICRF power partitioning (equation 5.2) between H and majority D and beam-injected D ions which has an impact in the bulk ion heating and the fusion yield enhancement [24]. A set of discharges with different H concentration was implemented (figure 5.2). In all cases, central heating was performed in order to avoid MHD activity and impurity accumulation as seen in chapter 4. The same plasma composition and plasma parameters were kept in these discharges while only changing the H concentration, see table 5.1 [18]. Here, we quote the H concentration $n_H/(n_H + n_D)$ as deduced from the ratio of the D_α and H_α light collected along lines of sight through the plasma. Penning gauge spectroscopy in the divertor gave somewhat higher $n_H/(n_H + n_D)$ of 3-4%. The radial profiles for the plasma temperature and density are very similar as shown in figure 5.3 for three different times, between the three discharges.

According to our modelling, however, the experimental results are more consistent with the values deduced from the D_α and H_α light (figure 5.4). The main results in the experimental observations (figure 5.2) are the differences in the fusion yield for the three discharges. In the early stage of the heating phase, up to t = 8 s, discharge with the lowest H puff shows a faster rise in the neutron yield. A lower H concentration leads to a larger D damping of the wave energy (figure 5.5), accelerating them to higher energies with respect to the other discharges (figure 5.6). As the plasma density grows,

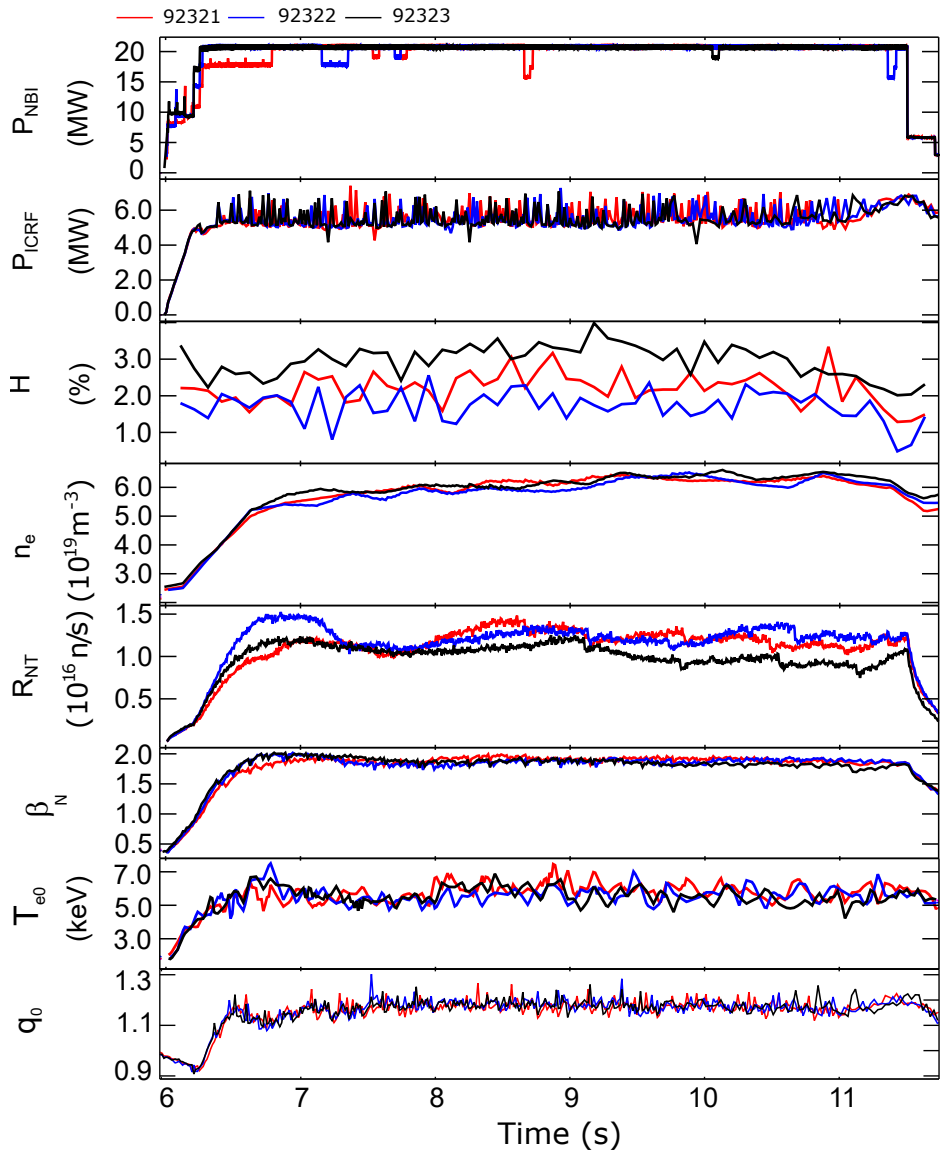

Fig. 5.2 *Overview of three hybrid discharges with three different H concentrations. Different neutron rates are obtained for similar plasma parameters and power input as a consequence of slight variations in the H concentration. The H concentration data (dashed) has been smoothed (solid) for this plot.*

the difference in the neutron rate is reduced. From t = 8 s onwards, the fusion yield of the discharge with the lowest H concentration is on average ∼20% higher than in the discharge with the highest H concentration, which we interpret as being due to a stronger ICRF-accelerated fast deuterium tail.

The experimental results are in line with our modelling results. Figure 5.4 shows the simulated neutron rates for the three discharges which are consistent with the

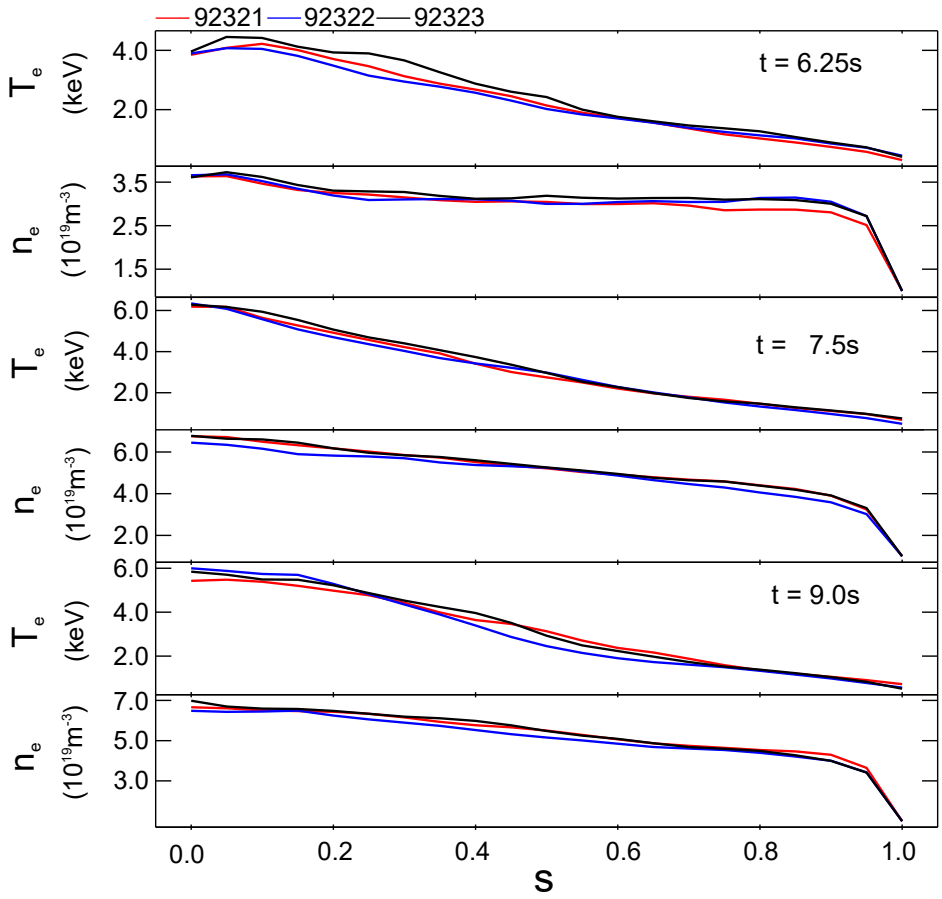

Fig. 5.3 *Radial profiles for plasma temperature and density. The profiles are shown at three different times, during the ramp up t = 6.25s and during the main heating phase, t = 7.5 and 9.0.*

	92321	92322	92323
$n_H/(n_H + n_D)$ (%)	1.5-3.0	1.0-2.0	2.5-4.0

Table 5.1 The range of H concentration for discharges in the H concentration scan.

measured neutron rates [66]. The difference between the discharge with the lowest H concentration and the discharge with the highest concentration is about 0-25% which is in good agreement with the experimental results. The difference vary as the H concentration is not constant throughout the discharge, the H(%) showed in figure 5.2 has been smoothed for a better visualisation. The ICRF wave was tuned for a central $\omega = \omega_{cH} = 2\omega_{cD}$ resonance for the three discharges. The variation of H concentration has a direct impact on the power partition between the H and D ions, this is shown in figure 5.5 at t = 10.0 s during the main heating phase. To first order, the ratio of H to D damping scales roughly as $n_H/(n_H + n_D)$, as expected. A comparison with

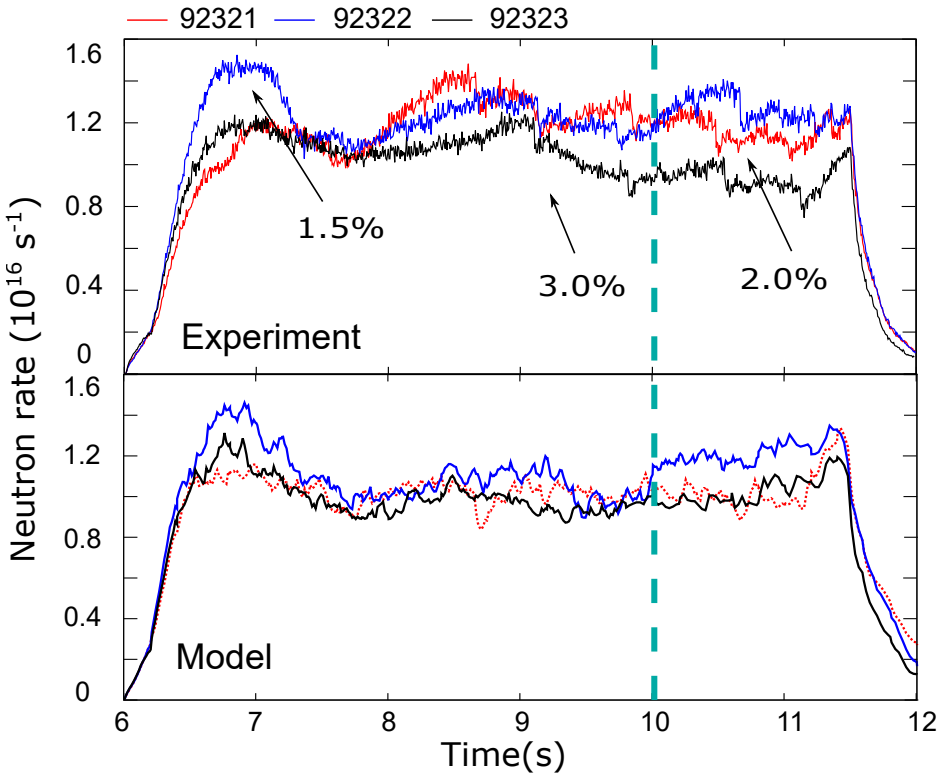

Fig. 5.4 *Comparison of experimental neutron emission rate (top) for discharges 92321, 92322 and 92323 with a H concentration of about 2%, 1.5% and 3%, respectively. Modelled neutron emission rate of the H scan discharges (bottom). The vertical dashed line marks the time point at which the ICRF heating profiles are shown.*

the numerical result and the analytical approximation (equation 5.2) for the local power partition at the resonance is given in table 5.2. Both, numerical and analytical, follow the same trend, higher absorption from 2$^{\text{nd}}$ D harmonic resonance for lower H concentrations. PION follows the changes in the H concentration throughout the

	92321	92322	92323
PION p_2/p_1	1.43	2.68	0.63
Eq. 5.2 p_2/p_1	1.94	2.26	0.64

Table 5.2 Local power fractions between H and D at the resonance position as computed by PION and as the analytical approximation equation 5.2 with $c_{21} = 0.2$ for t = 10.0s.

discharge and although the H concentration for these discharges is low, notice that small differences in the H concentration play a relevant role in this scenario as they have an impact in the way plasma damps the ICRF wave energy and consequently in the plasma performance. This is clearly evident in figure 5.6 where a lower H concentration leads to a stronger highly energetic D tail, further enhancing fusion

performance as the second harmonic D damping has an advantageous effect on the fusion yield. Notice that H distribution is more energetic in the discharge with higher H concentration, in fact it stays dominant in front of the D distribution until around the E = 1.1MeV. The D velocity distribution function shows the same trend in the PION modelling and in the measurements with the neutron time-of-flight spectrometer TOFOR [68–70]. However, PION predicts a stronger D tail as compared to TOFOR for the discharge with the highest H concentration. For the comparison we have volume integrated the PION distributions inside s = 0.35 where most of the TOFOR signals come from and we have averaged the distributions over the given TOFOR time window. The distributions are normalised so as to have 1 at E = 150keV. Notice that the cross section for D-D fusion reactions peak at the MeV range and, therefore, strengthening the ICRF-accelerated deuterium tail enhances the fusion neutron rate for this particular case. As it is shown in figure 5.5, after the deuterium beams have

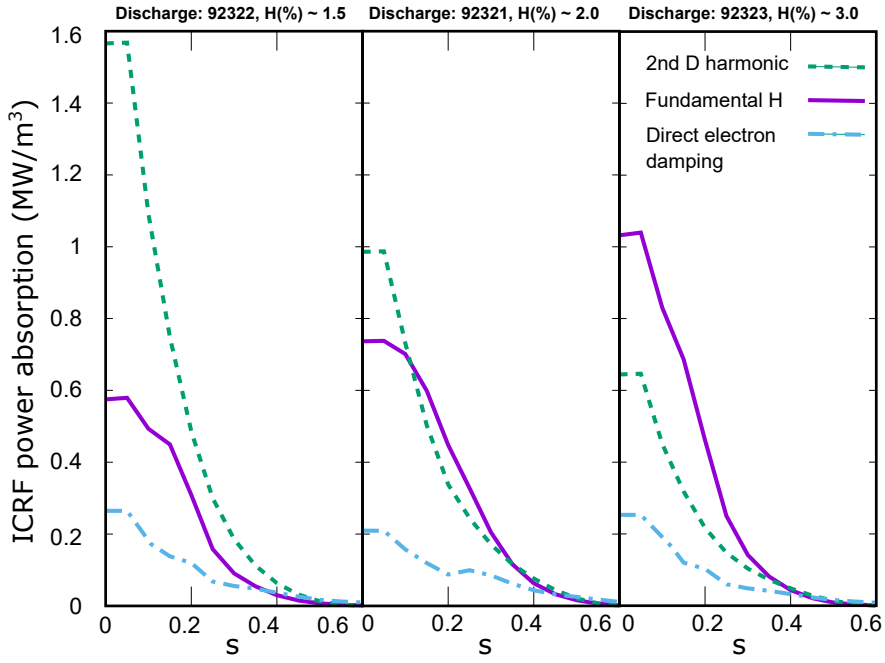

Fig. 5.5 *ICRF power absorption profile for fundamental H (solid), 2nd D harmonic resonance (dashed) and direct electron damping (dashed-dotted) during the main heating phase at t = 10.0 s. The ICRF power absorption has been normalised to the average input ICRF power of 5MW (right y-axis).*

been injected, 2nd D harmonic resonance becomes the main damping mechanism at the plasma centre for the two lowest H concentration discharges once the plasma core gets hotter, while fundamental H resonance dominates (figure 5.7) for low plasma densities and temperatures that take place during the ramp up (figure 5.2 and figure 5.3).

Fundamental heating becomes more relevant at low temperatures as compared to 2nd harmonic heating since the RF diffusion is low at low temperatures for harmonic heating while it is higher for fundamental heating. This fact together with the low plasma density which decreases the critical energy and the collisionality favours the creation of energetic H ions which mainly collide with electrons. Other mechanisms can also influence the power absorption such as the q-profile, however there is a minor variation of q at the centre (figure 5.2) of around 15% from the ramp up to the main heating phase, for which PION does not predict differences in the power absorption fraction. Small to no differences are predicted by PION with regards to direct electron damping, therefore, varying the H concentration in a small range has no impact in the total fraction of energy absorbed by ions and electrons but only in the competing damping mechanisms by ion species.

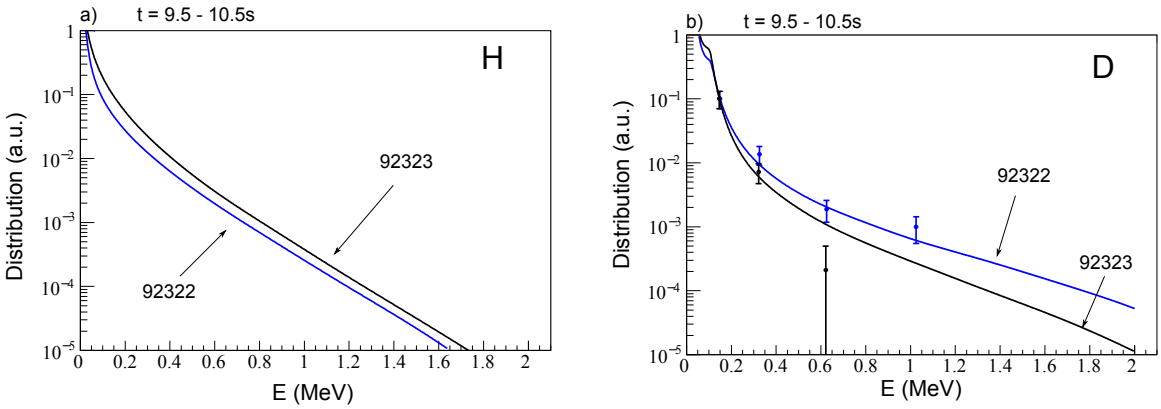

Fig. 5.6 *Energy distribution functions of a) hydrogen and b) deuterium in logarithmic scale for discharges 92322 (blue) and 92323 (black) with a H concentration of about 1.5% and 3%, respectively. a) PION velocity distribution for H and b) PION velocity distribution for D and as deduced from measurements with the neutron time-of-flight spectrometer TOFOR (dots).*

Figure 5.7 shows the time evolution of fundamental H absorption, 2nd D harmonic absorption and direct electron damping for discharges with the lowest and highest H concentration. Similar behaviour is observed in the way damping mechanisms evolve, i.e. fundamental H damping dominates during the ramp up while it decays once the D beams are injected as they produce a rapid increase of the 2nd D harmonic damping strength. As the H concentration decreased from 3% to 1.5%, D damping increased from 35% to 50% and H damping decreased from 50% to 35% in average, while direct electron damping stayed roughly the same, i.e. 15% of the total ICRF power. Notice the decrease in H absorption for both cases around t = 11s as a consequence of the

decrease in H concentration (figure 5.2) followed by an increase around t = 11.5s as the NBI beams are stopped around t = 11.3s.

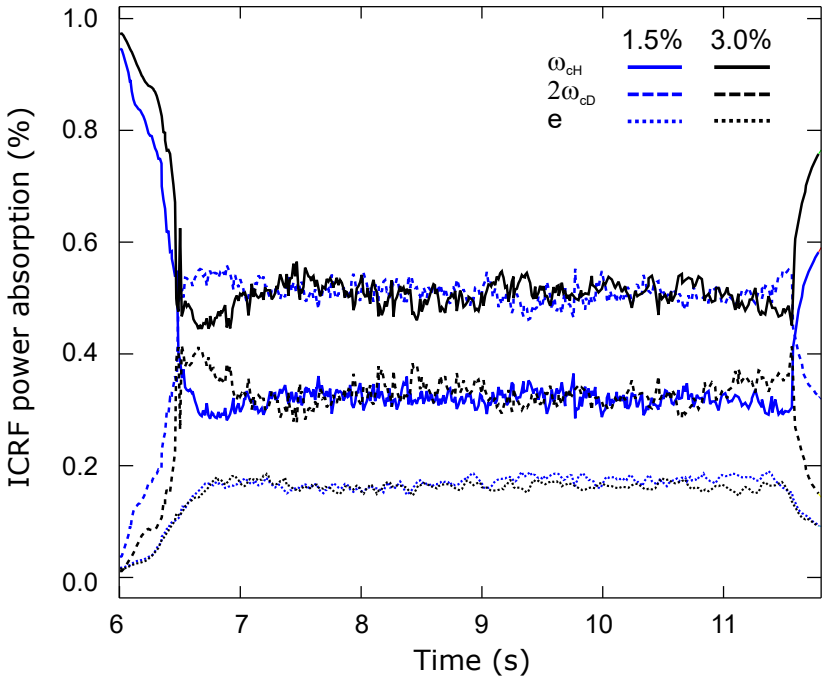

Fig. 5.7 *Damping fractions of the total ICRF power with fundamental hydrogen absorption (solid), 2nd deuterium harmonic absorption (dashed) and direct electron damping (dotted) for discharges 92322 (blue) and 92323 (black). The D NBI power is stopped down at around t = 11.3s, resulting in the decrease in D damping fraction.*

5.3 High-performance hybrid discharge

From the point of view of fusion neutron rate, the aim was to improve the previous record of $2.3 \cdot 10^{16}$ n/s from the hybrid discharge 86614. The neutron rate record was achieved in several discharges and here, we study the combined effect of ICRF and NBI heating in one of the best shots with $B_T = 2.8$ T and $I_p = 2.2$ MA, discharge 92398. Similarly to other hybrid discharges, 5 MW of ICRF power was tuned to a central fundamental H and second D harmonic resonance ($\omega = \omega_H = 2\omega_D$) using a frequency of 42.5 MHz as in previous discharges. Together with deuterium NBI power of 26 MW, the total external heating power was 31 MW. An overview of the high performing hybrid discharge 92398 is presented in figure 5.8. The neutron rate was

increased to its steady-state value of $2.7 \cdot 10^{16}$ s^{-1} and the normalised plasma beta to 2.7, when stationary high-performance plasma was obtained.

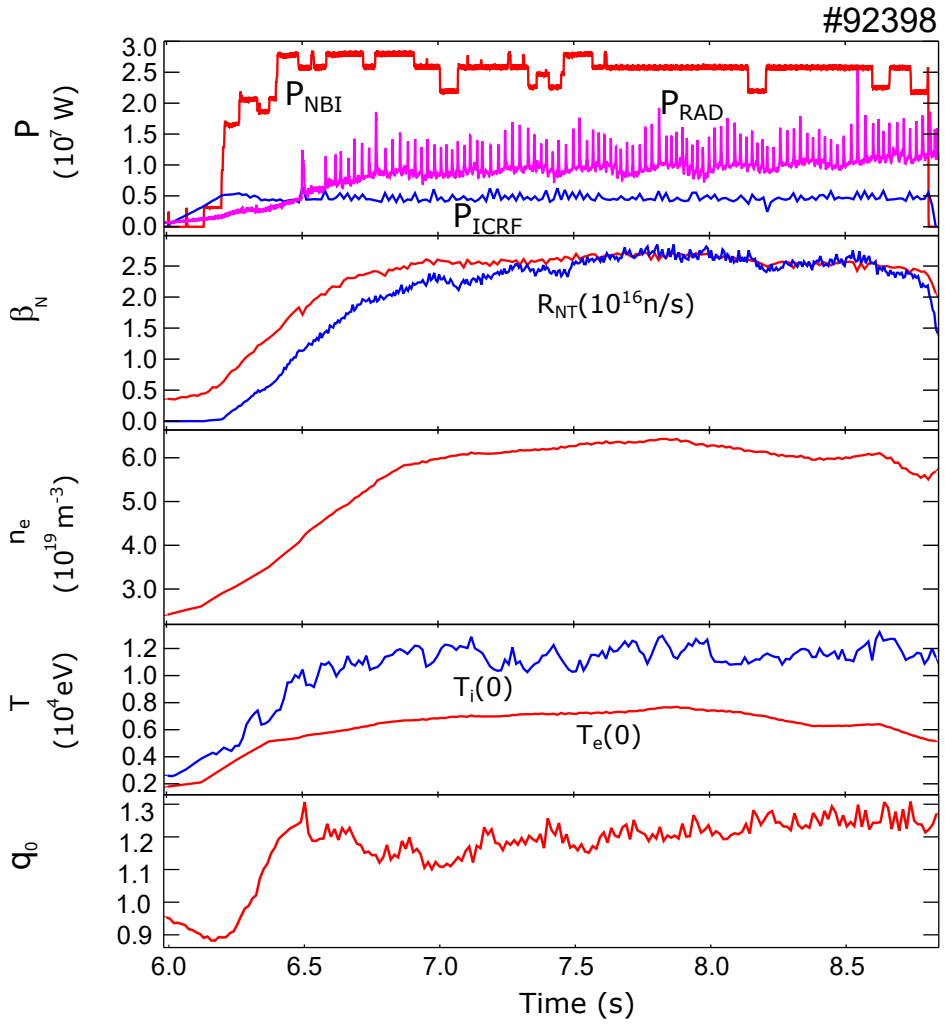

Fig. 5.8 *Overview of the high performing hybrid dicharge 92398. A factor $R = T_i/T_e$ has been applied to the T_i as measured by the X-ray crystal spectroscopy (XCS) diagnostic.*

The experimental ion temperature T_i has been computed using the T_i/T_e ratio as deduced from the X-ray crystal spectroscopy data. This data suggests that the T_i/T_e ratio is around 1.25-1.6. The H concentration $n_H/(n_H + n_D)$ deduced from the ratio of the D_α and H_α light collected along lines of sight through the plasma is ~2% and has been used to model this discharge. The calculated and experimental neutron yield are in good agreement as shown in figure 5.9. However, several uncertainties associated with the experimental measurements have been taken into account to assess their impact on the neutron yield (shaded area in figure 5.9). In particular, the upper limit of the shaded area represents the neutron rate value for a simulation assuming

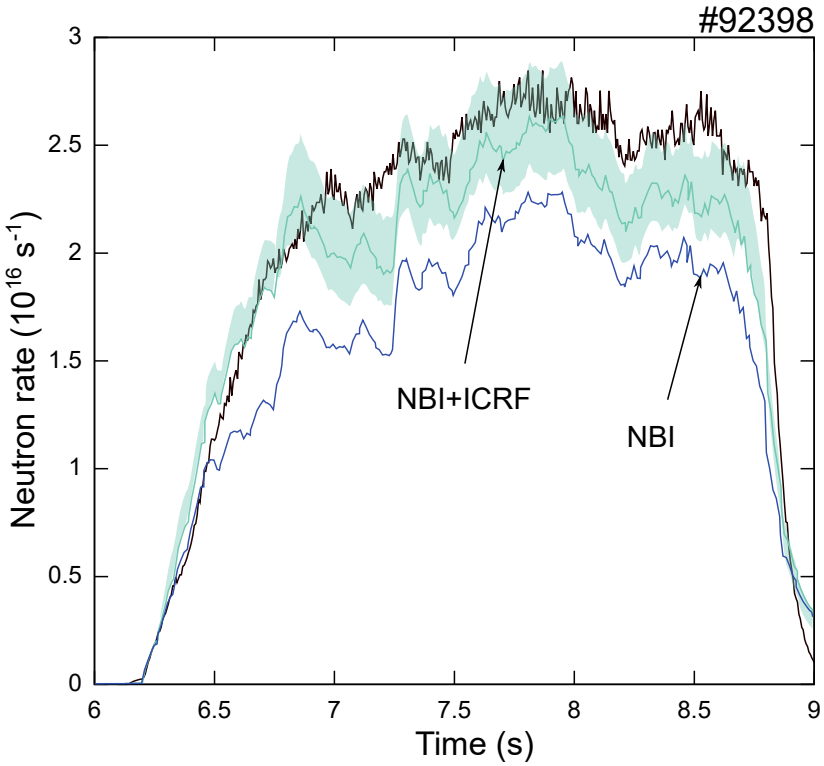

Fig. 5.9 *Neutron production rate of discharge 92398. The solid black line is the experimentally measured neutron rate, the other two lines labelled as NBI+ICRF and NBI refer to the PION modelling for the total input power heating and only NBI, respectively. The shaded area shows the assumed error in the modelling due to uncertainties in the input ion temperature and impurity concentrations.*

the maximum measured ratio by the XCS diagnostic of $Ti/Te = 1.6$ while the lower limit is for $T_i/T_e = 1.25$. The impurity content has been varied for $\pm 2\%$ around the measured impurity densities, the variation caused in the neutron rate falls inside the estimated error area. However, the modelled neutron rate is, in general, lower than the measured one. The reason for this might be that the ion temperature is higher or the H concentration slightly lower. It is difficult to assess the exact value of the measurements, specially for these two diagnostics, so we decided to cover the full range of T_i temperatures as given by the XCS diagnostic and use the H concentration as deduced by the ratio of the D_α and H_α light. Radial profiles during the ramp up and main heating phase are provided in figure 5.10. One of the main goals was to evaluate the impact of ICRF enhancement in the fusion yield. In order to do so, the neutron rate has been modelled in two different ways, one which takes into account the full external power and a second one which only models the NBI heating (figure 5.9). The NBI only case has been modelled with PION with zero antenna power and using

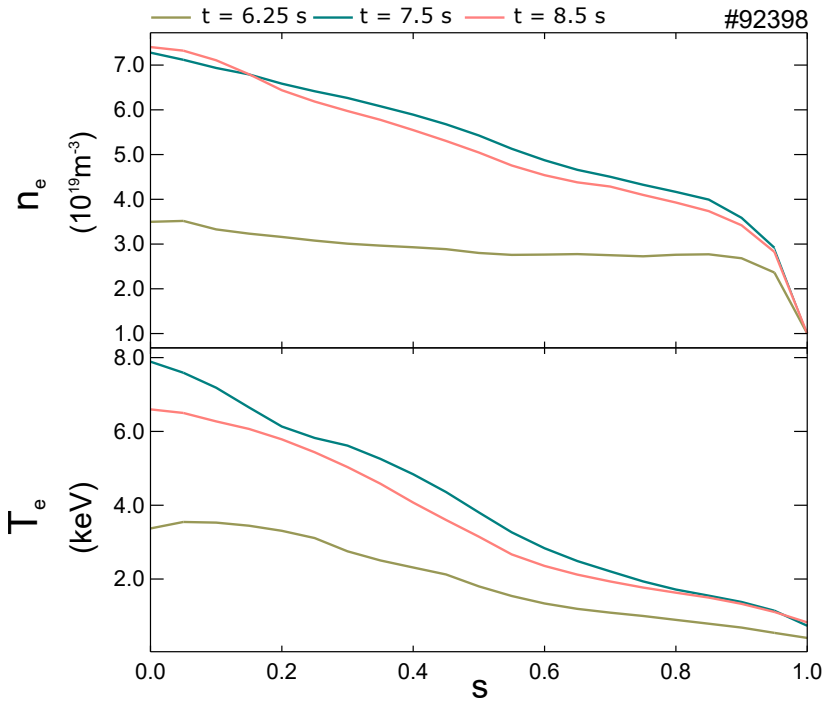

Fig. 5.10 *Plasma density and temperature profiles for discharge 92398, at t = 6.25s during the ramp up and at t = 7.5 and 8.5s during the main heating phase.*

the beam source terms from PENCIL. The ICRF enhancement is calculated from the difference between the associated neutron yields for both heating mechanisms as $\mathrm{RF}(\%) = \frac{\mathrm{R_{NT}(NBI{+}ICRF) - R_{NT}(NBI)}}{\mathrm{R_{NT}(NBI{+}ICRF)}}$. Figure 5.11 shows good agreement between the ICRF enhancement as estimated from a spectroscopic analysis of data collected by the neutron time-of-flight spectrometer TOFOR and as predicted by the PION code. Detailed explanation on the TOFOR neutron spectrum from NBI heating is provided in [71]. The enhancement varies throughout the discharge, starting at a maximum value of around 35% during the ramp-up phase and reaching a steady value of 15% during the main heating phase. This variation is the result of an increasing plasma density and temperature, as neutron emission from D beams and thermal reactions increase and, therefore, the ICRF enhancement is reduced until a steady value. However, notice that this enhancement does not extrapolate to D-T scenario as will be shown in chapter 6 since the fusion cross sections σ_{DT} and σ_{DD} are different.

In order to maximise the ICRF fusion enhancement in this scenario, it is crucial that D ions absorb most of the ICRF wave power and the presence of a high bulk ion heating as mentioned previously. The damping mechanisms competing in this discharge are the same as those described in section 5.2 and the physics are similar. During the ramp-up, fundamental H absorbs almost all the wave power while 2^{nd} D

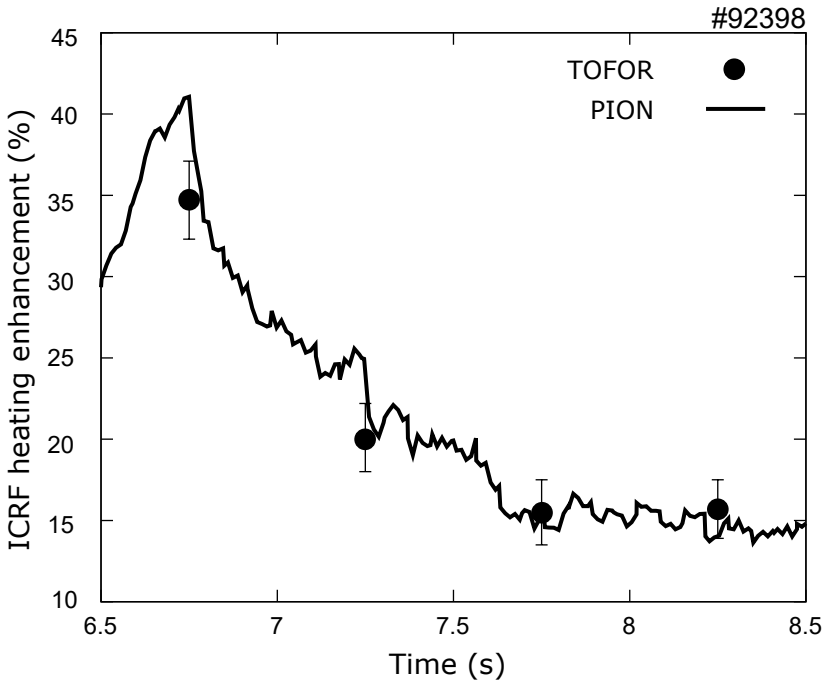

Fig. 5.11 *ICRF enhancement of neutron yield for discharge 92398. Comparison of PION (solid line) and experimental results based on TOFOR (black dots) measurements.*

harmonic damping becomes dominant during the main heating phase (figure 5.12a). The absorption profiles (figure 5.13) show a strong absorption of fundamental H for low

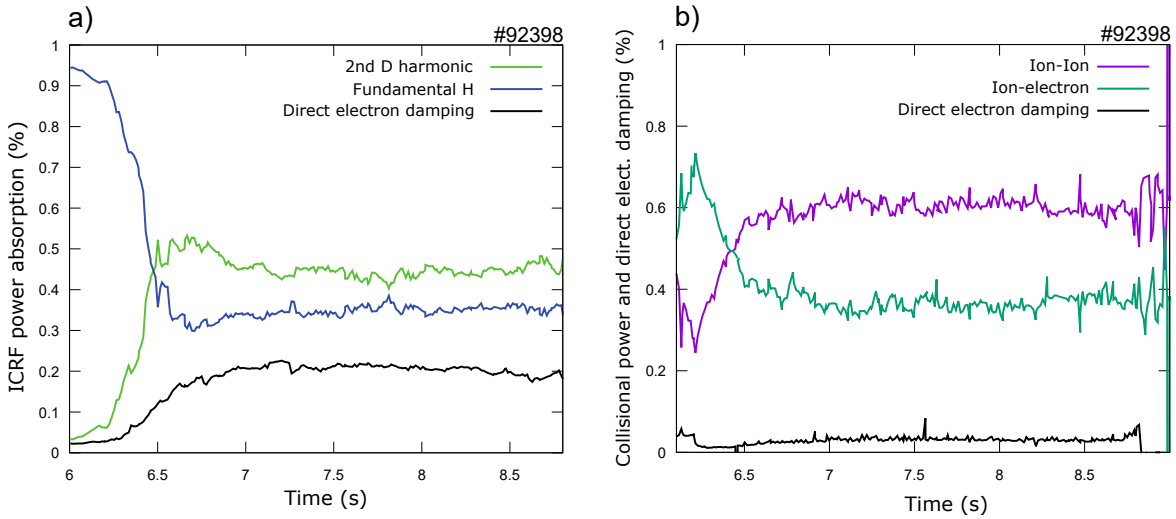

Fig. 5.12 *a) Normalised ICRF power absorption mechanisms to the input ICRF power, fundamental H, 2^{nd} D harmonic and direct electron damping. b) Normalised collisional power to the input ICRF power for discharge 92398.*

plasma temperatures while this becomes lower during the main heating phase where

D absorption becomes dominant as seen in section 5.2. Bulk ion heating is dominant throughout the whole discharge except for the low temperatures and densities that characterise the ramp-up phase (figure 5.12b), where fundamental H strongly dominates generating a fast ion population that slows-down mainly through ion-electron collisions. PION predicts an average fast ion energy of 500 keV for minority H at t = 6.25 s where fundamental H absorption peaks and 160 and 65 keV for H and D, respectively, during the main heating phase. The computed critical energies are 115 and 230 keV for H and D, respectively, during the main heating phase. Our modelling results show higher bulk ion heating than electron heating during the main heating phase from t = 6.5s onwards. While full heat transport analysis is beyond the scope of the present study, this appears consistent with the measured higher T_i than T_e. In addition, the equivalent D-T power output has been calculated and a total of 7 MW of fusion power has been obtained. A more detailed explanation on the extrapolation to D-T plasmas can be found in chapter 6.

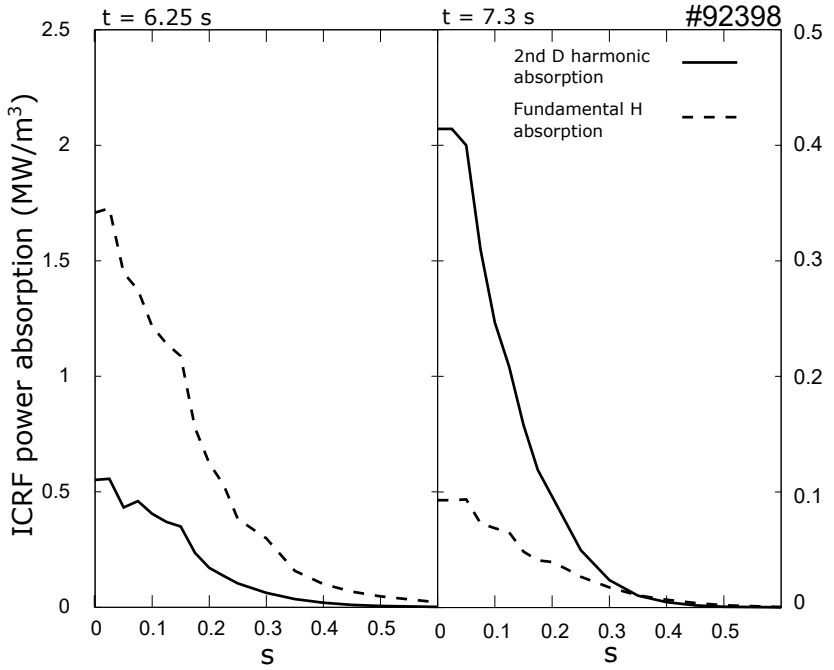

Fig. 5.13 *Absorption profile for fundamental H absorption (dashed) and 2nd D harmonic absorption (solid) at t = 6.25 s and t = 7.3 s. The right y-axis has been normalised to the average ICRF input power of 5MW.*

5.4 Conclusions

The goal of this chapter was to study how to increase the number of fusion reactions for the hybrid scenario using H minority heating in D plasmas. To do so, the hydrogen concentration was tuned to maximise the energy transferred from the wave to the deuterium population. In the case of a D plasma this has been shown to be beneficial mainly due to the D-D cross section peaking at the MeV range of energies. Thus, generating a strong tail of D ions enhances the number of fusion reactions. This effect is well reproduced by PION and supported experimentally where the experimental distribution functions of D show a stronger tail for lower H minority concentrations. In average, this approach has the potential to boost the neutron rate by 20%.

This result lead to a high-performance discharge that achieved a new fusion record of $2.7 \cdot 10^{16}$ s^{-1}. The ICRF enhancement in this case was found to be of about 15% during the steady state as it was shown to be dependent on plasma density and temperatur as both parameters increase thermal reactions. It was also found to be dependent on neutron emission from D beams, such effects effectively reduce ICRF enhancement. PION results confirmed that in order to reach high fusion yield a larger fraction of the wave energy needs to be channeled to the D population and larger ion-ion than ion-electron heating is also necessary. It was also found that a prediction to D-T is not straightforward as heating aspects change (more detail in chapter 6) and the fusion cross section peaks around 120 keV making the scheme of channeling all the wave energy to D not valid anymore. An equivalent D-T fusion power of 7 MW was found.

Chapter 6

Extrapolation of a high performing discharge

This chapter presents an exercise based on extrapolations to higher heating power and different plasma compositions. It focuses on a particular high performing hybrid discharge, 86614, which reached a record neutron rate in JET in 2014. This discharge was characterised by a two well differentiated phases, a high performance and a transition to a low performance phase dominated by strong impurity accumulation and MHD activity. The original ICRF scheme consisted of H minority in a D plasma. Not all the heating power at JET was available during these experiments and, therefore, this modelling exercise predicts the performance of this shot if the total power had been available and for an additional ICRF scheme, the ^{3}He minority. This assessment has been performed using the integrated modelling code JETTO.

The second part of the chapter studies the prediction to D-T plasmas. A high performance in a D-T plasma is the final goal in nuclear fusion and in particular for the forthcoming second D-T experimental campaign in JET (DTE2). An analysis through several parameter scans is given for ^{3}He and H minority schemes in a D-T plasma. The impact of the variation of these parameters on the physical aspects of fusion performance is studied and identified for each case. These simulations have been performed using a standalone PION version coupled to the beam deposition code PENCIL.

The results contained in this chapter have been published in Publication 1, 4, 5 and Ref. [72] (c.f. pages xxii-xxiii).

6.1 Introduction

The prediction for a D-T discharge is the last step in the analysis of the high-performance hybrid discharges, where the maximum power output and the best strategy to follow is studied. In order to model a 50%:50% D-T plasma from a D hybrid high-performance discharge, the plasma composition is modified by changing half of the bulk D by T and half of the D beams to T. The stand-alone simulations for PION take a single time point of the original discharge, in this case 86614, and evolve until a steady state solution is found.

Quasi-neutrality is maintained in all cases since the electron density is computed as $n_e = \sum_i Z_i n_i$ in both codes, PION and PENCIL. The NBI penetration is calculated by the PENCIL code under the presence of T for both beam species, D and T. The collisionality is computed in PION for all resonant species with the background plasma defined as 50%:50% D-T. The magnetic equilibrium is assumed to be as in the original discharge and, therefore, does not take into account the change in the Grad-Shafranov shift at the magnetic axis. An estimation of the shift at the magnetic axis due to the presence of T in the plasma with regards to the pure D scenario has been carried out using the Grad-Shafranov shift equation as given in [2]. The plasma energy increases by around 30-35% from pure D to D-T plasma, assuming the internal inductance to be constant, the Grad-Shafranov shift at the magnetic axis increases approximately by 2-4 cm. This is in line with the D-T prediction simulations performed in [14] where an increase of 3 cm was found. Such a small change will have a very small impact in the simulations performed in the present chapter. However, in case larger shifts occur, the resonance position would be placed further off-axis at the HFS. This could be solved by slightly tuning the toroidal field as to match the central resonance.

In this new scenario, the ICRF scheme changes as T becomes resonant together with H and D. However, as discussed in chapter 5 and showed in equation 5.3 the damping strength of 3$^{\text{rd}}$ T harmonic is negligible as compared to that of H or D. In fact, as D and T beams are injected, the 2$^{\text{nd}}$ D harmonic becomes the dominant damping mechanism, as expected. Nevertheless, while chapter 5 hinged around the idea that channeling most of the power to D was beneficial for the fusion performance, it does not necessarily apply in the D-T scenario. The reason is that fusion D-D and D-T cross sections peak at different energy regions, while D-D cross section peaks around the MeV range, D$\rightarrow$T cross section peaks around 120 keV and decreases rapidly beyond this energy. Therefore, one needs to be careful in the way energy is channeled to D as a strong high energy tail in the distribution function has the potential to decrease the number of fusion reactions. As beams are close to the optimal energy for D-T

fusion reactions to occur, most of the fusion reactions are due to beam-thermal ion interactions and thus, a lower ICRF enhancement is expected as compared to the D-D scenario.

6.2 Extrapolation to maximum available power at JET

An overview of the high performing discharge 86614 is shown in figure 6.1. This discharge consisted of 25 MW of total heating power (20 MW of NBI and 5 MW of ICRH). A minority concentration of around 2.5% of H was used. The high performance phase (7-9 s) was limited by impurity accumulation and MHD activity. The low performance phase spans from 9 s onwards. These two phases are clearly visible in figure 6.1 for the R_{NT} and T_e values.

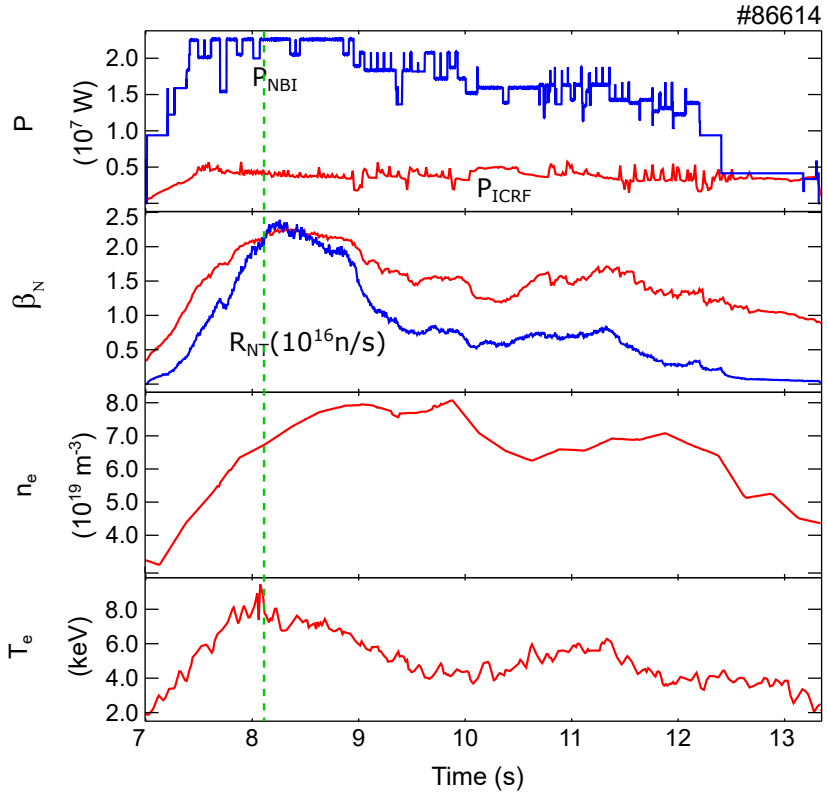

Fig. 6.1 *Overview of the high performing hybrid discharge 86614. The vertical green dashed line marks the time slice where simulations are performed for the D-T prediction.*

In order to predict the performance at the maximum available power at JET the integrated modelling code JETTO [73] has been used. The added value of using

JETTO together with PION is that it allows to compute the transport and, therefore, assess the impact of bulk ion heating on ion temperature and on the fusion reaction rate. This is necessary as in the ^{3}He minority scenario the only resonant species is ^{3}He ions for a D plasma and transport calculations become crucial to properly account for the fusion yield of D background ions.

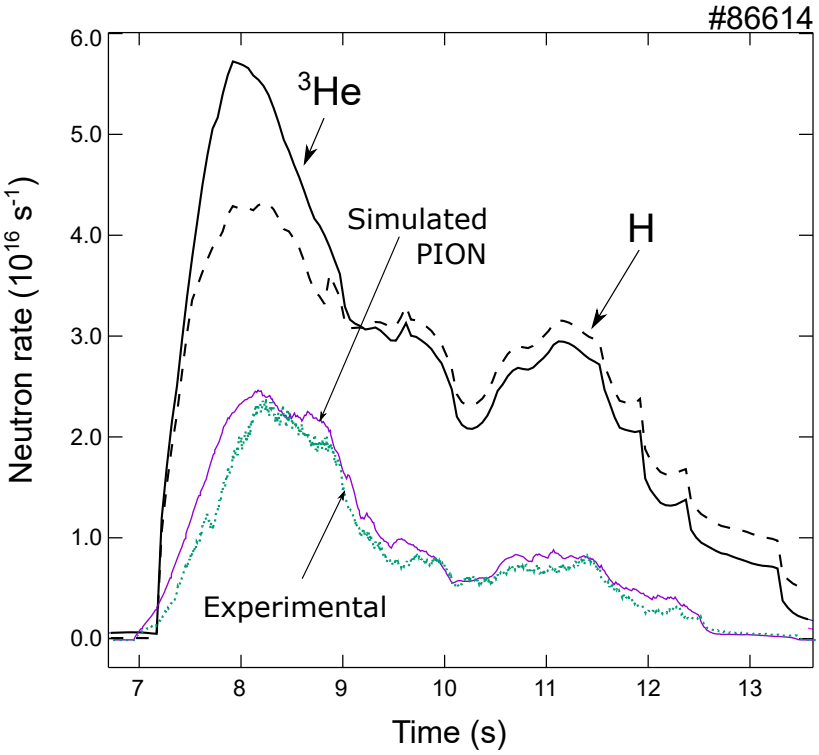

Fig. 6.2 *Experimental (dotted/green) and simulated fusion reaction rate of original experimental data with PION (solid/purple). Simulations for a power extrapolation with JETTO (34 MW NBI and 6 MW ICRH) for H minority (dashed) and ^{3}He minority for discharge 86614.*

The fusion reaction rate is shown in figure 6.2. The solid purple line is the fusion yield simulated using PION for the real experimental configuration, the green dots represent the experimental value of the neutron rate, and excellent agreement is found [74]. The black solid and dashed lines are the simulated neutron rate for the higher power using JETTO for ^{3}He and H minority scenarios. The first noticeable and remarkable feature from figure 6.2 is that by increasing the heating power by a factor of 1.48 the neutron rate increases by a factor of 2-3, further increasing the neutron rate efficiency. The non proportionality between factors is normal since typically changes in temperature, i.e. in energy, lead to changes in the value of the fusion cross section which are non linear. The second important feature is that an important difference

between both minority schemes is shown during the high performing phase while this difference diminishes in the low performance phase. The ^{3}He minority scheme reaches a higher neutron rate as compared to the H minority during the high performing phase. This result is understood with figure 6.3 that shows a higher ion temperature achieved in the ^{3}He scheme. A peak temperature of 16 keV and 12 keV is reached by ^{3}He and H minority schemes, respectively, during the high performing phase, in the low performance phase it decreases sharply at a value around 10/12 keV and 8/10 keV for ^{3}He and H, respectively. However, during the low performance phase neutron rate is stronger in the H minority scheme rather than in the ^{3}He scheme.

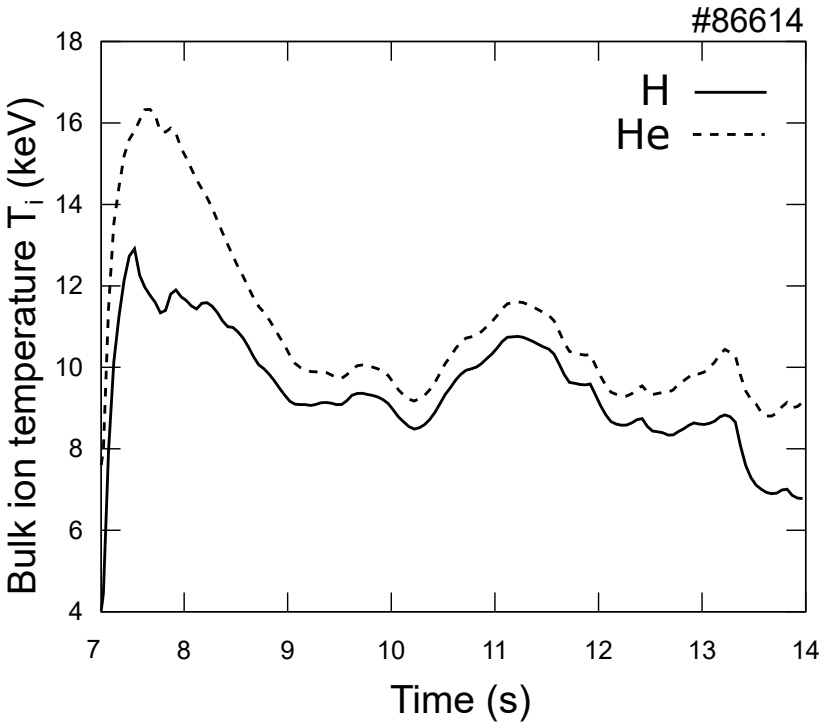

Fig. 6.3 *Simulated central ion temperature for H (solid) and ^{3}He (dashed) minority schemes for discharge 86614.*

These differences are explained by studying the collisional power and power absorption in each scenario. In figure 6.4 collisional power is shown for both minority schemes. Notice that ion-ion collisions are dominant throughout the whole discharge in the ^{3}He scheme while ion-electron collisions dominate at the beginning of the discharge (7-8 s) and ion-ion collisions become dominant beyond this point. This behaviour in the H scheme is very similar to what was found in chapter 5 and in particular for figure 5.12b. The critical energy of H is roughly one third of that from ^{3}He and the energies reached by H minority are beyond its critical energy, effectively colliding with electrons and thus

reaching a smaller ion temperature as compared to ^{3}He. In fact, the ion-ion collisional power increase in the H scheme is not only due to electron temperature peaking around 8 s but also due to the enhancement of the 2nd D harmonic heating power absorption as D beams are injected, as it was found in chapter 5. Its small atomic mass makes H very dependant on background plasma parameters such as electron temperature and density to achieve good bulk ion heating, notice the large variations of collisional power heating for H in figure 6.4. On the other hand, the ^{3}He minority scheme is typically a strong bulk ion heating scenario due to the higher atomic mass of ^{3}He ions, which tend to slow down through ion-ion collisions. Ion-ion collisions stay dominant at around 60-70% during the whole discharge. As has been shown in figure 6.2 this has a strong impact in enhancing the fusion neutron rate. Nevertheless, notice that during the low performance phase the H minority scheme performs better although bulk ion heating and ion temperature are lower.

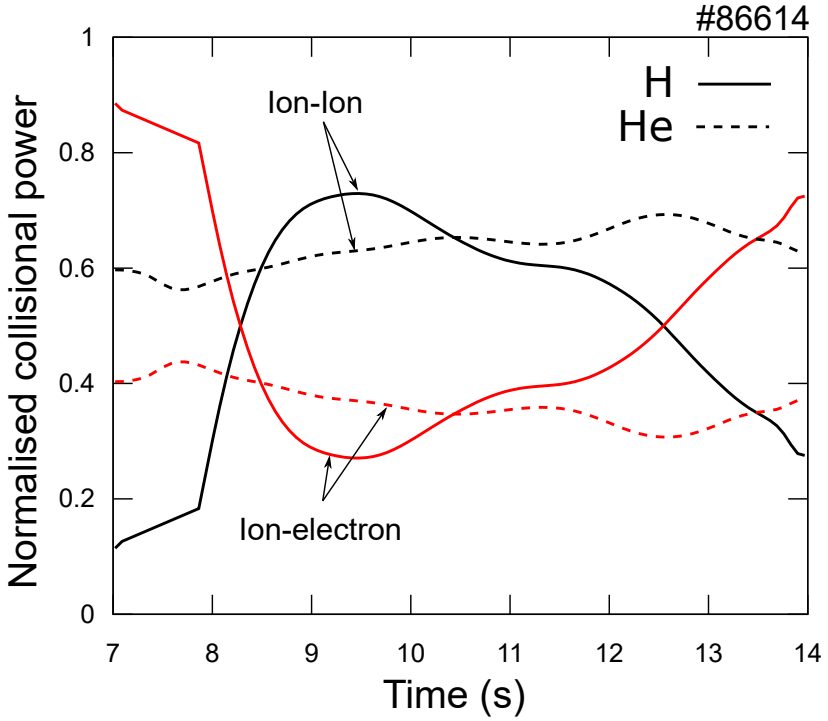

Fig. 6.4 *Normalised ICRF collisional power (6MW) for ion-ion collisions (black) and ion-electron collisions (red) for H minority (solid) and ^{3}He minority (dashed) for discharge 86614.*

Figure 6.5 shows the power absorption for the different damping mechanisms involved in each scenario, fundamental heating, 2nd D harmonic heating (H minority case) and direct electron damping. For the ^{3}He minority scheme, ^{3}He ions damping strength is dominant with 70-85% of total power absorption, lowering around 8-9 s

when the plasma density and electron temperature peaks (figure 6.1), hence maximising direct electron damping. For the H minority scheme, fundamental H absorption is the dominant damping mechanism with 65-80% of total power absorption while 2nd D harmonic absorption increases up to 25%. Around 9 s and beyond the 2nd D harmonic absorption stays roughly constant around 25% and it is the reason why in this low performance phase the H minority scheme delivers more neutrons than the ^{3}He scheme. Not only does the ion temperature gap between both schemes diminish (figure 6.3) but also D damping is maximised further increasing the fusion yield for D-D reactions. The ^{3}He scheme relies only on bulk ion heating for high fusion performance in a D plasma and, therefore, only thermal reactions are possible under these conditions.

It is important to mention that heating data shown in figures 6.4 and 6.5 refer exclusively to ICRF heating. Although 34 MW of NBI were used to carry out these simulations, the NBI collisional power is almost identical for both minority schemes which brings little to the present discussion.

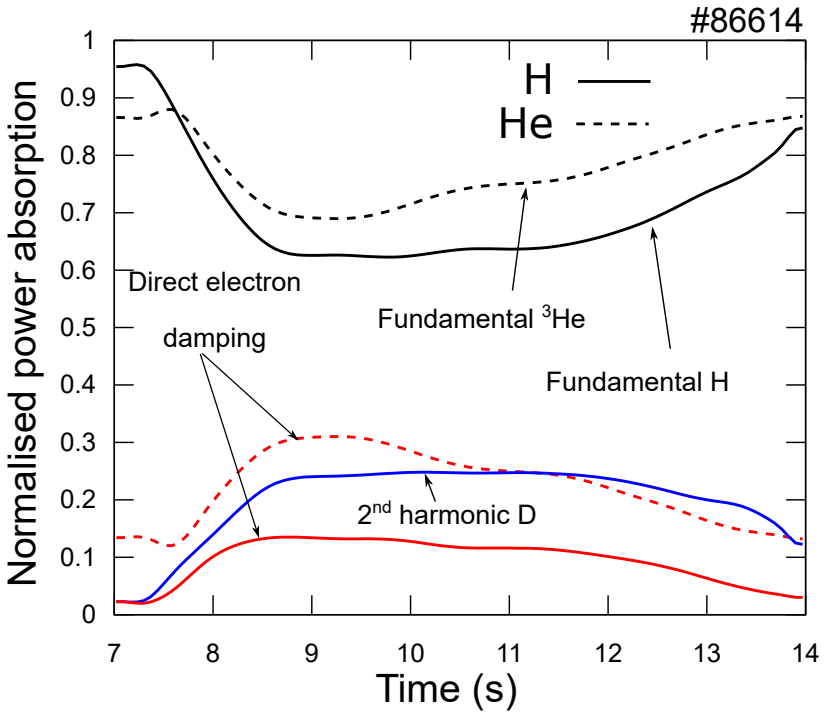

Fig. 6.5 *Normalised ICRF power absorption (fundamental/black and harmonic/blue) and direct electron absorption (red) for H minority (solid) and ^{3}He minority (dashed) for discharge 86614.*

6.2.1 Combined NBI + ICRF heating in JET D-T plasmas

Bulk ion heating and ICRF fusion enhancement are relevant quantities in order to evaluate D-T plasmas. An increased neutron rate should be obtained by maximising both. The following discussion shows the results obtained with coupled PENCIL and PION and studies the dependence of bulk ion heating and ICRF fusion enhancement under a scan on key plasma parameters. A 50%-50% D-T fuel ion mixture is considered under a scan in plasma temperature and density of the hybrid discharge 86614 ($n_e = 6.2 \cdot 10^{19}$ m^{-3}, $T_e = 9$ keV). The NBI source rate is shown in figure 6.6 for the different plasma densities considered at $T_e = 9$keV. Ion and electron temperatures are assumed to be equal. The toroidal magnetic field is set to $B_T = 3.25$ T and the plasma current to $I_p = 2.7$ MA. A total heating power of 40 MW has been simulated consisting of 34 MW of NBI power (17 MW of D beams and 17 MW of T beams) and 6 MW of ICRF power. In several simulations the ICRF power has been set to zero for comparison purposes. Regarding the ICRF scheme, a comparison between H and ^{3}He as minority species has been performed while the simulated antenna frequency has been set for central heating for all the cases under consideration. The resonant ion absorption

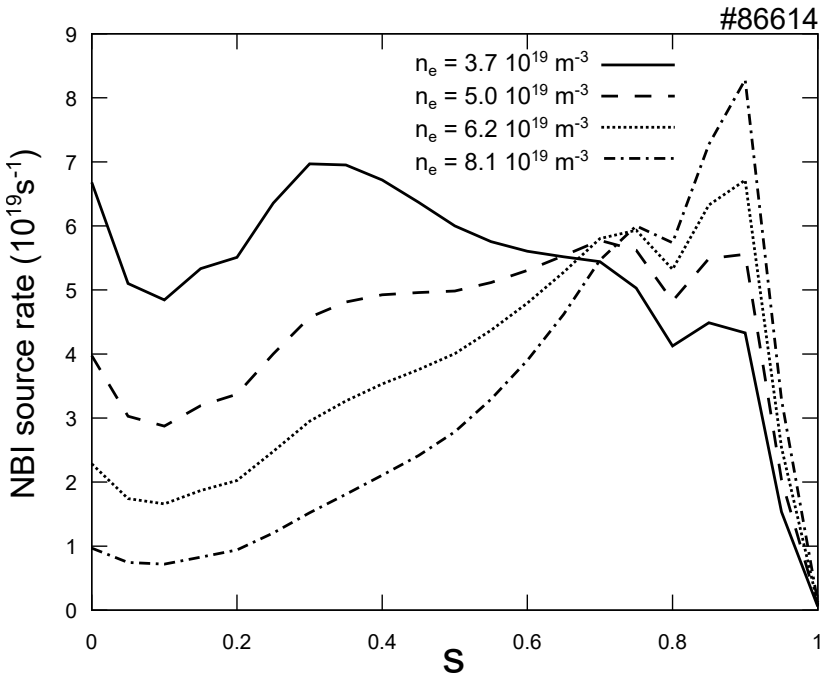

Fig. 6.6 *NBI source rate for $T_e = 9keV$ for different plasma densities.*

strength for both minority scenarios ranges from 63% to 87% and 73% to 90% for H and ^{3}He minority scenarios, respectively (figures 6.7 and 6.8). Minority concentrations for H and ^{3}He are maintained constant at 5% over D and T densities, $\frac{n_H}{n_D+n_T}$ and

$\frac{n_{^3He}}{n_D+n_T}$, respectively. PION predicts a dependency of the power absorption on both the plasma density and the plasma temperature. For lower plasma temperatures and densities the power absorption on ions is higher while it decreases for higher values of plasma temperature and density where direct electron damping is stronger as it is $\propto T_e n_e$. However, ion absorption is dominant over direct electron damping for the whole range under consideration.

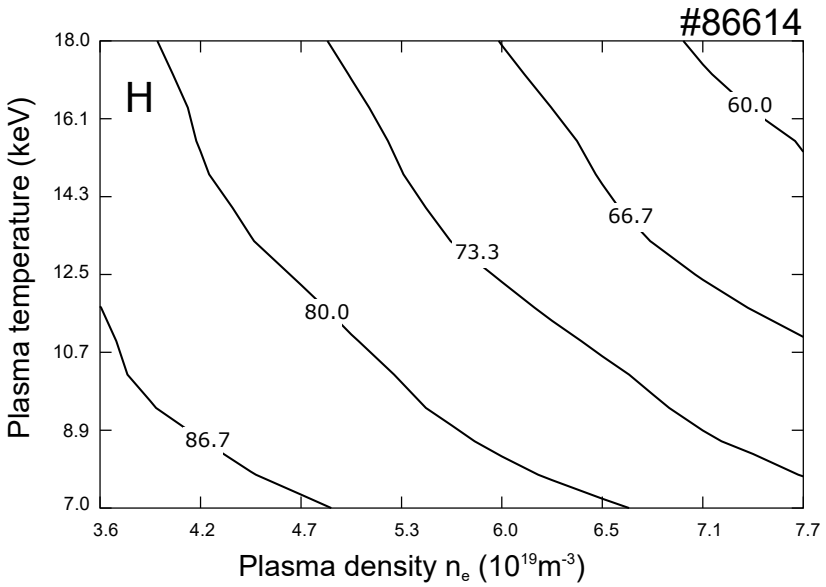

Fig. 6.7 *Contour lines of normalised power absorption of resonant ions to total RF input power (6MW) in % for a minority concentration of 5% of H minority.*

Bulk ion heating is shown in figures 6.9 and 6.10. Although D and T beams are used for both minority scenarios, i.e. H and ^{3}He, only resonant species are shown, therefore, only T beams (17 MW and $\sim$ 95 keV) are shown in the ^{3}He minority case and only D beams (17 MW and $\sim$105 keV) in the H minority case as they are resonant through the 2$^{\text{nd}}$ harmonic resonance. Tritium beams are resonant in the H minority scenario but the 3$^{\text{rd}}$ T harmonic resonance absorption strength is negligible in front of the 2$^{\text{nd}}$ D harmonic and H fundamental absorption strength as predicted by PION under the conditions of this scenario.

For all the ranges under consideration of the pure NBI simulated scenario, between 65-90% of the D NBI power and 82-100% of the T NBI power is transferred to ions, this difference lies in the higher energy of D beams and a higher critical energy of T beams as $E_{crit} \propto A$ (see equation 2.30). The simulations with NBI+ICRF show a different trend and the differences between both minority scenarios grow. As the critical energy increases with T_e the collision power from resonant ions to thermal ions depend mainly

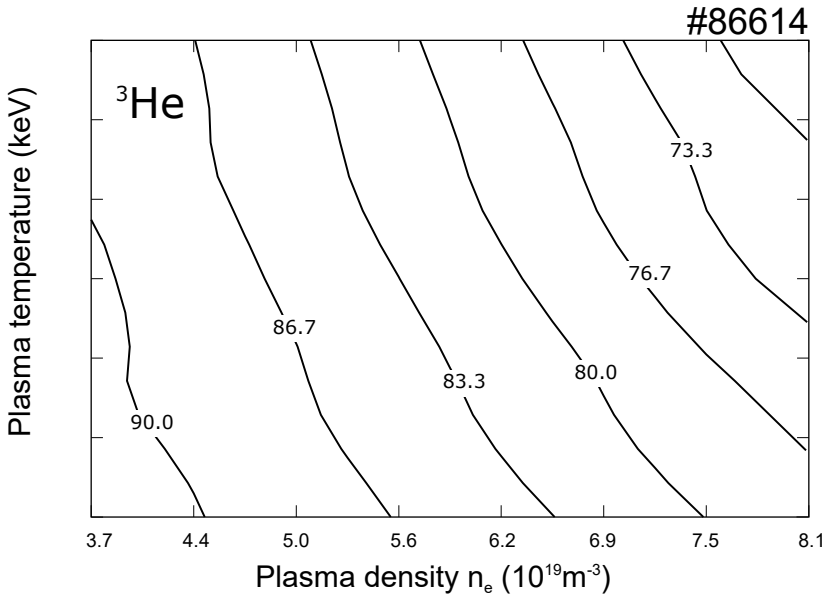

Fig. 6.8 *Contour lines of normalised power absorption of resonant ions to total RF input power (6MW) in % for a minority concentration of 5% of ^{3}He minority.*

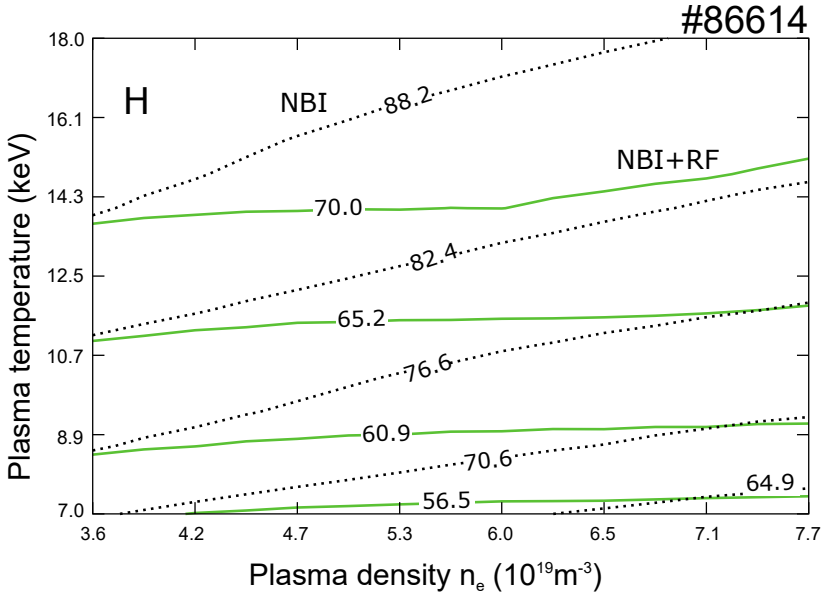

Fig. 6.9 *Contour lines of normalised collisional power from resonant ions to thermal ions for NBI and NBI+RF to total RF input power (6MW) and resonant beam power (17MW) in % for a minority concentration of 5% of H minority.*

on the plasma temperature. However, as compared to the simulated pure NBI scenario, the NBI+RF scenario shows an increase of bulk ion heating with plasma density. The reason why this occurs is that the average energy of fast ions tends to decrease and the direct electron damping becomes relatively stronger for increasing plasma densities.

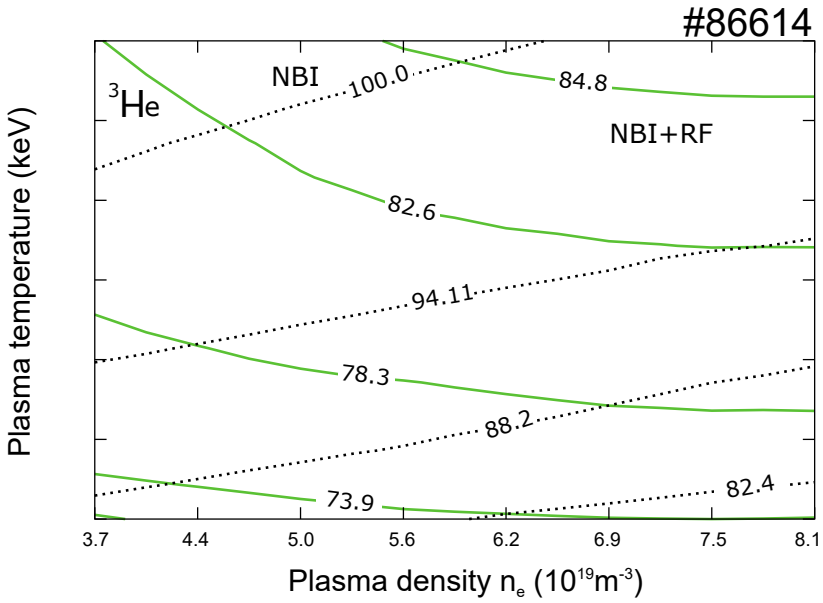

Fig. 6.10 *Contour lines of normalised collisional power from resonant ions to thermal ions for NBI and NBI+RF to total RF input power (6MW) and resonant beam power (17MW) in % for a minority concentration of 5% of ^{3}H minority.*

Both effects tend to increase the proportion of fast ion energy transferred to ions by lowering the average fast ion energy (see figure 5.1).

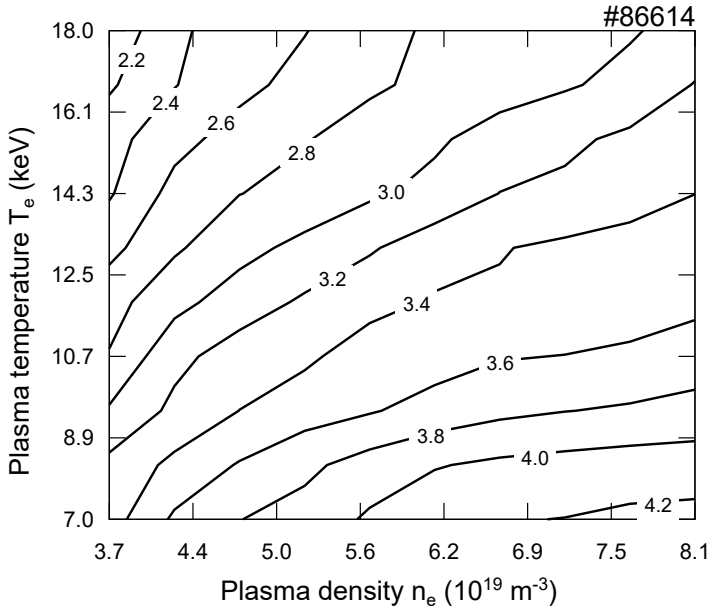

Fig. 6.11 *Contour lines of the ^{3}He-H scenarios difference in collisional power from resonant ions to thermal ions for a NBI+RF input power of 17+6MW and a minority concentration of 5%.*

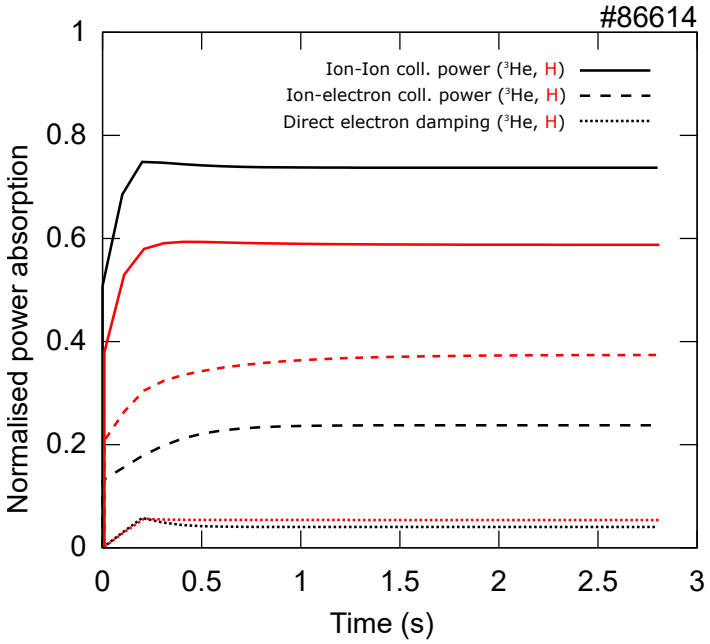

Fig. 6.12 *Bulk ion heating and direct electron damping at* $n_e = 6.9 \cdot 10^{19}$ *and* $T_e = 9keV$.

Regarding the differences between both minority scenarios, the ^{3}He minority scenario shows a 10-20% higher bulk ion heating, mainly due to a higher critical energy of ^{3}He as compared to H and the lower direct electron damping in the ^{3}He minority scenario. In figure 6.11 the difference in bulk ion heating between ^{3}He and H is shown, this difference is greater for lower plasma temperatures where the critical energy is substantially reduced and for higher plasma densities where direct electron damping becomes more relevant in the H scenario (figure 6.7). Moreover, ion-electron collisions are more relevant in the H minority scheme as compared to the ^{3}He scheme as a result of lower critical energy, figure 6.12 shows this feature for the original plasma temperature and density of the discharge where small differences in direct electron damping are found. A scan in the minority concentration at $T_e = 9$ keV and $n_e = 6 \cdot 10^{19}$ m^{-3} is

Minority	1%	3%	5%	7%
H	13.5	13.7	13.9	14.1
^{3}He	16.1	17.0	17.7	18.0

Table 6.1 Bulk ion heating in MW for a scan in the minority concentration for $P_{NBI} = 17$ MW and $P_{ICRF} = 6$ MW.

presented in table 6.1. Bulk ion heating increases with the minority concentration for both cases as the average fast ion energy decreases. For higher minority concentrations

the absorption tends to become weaker for fundamental heating as the polarization of the wave changes due to high minority concentration in the plasma.

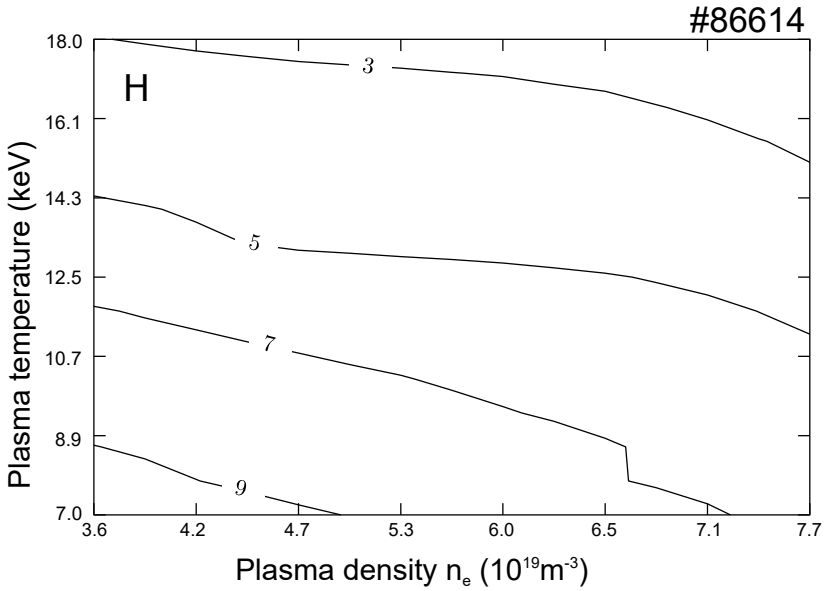

Fig. 6.13 *Contour lines of the ICRF fusion enhancement of D+T reaction rate in % of the total* $\frac{R_{NT}(NBI+RF)-R_{NT}(NBI)}{R_{NT}(NBI+RF)}$ *for 5% of H minority* ^{3}*He minority.*

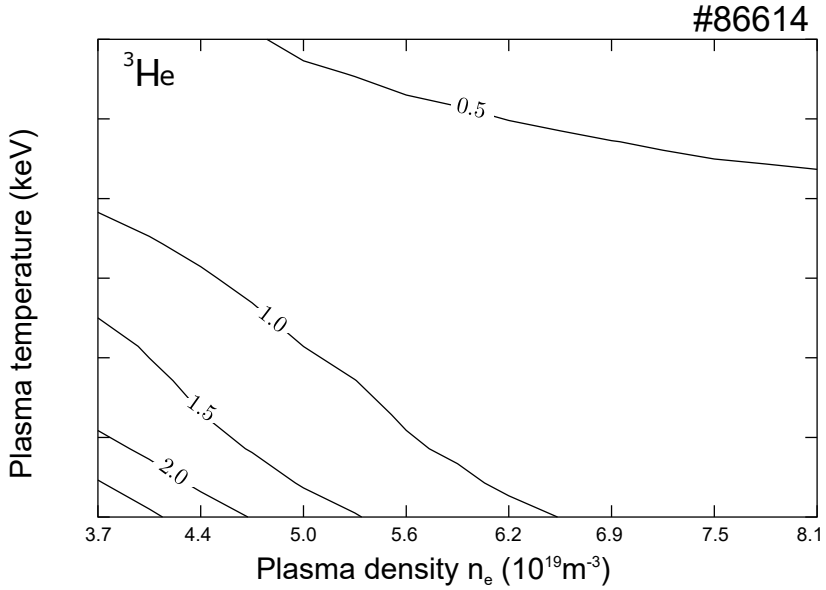

Fig. 6.14 *Contour lines of the ICRF fusion enhancement of D+T reaction rate in % of the total* $\frac{R_{NT}(NBI+RF)-R_{NT}(NBI)}{R_{NT}(NBI+RF)}$ *for 5% of* ^{3}*He minority.*

The motivation for modelling the ICRF fusion enhancement of the D-T scenario (figures 6.13 and 6.14) comes from the fact that, in principle, ICRF heating can

accelerate deuterons and tritons beyond the optimal D-T fusion reaction energy (∼120 keV for fast D and ∼160 keV for fast T), which could result in a lower fusion yield. However, figures 6.13 and 6.14 show that this is not the case for the parameter range under consideration as the ICRF enhancement is positive in both minority scenarios. The ^{3}He scenario shows a lower ICRF enhancement of the D-T fusion reaction rate as the T damping strength is roughly 10% of the total D damping strength for the H minority scenario. Nevertheless, the ICRF fusion enhancement behaves in a similar way for both minority scenarios, it is lowest at regions where thermal fusion reactivity increases, i.e. regions of higher plasma density and temperature. The ICRF enhancement ranges from 2-9% for H minority scenario and 0.5-2% for ^{3}He minority scenario.

6.3 Conclusions

This chapter is a modelling effort to predict plasma performance by extrapolating to conditions that could be achievable in D-T plasmas. These type of simulations are interesting as they give an idea of what to expect in real experiments under similar conditions. The extrapolations were 1) higher power and 2) D-T plasma conditions. Moreover, an additional ICRF scheme (^{3}He minority) has been modelled which is of special importance for the future D-T campaign at JET. The record hybrid discharge 86614 has been used as a reference and experimental data has been modified for the predictive exercise.

The first assessment tackles a prediction for higher heating power conditions. The power has been increased (by a factor of 1.48) to the maximum available power in JET, 40 MW, 34 MW of NBI and 6 MW of ICRH. These simulations have been performed using JETTO and PION and show an increase of the neutron rate production by a factor of 2-3. This was explained by the rising in the bulk temperature during the high-performing phase to 16 keV and 12 keV for the ^{3}He and H minority scenarios, respectively. This difference in temperature has a direct impact in the thermal fusion rate. The higher ^{3}He minority scheme temperature is the result of a higher bulk ion heating which stays around 60-70% during the whole discharge. The smaller critical energy of H as compared to ^{3}He makes H very dependent on background plasma conditions such as electron temperature and density which forces bulk ion heating to stay low during the high-performing phase. However, as electron temperature increases and D beams are injected bulk ion heating reaches 70% of the total ICRF power. During the low-performing phase, D absorption becomes more relevant, up to 25%

of the total ICRF power, effectively increasing the fusion rate which becomes greater than in the ^{3}He scenario.

The second analysis hinges around a prediction for a D-T plasma composition at maximum available power. The focus is given to a scan in two plasma parameters, plasma temperature and density. The results allow to have a comprehensive understanding of bulk ion heating in a wide range of plasma conditions. Both minority schemes, H and ^{3}He show good ion power absorption, 60-87% and 73-90%, respectively. Power absorption has a strong dependence on both parameters, plasma density and temperature as both tend to increase direct electron damping while reducing ion absorption. Bulk ion heating behaviour is more complex, in general terms, ^{3}He offers higher energy transfer to background ions ranging from 10 to 20% of the total input power for resonant ions. This difference is reduced for higher temperatures and lower densities as the H critical energy increases and the direct electron damping becomes reduced.

Chapter 7

JET T and D-T plasmas

A tritium (T) campaign is planned in preparation for the deuterium-tritium (D-T) campaign at the Joint European Torus (JET). These experiments will be the first experiments involving T with the ITER-like plasma-wall facing components materials. They will give a unique opportunity to test one of the most promising ion cyclotron resonance frequency (ICRF) heating schemes for ITER plasmas: the 2nd tritium (T) harmonic resonance ($\omega = 2\omega_T$). This chapter provides two key contributions related to modelling of the performance of this scheme at JET. First, we assess the heating performance of the 2nd T harmonic resonance and, second, we model different ICRF schemes for the T campaign in support for the D-T campaign, i.e., identify differences and similarities from the heating point of view between T and D-T plasmas in order to predict the performance of $\omega = 2\omega_T$ in the D-T scenario. In our modelling we use a selected hybrid record discharge as reference, i.e., using its experimental profiles. We consider two ICRF schemes (6 MW), i.e. $\omega = \omega_{^3He} = 2\omega_T$ (no ^{3}He), with a central resonance and three NBI power outputs (15, 25 and 35 MW) in two plasma compositions (100% T and 50%:50% D-T). Note that isotope effects are not taken into account in these simulations. For this study, the ICRF and NBI heating are modelled with the ICRF code PION and the beam code PENCIL which take into account the ICRF+NBI synergy.

The analysis of the T velocity distribution function shows that a stronger tail is formed in plasmas with lower tritium density. This fact has an important impact on the slowing-down process of fast tritons with the background species. The T plasma shows a higher and more peaked ion-ion collisional power density at the plasma centre as compared to D-T plasma. In the T plasma, ICRF heating drives fast tritons at the plasma centre with an average energy substantially lower than in the other case. On the other hand, the use of ^{3}He as a minority makes the fast ion T energy considerably

lower due to strong ^{3}He absorption. Fast ion average energies reached at the plasma centre are similar in all species mixture cases. As a result, there is a strong heating similarity between T and D-T. However, it is crucial to study the generation of a strong T tail as a result of particle-wave interaction which is not possible under this scheme and needs to be studied in plasmas without ^{3}He in preparation of JET D-T campaign and ITER. Therefore, both schemes ($\omega = \omega_{^3He} = 2\omega_T$ and $\omega = 2\omega_T$) need to be tested.

The results shown in this chapter have been published in Publication 6 (c.f. pages xxii-xxiii).

7.1 Introduction

Both flagship scenarios at the Joint European Torus (JET), baseline and hybrid, have made considerable progress in terms of plasma performance during the deuterium (D) campaign performed in 2015-2016. Control of impurity accumulation and neutron rate production have been improved and studied in detail [19, 22, 45, 66, 75–78]. Presently, in preparation for the 2$^{\text{nd}}$ deuterium-tritium (D-T) campaign (DTE2) at JET, a D and a T campaign will be carried out. Several physical aspects will be assessed in the process such as the isotope effect and the heating schemes performance.

In this study, the focus is given to the heating performance of two ICRF schemes, the pure 2$^{\text{nd}}$ T harmonic heating ($\omega = 2\omega_T$) and the ^{3}He fundamental heating ($\omega = \omega_{^3He} = 2\omega_T$). An assessment of the heating differences arising from different plasma composition (T and D-T) is also carried out. The relevant ion cyclotron resonance frequency (ICRF) heating scheme is the 2$^{\text{nd}}$ harmonic T resonance which is one of the most promising schemes for the activated phase of ITER. We use the ICRF code PION [41] and the neutral beam injection (NBI) code PENCIL [79] which take into account the ICRF+NBI synergy. The spatial damping decrements of the ^{3}He fundamental and the 2$^{\text{nd}}$ T harmonic heating scheme as given in [67] are,

$$2\eta = \frac{\pi}{c}\omega_{pM}\frac{n_m}{n_M}R \tag{7.1a}$$

$$2\eta = \frac{\pi}{2}\frac{\omega_{pi}}{c}\beta_i R, \tag{7.1b}$$

respectively. Here, the single-pass absorption coefficient is defined as $A = 1 - e^{-2\eta}$, the subscripts m and M stand for minority and majority species, respectively, R is the major radius, c the speed of light in vacuum, ω_{pi} the ion plasma frequency, β_i the ion beta and n the ion density. Therefore, it is expected that the higher the density or the ion beta of the resonant tritons, the larger the ion power absorption of

2^{nd} T harmonic heating. However, notice that these formulas assume a Maxwellian distribution of resonant ions which is not the case considered here, where strong RF heating is occurring. Thereofre, the damping decrement due to fast ions is also taken into account in this analysis as explained in [67]. On this basis, several simulations have been performed to assess the 2^{nd} T harmonic heating in a T and a D-T plasma for three different NBI heating powers (P_{NBI}). Furthermore, resonant ions concentration plays a key role on the energy of fast ions and, therefore, in their velocity distribution function. Typically, higher concentrations lead to weaker high energy tails which has a direct impact on the thermalisation process of resonant ions (electron or ion collisions) depending on the so-called critical energy (equation 2.30).

7.2 Scenario parameters

A D hybrid high-performance discharge (#92398) has been taken as a starting point. Tritium and ^{3}He are the only resonant species in these simulations. The original plasma composition has been replaced by that of the two scenarios considered, 100% T and 50%D-50%T. The total density and temperatures (ion and electron) are the same as that for the reference D plasma in all cases under consideration. The antenna frequency is tuned for a central resonance. In table 7.1 the main parameters are shown.

	B_T	I_p	Z_{eff}	P_{ICRF}	f	P_{NBI}	E_{NBI}
92398	3.25 T	2.7 MA	1.7	6 MW	33.0 MHz	15, 25, 35 MW	118 keV

Table 7.1 Main modelling parameters for discharge 92398.

7.3 2^{nd} T harmonic and ^{3}He minority schemes in T and D-T

In this section both heating schemes are analysed, i.e., the pure 2^{nd} T harmonic and ^{3}He minority. The volume integrated power absorption of resonant ions in T and D-T is expected to be different. The modelling shows that ion power absorption is dominant in all cases (figure 7.1). However, for the pure 2^{nd} T harmonic scheme, ion absorption is greater in the T case as compared to the D-T scenario (figure 7.1a) as higher T density and energy are qualitatively beneficial for ion heating, in agreement with equation (7.1b). In T, the ion power absorption remains constant at 82% of the wave power regardless of P_{NBI} as the fast ion spatial decrements are similar,

$\eta_{f15} \sim \eta_{f25} \sim \eta_{f35}$, where the subscripts 15, 25 and 35 refer to P_{NBI}. In D-T, tritium absorption scales with P_{NBI} following equation (7.1b), where the ratio of the single-pass absorption coefficients computed for different P_{NBI} is $A_{35}/A_{15} = 1.08$ and the ratio of the total ion power absorption computed by PION is $P_{35}/P_{15} = 1.11$. In particular, for 15 MW of NBI power, ion absorption accounts for 67% of the total ICRF power.

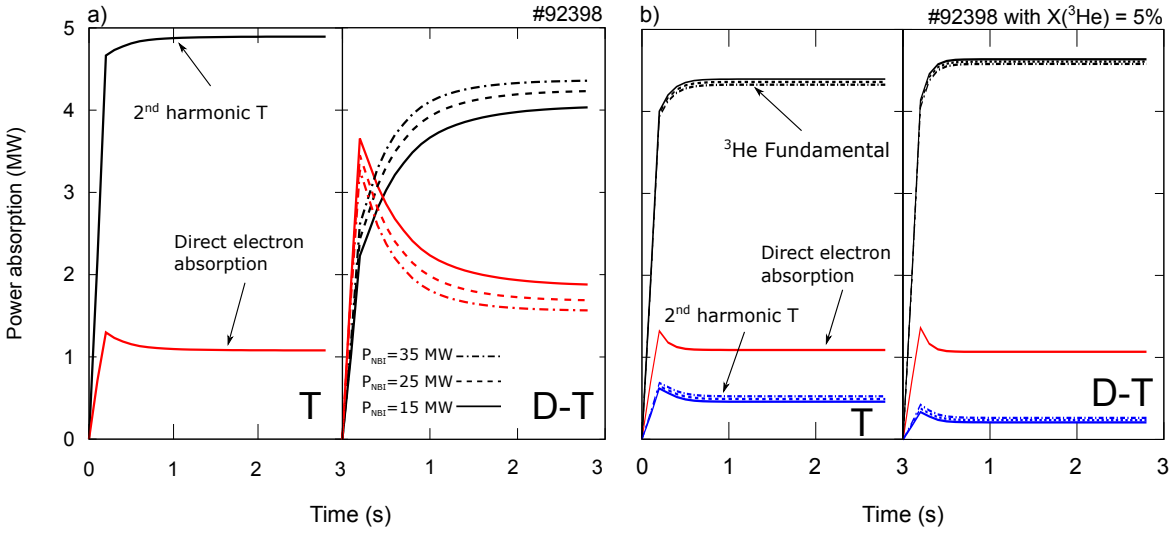

Fig. 7.1 *a) and b) volume integrated power absorptions for the pure 2nd T harmonic scenario and 3He minority, respectively, for 2nd T harmonic, 3He fundamental and direct electron damping for three different P_{NBI}, 15 MW (solid), 25 MW (dashed) and 35 MW (dash-dotted) for T and D-T scenarios for discharge 92398.*

For the ^{3}He minority scheme, the fundamental resonance is dominant over the 2nd T harmonic heating (figure 7.1b). Notice that the plasma composition (T and D-T) and P_{NBI} variations have a small impact in the power absorption competition as $\eta_{^3He} \sim 10\eta_T$ which makes ^{3}He a very strong absorber. PION predicts a total of 80% ion absorption under these conditions.

Central deposition is obtained in all cases (figure 7.2). Ion absorption is dominant while direct electron heating is larger in D-T (figure 7.2a) as the lower T density in the plasma reduces notably the value of equation 7.1b. More peaked profile is obtained for D-T as a result of larger average fast ion energies reached as described by the local power absorption equation 5.2. For the ^{3}He case very similar profiles are obtained as ^{3}He fundamental absorption is similar in T and D-T (figure 7.2b).

Another important aspect when studying plasma heating is the bulk ion heating or, in other words, the fast ion collisional power to background ions. Bulk ion heating has a large impact on thermal-thermal reactions. Typically, high-performing shots rely on increasing the collisional energy to ions which leads to higher ion thermal temperature

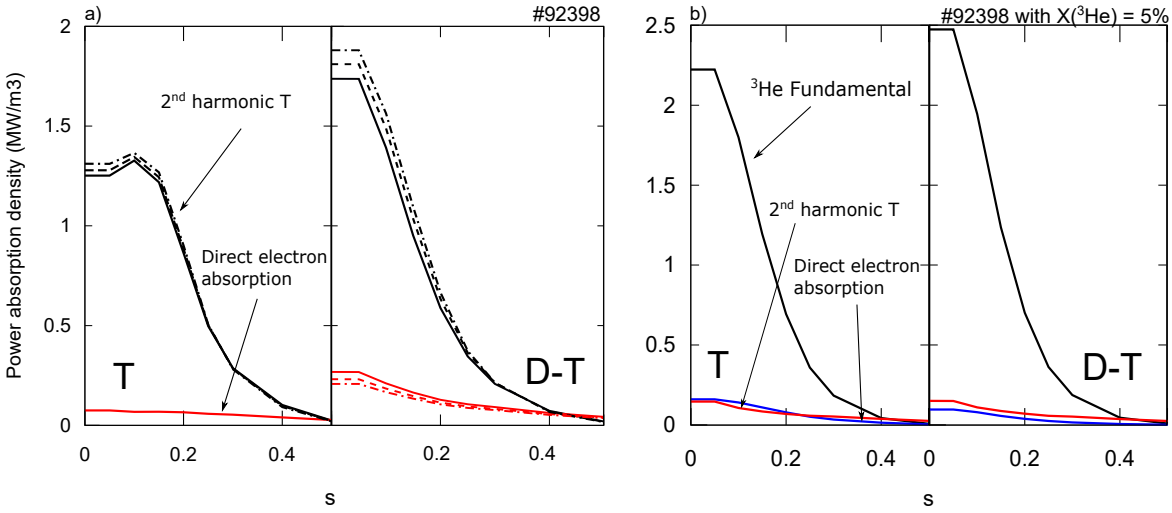

Fig. 7.2 *a) and b) power absorption profiles for the pure 2nd T harmonic scenario and 3He minority, respectively, for 2nd T harmonic, 3He fundamental and direct electron damping for three different P_{NBI}, 15 MW (solid), 25 MW (dashed) and 35 MW (dash-dotted) for T and D-T scenarios for discharge 92398.*

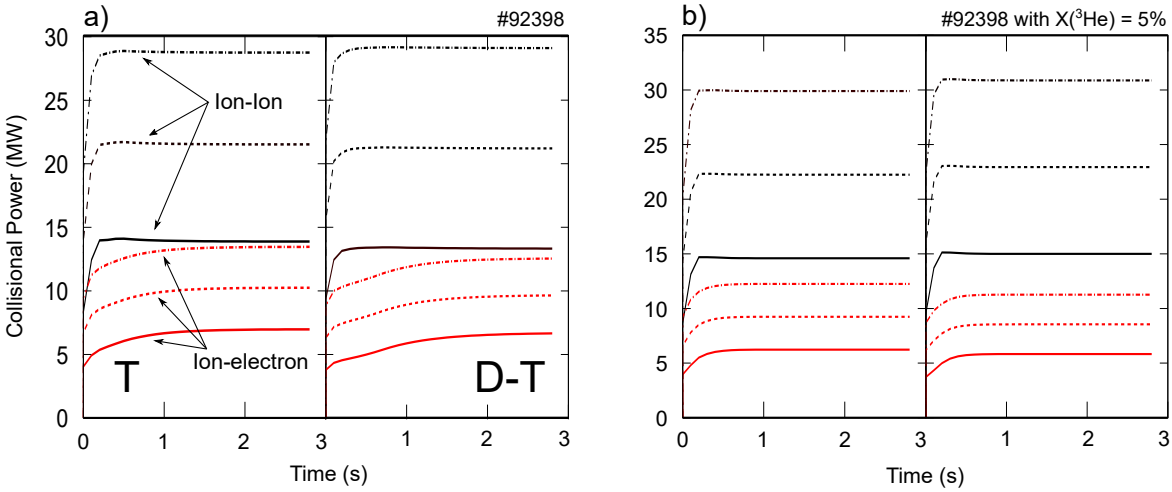

Fig. 7.3 *a) and b) Volume integrated collisional power for the pure 2nd T harmonic scenario and 3He minority, respectively. Ion-ion collisions (black) and ion-electron collisions (red) for three different P_{NBI}, 15 MW (solid), 25 MW (dashed) and 35 MW (dash-dotted) for T and D-T scenarios for discharge 92398.*

and, therefore, higher neutron yield [24, 45], although other mechanisms such as ICRH and NBI synergy also play a role in enhancing the neutron yield [75, 77, 80]. In all cases dominant bulk ion heating is obtained (figure 7.3), in general 65% of the total heating power is transferred to ions with slightly higher values in the pure T case (figure 7.3a). In the 3He case ion-ion collisions are slightly more dominant than in the

pure 2nd T harmonic scenario and almost no difference between D and D-T is seen (figure 7.3b).

In general, figure 7.3 shows that almost no differences should be expected between these scenarios in terms of fast ions slowing down with background species and therefore in bulk temperature. However, ion collisional power differs notably at the ICRF resonance location (figure 7.5a). While collisional electron heating is similar, ion collisional heating is substantially higher at the resonance position in the pure T scenario as shown in figure 7.5a. The difference in T density between the two scenarios, T and D-T, has a strong impact on the velocity distribution function of resonant tritons (figure 7.4). Bulk ion heating is lower in the D-T scenario as a result of the lower T density which drives a stronger energetic tail in the range of several MeV as compared to the T scenario. Thus, a smaller concentration of fast ions around the critical energy (330 keV) is found (figure 7.5b) which explains the lower central bulk ion heating. It is important to mention that this central difference in ion collisional heating arises from the ICRF accelerated resonant ions. Figure 7.6 shows that although similar ion-electron heating is obtained, central bulk ion heating contribution from ICRF is considerably higher in T than in D-T as a result of different fast tritons energy in each scenario.

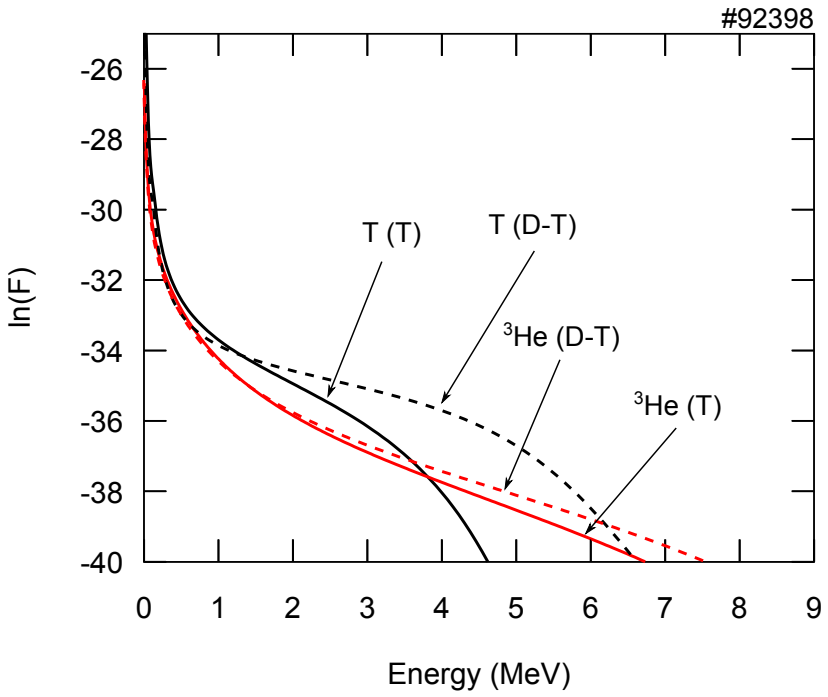

Fig. 7.4 *Velocity distribution functions of resonant tritons (black) for the pure 2nd T harmonic scheme and of resonant ^{3}He ions (red) for T (solid) and D-T (dashed) scenarios for discharge 92398.*

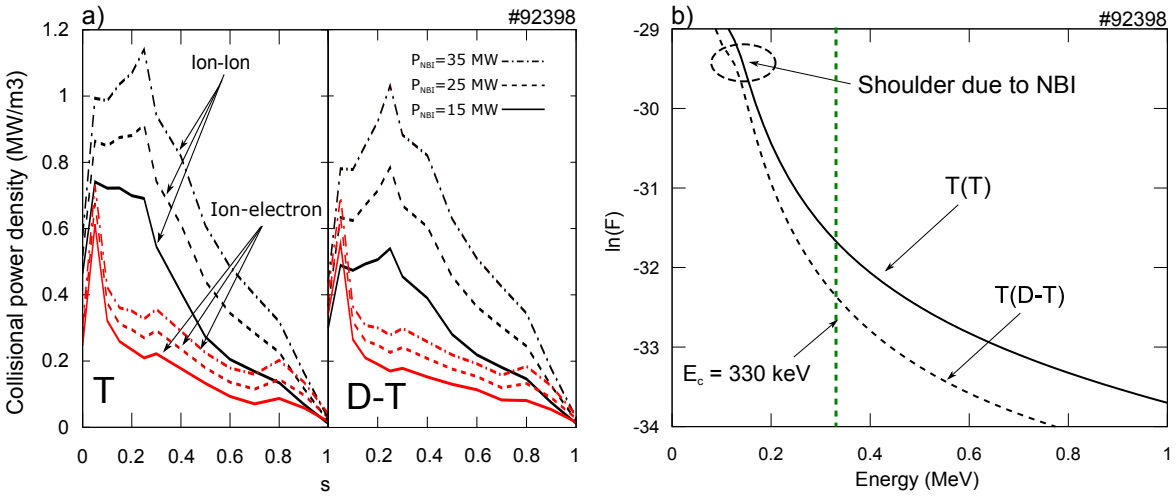

Fig. 7.5 *a) Profile of collisional power for ion-ion collisions (black) and ion-electron collisions (red) for three different P_{NBI}, 15 MW (solid), 25 MW (dashed) and 35 MW (dash-dotted) for T and D-T scenarios for discharge 92398. b) Detail of the velocity distribution function of tritons around the critical energy for T (solid) and D-T (dashed) scenarios for discharge 92398.*

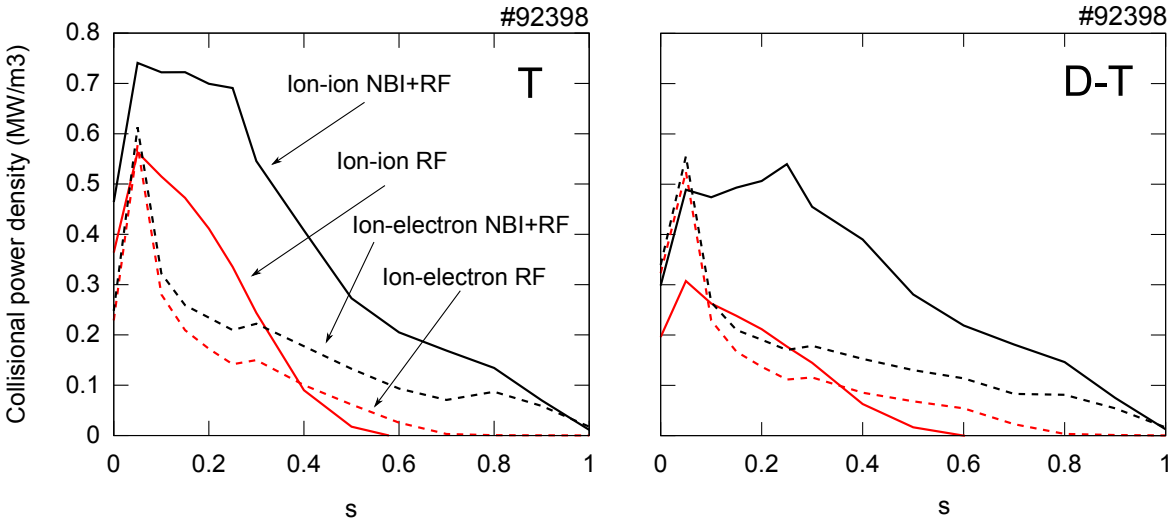

Fig. 7.6 *Ion-ion (black-solid) and ion-electron (black-dotted) collisional powers for 15 MW of NBI and ICRF heating. Ion-ion (red-solid) and ion-electron (red-dotted) collisional powers with ICRF heating and no NBI for T and D-T scenarios for discharge 92398.*

Very similar bulk ion heating is expected for both T and D-T scenarios for the ^{3}He scheme (figure 7.7a). The strong absorption of resonant ^{3}He ions makes the velocity distribution function to be virtually equivalent (figure 7.7b). Notice that fast tritons energy is kept below the critical energy for the range considered here. As opposed to

the pure 2nd T harmonic scheme, for the ^{3}He minority scheme dominant central bulk ion heating is expected regardless of P_{NBI} (15-35 MW). These results suggest that higher central ion temperature should be expected in the ^{3}He scenario as opposed to the pure 2nd T harmonic and, for the 2nd T harmonic higher ion temperature in T than in D-T. This conclusion has been supported by recent studies carried out with heating codes coupled with transport solvers, therefore, the prediction from T to D-T is not straightforward and a difference in bulk ion temperature plays an important role in the neutron yield that needs to be assessed carefully.

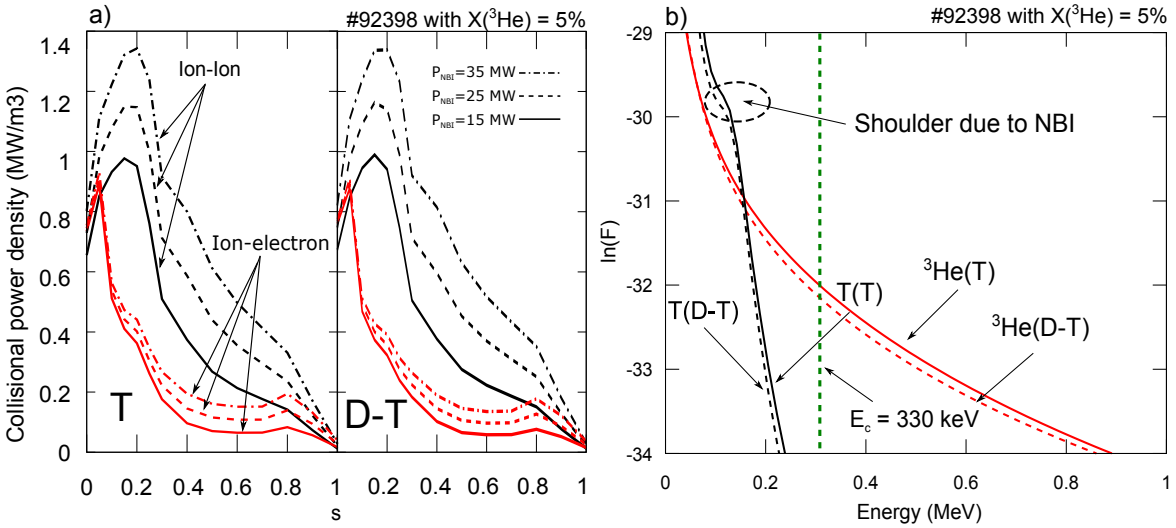

Fig. 7.7 *a) Profile of collisional power for ion-ion collisions (black) and ion-electron collisions (red) for three different P_{NBI}, 15 MW (solid), 25 MW (dashed) and 35 MW (dash-dotted) for T and D-T scenarios for discharge 92398. b) Detail of the velocity distribution function of tritons (black) and ^{3}He (red) around the critical energy for T (solid) and D-T (dashed) scenarios for discharge 92398.*

7.4 Hybrid and baseline scenarios differences

The modelling presented in this chapter addresses the hybrid scenario, however, the modelling has also been carried out for a record baseline shot (92436). Baseline results are not shown as differences are found to be small, thus it has been considered that summarising these differences is more appropriate for the present text.

From the heating point of view, these differences arise mainly by a higher plasma temperature and plasma density in 92398. The higher plasma temperature favours bulk ion heating which in the hybrid scenario is roughly 5% greater for the volume integrated total and 0.3-0.4 MW/m^3 higher at the plasma center. Notice that the

plasma current is higher in the baseline scenario which also reduces beam penetration. These results are summarised in table 7.2 for the $P_{NBI} = 15$ MW case. Notice that apart from the D-T and T scenarios, the T-He (50%-25%) case has also been modelled which gives excellent results for extrapolation to D-T as profile results are also very similar.

	92398			92436		
	D-T	T	T-He	D-T	T	T-He
ICRF ion absorption (MW)	4.1	4.9	4.0	3.5	4.8	3.5
Direct electron absorption (MW)	1.9	1.1	2.0	2.5	1.2	2.5
Bulk ion heating (MW)	12.9	13.3	12.8	12.0	12.7	11.9
Ion-electron heating (MW)	6.2	6.6	6.3	6.5	7.1	6.6
Fast ion energy content (MJ)	1.9	2.1	1.9	1.4	1.7	1.4
Central average fast ion energy (keV)	340	200	340	350	200	360

Table 7.2 Summary of volume integrated heating parameters for hybrid and baseline scenarios for the pure 2^{nd} T harmonic scenario with $P_{NBI} = 15$.

7.5 Conclusions

From the heating point of view, PION predicts for both the pure 2^{nd} T harmonic and ^{3}He minority heating schemes good ICRF central heating in T and D-T. The main difference between T and D-T scenarios arise from their different T content in the plasma when the 2^{nd} T harmonic heating scheme is considered. This has an important impact in the velocity distribution function of resonant tritons, effectively increasing central bulk ion heating in the T scenario. However, ion-electron collisions are predicted to be similar in T and D-T which might lead to similar ICRF control of central impurity accumulation. Regarding the ^{3}He minority scheme, ^{3}He is a strong absorber which leaves a small percentage of the wave energy to T absorption. In this scenario there is a strong heating similarity between T and D-T scenarios. However, the generation of a strong T tail is not possible with this scheme and needs to be studied in plasmas without ^{3}He in preparation of JET D-T campaign and ITER.

Chapter 8

Conclusions

The use of codes such as the main code used in this thesis, PION, becomes crucial not only to understand and analyse the underlying physics in fusion experiments but also to prepare new ones. Therefore, simulations are contrasted with experiments to validate the present models and improve the reliability of the modelling results. This thesis reports on the modelling study of plasma heating through ICRF waves and NBI for recent experiments at the Joint European Torus (JET).

During the 2015-2019 JET campaigns many efforts have been devoted to the exploration of high-performance plasma scenarios envisaged for D-T operation in JET. Experiments in D, H and T are expected to lead in 2020 to the first experiments with 50%:50% D-T mixtures since 1997. In order to mimic plasma conditions as in the International Thermonuclear Experimental Reactor (ITER), JET has been upgraded with the so-called ITER-like-wall (ILW) which is made of tungsten and beryllium. The last campaigns at JET have been focused on enhancing the fusion performance of the baseline and hybrid scenarios with the final goal of improving ITER's future operation. For this reason, the second D-T campaign at JET will be of special relevance and will pave the way for the future experiments in ITER.

On this basis, this thesis provides valuable insight on how to optimise plasma performance through plasma heating for different schemes. The results shown in this thesis serve as a guideline for maximising fusion yield by means of properly configuring several plasma heating schemes. These guidelines are being used in the present JET campaign. The following is a summary of the results obtained.

With the ITER-like-wall consisting of high-Z elements, one of the key aspects to achieving high-performance conditions is the capability to control impurities in order to avoid disruptions and high radiation losses. The experiments shown in this thesis were designed to place the resonance position at different locations which showed the

inability to control impurities when the resonance was placed too off-axis either on the LFS or the HFS. The modelling results show that only central heating provides the greatest density power peak and the largest ion-electron heating. Both effects are beneficial for peaking the electron temperature (through ion-electron collisions) and for flattening the central density profile. Both are crucial to avoid central impurity accumulation.

Off-axis experiments performed poorly in terms of impurity control as temperature and density profiles could not reach the desired shape. Moreover, they eventually were dominated by MHD activity and important radiation losses until disruption of the discharge. However, it is important to mention that HFS deposition proved to be an interesting scheme with an improved performance until the appearance of the MHD activity. The conclusion from this study is that under this hybrid configuration in order to avoid MHD activity and impurity accumulation, the ICRF resonance must be placed in a region around $|R_{res} - R_0| \leq 15$ cm, i.e., central deposition, in accordance with other impurity control studies.

For the impurity control study, the PION code which takes into account finite orbit widths (FOW) was updated to compute the impurity screening due to fast resonant ions. As opposed to previous studies such as in [19, 22] the fast ion contribution to fast ion temperature screening was found to be small as compared to the background plasma and their contribution could be neglected. When FOW are taken into account, the temperature profile of fast ions tends to broaden which effectively decreases the temperature gradient. This single effect is enough to drastically reduce fast ions contribution to impurity control and lead to optimistic results in previous studies without FOW. Moreover, heating off-axis makes fast ions to contribute negatively to the impurity screening. The contribution to impurity screening from D beams was also found to be small since the effective temperature remains flat with no gradient.

Experiments with H minority scheme ($\omega = \omega_{cH} = 2\omega_{cD}$) showed the capability of boosting the neutron rate by 20% by varying the H minority concentration. Good agreement was found between PION and experimental results. It was shown that by reducing the H concentration more power was being channeled to D. As D fusion cross section peaks at the MeV range of energies, producing an ICRF induced energetic tail in a D-D plasma is beneficial for fusion yield. This effect was supported experimentally with the TOFOR diagnostic where the experimental distribution functions of D showed a stronger tail for lower H minority concentrations.

During this campaign a high-performance discharge reached a new fusion record of $2.7 \cdot 10^{16}$ s^{-1}. A detailed analysis of this particular discharge was made with PION and

we obtained an excellent agreement with the experimental results. It was confirmed that bulk ion heating and channeling the ICRF power to D played a major role in enhancing neutron production. The ICRF fusion enhancement was computed to be about 15% of the total neutrons produced during the steady state. This enhancement was found to be reduced by increasing the plasma density and temperature as they increase thermal reactions and also with the injection of D beams. However, this result could not be directly extrapolated to the D-T case as the D-T fusion cross section peaks at 120 keV which invalidates the strategy of maximising the power to D. An equivalent D-T power of 7 MW was calculated.

The prediction or extrapolation of the physics and plasma performance of a particular discharge became a crucial exercise during the last JET campaigns. This study allows to predict the plasma performance for a reference discharge under variations of the starting conditions, such as plasma composition and heating power. The main interest lies on the prediction of the equivalent D-T plasma of previous D-D plasma campaigns and its performance assuming maximum power available at JET. Two assessments have been made for two different minority ICRF schemes, H and ^{3}He minority. The first assessment consisting of a study at maximum power available in a D-D plasma using the integrated modelling tool JETTO and the second consisting of the same prediction but for a D-T plasma using PION.

For the D-D case, the neutron production rate increased by a factor of 2-3 during the high-performance phase of the original shot while the power was scaled by a factor of only 1.48. The prediction shows a higher bulk temperature achieved by ^{3}He, 16 keV as compared to 12 keV reached by H, as a result of its higher critical energy. However, while in the ^{3}He minority scenario ($\omega = \omega_{c^3He}$) all the fusion reactions rely on thermal-thermal reactions, in the H minority scenario ($\omega = \omega_{cH} = 2\omega_{cD}$) the 2$^{\text{nd}}$ D harmonic heating produces an energetic tail in the D velocity distribution further enhancing the fusion rate beyond thermal reactions. This enhancement increased the fusion reactions in the H minority scenario beyond those in the ^{3}He minority scenario during the low-performance phase.

The D-T extrapolation also consisted of a scan in two plasma parameters, plasma temperature and density. This analysis allows to predict the heating efficiency in a wide range of temperatures and densities. Both minority schemes, H and ^{3}He showed good ion power absorption, 60-87% and 73-90%, respectively. Power absorption has a strong dependence on both parameters, plasma density and temperature as both tend to increase direct electron damping while reducing ion absorption. The study of bulk ion heating shows strong differences with regards to heating with NBI or NBI+ICRH as

the ICRH addition changes substantially the velocity distribution functions of resonant ions. In general terms ^{3}He minority offers higher energy transfer to background ions ranging from 10 to 20% of the total input power for resonant ions as compared to H minority. This difference is reduced for higher temperatures and lower densities as the H critical energy increases and the direct electron damping becomes reduced. Regarding the ICRF fusion enhancement, it ranges from 2-9% for H and from 0.5-2% for ^{3}He. This difference between both minority scenarios lies in the stronger 2$^{\text{nd}}$ D harmonic absorption as compared to that of T in the ^{3}He scenario. ICRF fusion enhancement for D-T plasmas is considerably lower than in D-D plasmas mainly because of D-D fusion cross section peaking at the MeV range which is beneficial for ICRF heating.

Before the second D-T campaign at JET, a T campaign will be carried out. The goal is that experiments in a full T plasma mimic the same plasma heating physics of a D-T plasma. For that, it is important to understand what differences and similarities are expected. An analysis performed with PION shows the results in terms of plasma heating that have been found for both scenarios. The ICRF schemes analysed are ^{3}He minority ($\omega = \omega_{c^3He} = 2\omega_{cT}$) and the most promising scheme for ITER, the 2$^{\text{nd}}$ T harmonic heating scheme ($\omega = 2\omega_{cT}$).

Both ICRF schemes, the pure 2$^{\text{nd}}$ T harmonic and ^{3}He minority heating, show good central ion absorption in T and D-T, as predicted by PION. Regarding the ^{3}He minority scheme, the damping strength of ^{3}He leaves a small percentage of the wave's energy to the 2$^{\text{nd}}$ T harmonic heating. This is the reason why this scenario offers a large heating similarity between T and D-T. Nevertheless, as T absorption is low under these conditions, no energetic T tail can be developed with this scheme, which is a topic relevant for ITER. Therefore, the pure 2$^{\text{nd}}$ T harmonic scheme needs to be tested.

For the pure 2$^{\text{nd}}$ T harmonic scheme, the T density in each scenario plays a crucial role. The T velocity distribution function is higher around the critical energy for higher T density, while a stronger energetic tail is obtained for lower T densities. This fact leads to higher central bulk ion heating for higher T densities. However, ion-electron collisions are predicted to be similar in T and D-T which might lead to similar ICRF control of central impurity accumulation.

The overall conclusion is that this thesis gives a guideline to the optimisation of several ICRF schemes in order to boost the fusion performance in hybrid discharges and assess its extrapolation to D-T scenarios. The study of the results obtained shows the reason of this improved performance such as the impurity control using ICRF waves, the role of H concentration or the ICRF fusion rate enhancement. The strategy described to boost the fusion rate for D plasmas has proven to be valid in JET

experiments and has contributed to get closer to the D-T ready plasma goal. However, this strategy does not directly extrapolate to D-T scenarios. The analysis of a D-T prediction for a scan in plasma density and temperature for two different ICRF schemes shows that the ICRF fusion rate enhancement is substantially lowered as compared to the D scenario. The reason is that the D-T fusion cross section peaks at a much lower energy range as compared to the D-D one and the highly energetic ions created by the ICRF waves might lower the fusion performance. Finally, a prediction study from D plasmas to T and D-T plasmas has been given, which highlights the similarities and differences expected from the heating point of view. This is specially important for the forthcoming campaigns at JET where heating schemes are sought in order to easily extrapolate from D and T plasmas to D-T ones before the actual D-T experiments. The results of this thesis support the good progress towards the optimisation of fusion performance shown by the last experimental campaigns at JET.

8.1 Future work to be done

A D campaign is presently being carried out at JET. After that, a T campaign will take place before concluding in the D-T experiments. There is a big amount of work to be performed apart from analysing specific discharges. In particular, I am specially interested in the performance of the ^{3}He minority scheme in D plasmas. This scheme has just been started to be used in the present campaign. The modelling shows high ion temperature as a result of strong bulk ion heating which might potentially improve the neutron rate. However, the small collisional power to electrons might lead to impurity accumulation and, therefore, degraded performance. This needs to be confirmed experimentally.

There are two issues that were not tackled in this thesis which are relevant for the next D-T campaign. First, a promising ICRF scheme, the D minority in a T plasma, showed strong performance in the previous D-T campaign at JET [12]. Nevertheless, its performance degraded beyond D concentrations higher than 15%. This is still not well understood, it was proposed that Be and mode-conversion were the main culprits but it needs to be confirmed. Second, the role of fusion-born alpha particles needs to be assessed. It is mandatory to find ICRF schemes that do not *screen* the alpha particle effects. This is in practice obtained by preventing the fast ion pressure and collisional power to electrons from ICRF-driven fast ions to be substantially lower than that from fusion-born alphas. There are a number of ideas proposed for this, as for example, using the ^{3}He minority scheme [29].

These are going to be interesting times at JET with several campaigns taking place to study the isotope effect and finalising in the D-T experiments. I will work closely following several experiments and try to keep improving the plasma performance specially in preparation for the D-T plasmas.

References

[1] J. Freidberg. *Theory of Fusion Plasmas*. Cambridge University Press, New York, 2007.

[2] J. Wesson. *Tokamaks*. Oxford Science Publications, Oxford, 1997.

[3] J. Ongena et al. Energy for Future Centuries: Prospects for Fusion Power as a Future Energy Source. *Fusion Science and Technology*, 61:2T, 2012.

[4] P. Debye et al. The theory of electrolytes. I. Freezing point depression and related phenomenon. *Physikalische Zeitschrift*, 1923.

[5] S.Pfalzner. *An Introduction to Inertial Confinement Fusion*. Taylor and Francis Group, London, 2006.

[6] M. Watatani. *Stellarator and Heliotron Devices*. Oxford University Press, Oxford, 1996.

[7] J.M. Noterdaeme et al. Physics studies with the additional heating systems in JET. *Fusion Science and Technology*, 53(4):1103–1151, 2008.

[8] J. Ongena et al. Magnetic-confinement fusion. *Nature Physics*, 12(5):398, 2016.

[9] H. Zohm. On the size of tokamak fusion power plants. *Phil. Trans. R. Soc. A*, 377:20170437, 2019.

[10] L. Spitzer et al. The Electrical Conductivity of an Ionized Gas. *Physical Review*, 80 (2):230–238, 1950.

[11] L.-G. Eriksson et al. Theoretical analysis of ICRF heating in JET DT plasmas. *Nuclear Fusion*, 39:337, 1999.

[12] D.F.H. Start et al. D-T Fusion with Ion Cyclotron Resonance Heating in the JET Tokamak. *Physical Review Letters*, 80:4681, 1998.

[13] D.F.H. Start et al. Bulk ion heating with ICRH in JET D-T plasmas. *Nuclear Fusion*, 39:321–336, 1999.

[14] J. Garcia et al. Challenges in the extrapolation from DD to DT plasmas: experimental analysis and theory based predictions for JET-DT. *Plasma Physics and Controlled Fusion*, 59:014023, 2017.

[15] T. Casper et al. Development of the ITER baseline inductive scenario. *Nuclear Fusion*, 54:1 013005, 2014.

[16] C. Gormezano et al. Chapter 4: Advanced Tokamak Scenario Development at JET. *Fusion Science and Technology*, 53:958, 2008.

[17] X. Litaudon et al. Overview of the JET results in support to ITER. *Nuclear Fusion*, 57:102001, 2017.

[18] M. Mantsinen et al. Optimising the use of ICRF waves in JET hybrid plasmas for high fusion yield. *44th EPS Conference on Plasma Physics*, 41F:O3, 2017.

[19] F.J. Casson et al. Theoretical description of heavy impurity transport and its application to the modelling of tungsten in JET and ASDEX upgrade. *Plasma Physics and Controlled Fusion*, 57:014031, 2015.

[20] F. Casson et al. Predictive multi-channel flux-driven modelling to optimise ICRH tungsten control in JET. *submitted to Nuclear Fusion*, 2019.

[21] M. Goniche et al. Optimization of ICRH for tungsten control in JET H-mode plasmas. *Europhysics Conference Abstracts*, 38F:O4.129, 2014.

[22] M. Goniche et al. Ion cyclotron resonance heating for tungsten control in various JET H-mode scenarios. *Plasma Physics and Controlled Fusion*, 59:055001, 2017.

[23] E. Lerche et al. Optimization of ICRH for core impurity control in JET-ILW. *Nuclear Fusion*, 3:036022, 2016.

[24] M. Mantsinen et al. Analysis of bulk ion heating with ICRH in JET high-performance plasmas. *Plasma Physics and Controlled Fusion*, 41:843, 1999.

[25] G.A. Cottrell et al. Ion cyclotron heating of JET DD and DT optimized shear plasmas. *Nuclear Fusion*, 39:389, 1999.

[26] D. Anderson et al. Bulk ion heating with ICRH in JET D-T plasmas. *Plasma Physics, Controlled Fusion*, 29:891, 1987.

[27] R.W. Harvey et al. ICRF fusion reactivity enhancement in tokamaks. *Nuclear Fusion*, 26:1 43, 1986.

[28] V.B. Krapchev et al. Enhancement of the reaction rate by ICRF heating. *Nuclear Fusion*, 25:4 455, 1985.

[29] J. Garcia et al. First principles and integrated modelling achievements towards trustful fusion power predictions for JET and ITER. *Nuclear Fusion*, 59:086047, 2019.

[30] T. H. Stix. *Plasma Waves*. American Institute of Physics, New York, 1992.

[31] Ye. O. Kazakov et al. On resonant ICRF absorption in three-ion component plasmas: a new promising tool for fast ion generation. *Nuclear Fusion*, 55:032001, 2015.

[32] Ye. O. Kazakov et al. A new ion cyclotron range of frequency scenario for bulk ion heating in deuterium-tritium plasmas: How to utilize intrinsic impurities in our favour. *Physics of Plasmas*, 22:082511, 2015.

[33] M. J. Mantsinen. *Development and Experimental Evaluation of Theoretical Models for Ion Cyclotron Resonance Frequency Heating of Tokamak Plasmas*. PhD thesis, Helsinki University of Technology, Department of Engineering Physics and Mathematics, Espoo, Finland, 1999.

[34] L.-G. Eriksson et al. Monte Carlo operators for orbit-averaged Fokker–Planck equations. *Physics of Plasmas*, 1:308, 1994.

[35] *Course notes on plasma physics*. IPP Max Planck, Munich, 2014.

[36] T.H. Stix et al. Heating of toroidal plasmas by neutral injection. *Plasma Physics*, 14:367, 1972.

[37] M. Brambilla. *Kinetic Theory of Plasma Waves and Homogeneous Plasmas*. Oxford Science Publications, Clarendon Press, Oxford, 1998.

[38] K.G. Budden. *Radio Waves in the Ionosphere*. Cambridge University Press, Cambridge, 1961.

[39] T. H. Stix. Fast Wave Heating of a Two-Component Plasma. *Nuclear Fusion*, 15:737, 1975.

[40] L.-G. Eriksson et al. On the orbit-averaged Monte Carlo operator describing ion cyclotron resonance frequency wave-particle interaction in a tokamak. *Physics of Plasmas*, 6:513–518, 1998.

[41] L.-G. Eriksson et al. Comparison of time dependent simulations with experiment in ion cyclotron heated plasmas. *Nuclear Fusion*, 33:1037, 1993.

[42] M.J. Mantsinen et al. Alpha-tail production with ion-cyclotron-resonance heating of 4he-beam ions in jet plasmas. *Physical Review Letters*, 88:10 105002, 2002.

[43] A. Salmi et al. JET experiments to assess the clamping of the fast ion energy distribution during ICRF heating due to finite Larmor radius effects. *Plasma Physics and Controlled Fusion*, 48(6):717, 2006.

[44] M.J. Mantsinen et al. First observation of pT fusion in JET tritium plasmas with ICRF heating of protons. *Nuclear Fusion*, 41(12):1815, 2001.

[45] D. Gallart et al. Modelling of JET hybrid plasmas with emphasis on performance of combined ICRF and NBI heating. *Nuclear Fusion*, 58:106037, 2018.

[46] M.J. Mantsinen et al. Bulk ion heating with ICRF waves in tokamaks. *AIP Conference Proceedings*, 1689:030005, 2015.

[47] M.J. Mantsinen et al. Third harmonic ICRF heating of deuterium beam ions on ASDEX Upgrade. *43rd EPS Conference on Plasma Physics*, 40A:030005, 2016.

[48] M. García-Muñoz et al. Fast ion losses due to high-frequency MHD perturbations in the ASDEX upgrade tokamak. *Physical Review Letters*, 100(5):055005, 2008.

[49] S.E. Sharapov et al. The effects of electron cyclotron heating and current drive on toroidal Alfvén eigenmodes in tokamak plasmas. *Plasma Physics and Controlled Fusion*, 60(1):014026, 2017.

[50] L.-G. Eriksson et al. On the role of ion heating in ICRF heated discharges in Tore Supra. *Physics of Plasmas*, 24:022122, 2017.

[51] A. Becoulet et al. Heating and Current Drive System for Tore Supra Steady-State Operation. *J. Plasma Fusion Res. SERIES*, 3:51–57, 2000.

[52] M. J. Mantsinen et al. Analysis of combined fast wave current drive and neutral beam injection in the DIII-D tokamak. *Physics of Plasmas*, 9:1318, 2002.

[53] V. Bergeaud et al. ITER relevant ICRF heating scenarios with large ion heating fraction. *Nuclear Fusion*, 40:35, 2000.

[54] D. Van Eester et al. Re-evaluation of ITER ion cyclotron operating scenarios. *Nuclear Fusion*, 42:310, 2002.

[55] D. Gallart et al. Modelling of ICRF heating in DEMO with special emphasis on bulk ion heating. *AIP Conference Proceedings*, 1689:060004, 2015.

[56] T. Hellsten et al. Power deposition for ion cyclotron heating in large tokamaks. *Nuclear Fusion*, 28:285, 1988.

[57] L. Villard. Global waves in cold plasmas. *Computer Physics Reports*, 4:95, 1986.

[58] X. Llobet et al. *Theory of Fusion Plasmas*. Editrice Compositori, Bologna, 1996.

[59] T. Hellsten et al. A modelling scheme for the direct electron heating profiles during ion cyclotron resonance heating. *Nuclear Fusion*, 29:2165, 1989.

[60] T. Hellsten. A statistical model of the wave field in bounded domain. *Physics of Plasmas*, 24:022122, 2017.

[61] S. Succi et al. Computational models for wave-particle interactions. *Computer Physics Communications*, 40:137, 1986.

[62] L.-G. Eriksson et al. A Model for Calculating ICRH Power Deposition and Velocity Distribution. *Physica Scrypta*, 55:70, 1995.

[63] E. Lerche et al. Optimization of ICRH for core impurity control in JET-ILW. *Nuclear Fusion*, 56:036022, 2016.

[64] M.L. Reinke et al. Poloidal variation of high-Z impurity density due to hydrogen minority ion cyclotron resonance heating on Alcator C-Mod. *Plasma Physics and Controlled Fusion*, 54:045004, 2012.

[65] T.C. Hender et al. The role of MHD in causing impurity peaking in JET hybrid plasmas. *Nuclear Fusion*, 56:066002, 2016.

[66] M. Mantsinen et al. The Role of Combined ICRF and NBI Heating in JET Hybrid Plasmas in Quest for High DT Fusion Yield. *European Physical Journal*, 157:03032, 2017.

[67] M. Porkolab et al. Recent progress in ICRF physics. *Plasma Physics and Controlled Fusion*, 40:A35, 1998.

[68] M. Gatu Johnson et al. The 2.5-MeV neutron time-of-flight spectrometer TOFOR for experiments at JET. *Nuclear Instruments and Methods A*, 591:417, 2008.

[69] C. Hellesen et al. Analysis of resonant fast ion distributions during combined ICRF and NBI heating with transients using neutron emission spectroscopy. *Nuclear Instruments and Methods A*, 53:113009, 2013.

[70] C. Hellesen et al. Fast-ion distributions from third harmonic ICRF heating studied with neutron emission spectroscopy. *Nuclear Fusion*, 58:056021, 2018.

[71] C. Hellesen et al. Neutron spectroscopy measurements and modeling of neutral beam heating fast ion dynamics. *Plasma Physics and Controlled Fusion*, 52(8):085013–10, 2010.

[72] D. Gallart et al. Simulations of combined ICRF and NBI heating for high fusion performance in JET. *Europhysics Conference Abstracts*, 40A:P2.003, 2017.

[73] M. Romanelli et al. JINTRAC: A System of Codes for Integrated Simulation of tokamak Scenarios. *Plasma and fusion Research*, 9:3403023, 2014.

[74] M. Mantsinen et al. ICRH analysis of high-performance JET hybrid discharges using PION modelling and neutron spectrometry measurements. *Europhysics Conference Abstracts*, 39E:P2.171, 2015.

[75] D. Gallart et al. Modelling of combined ICRF and NBI heating in JET hybrid plasmas. *European Physical Journal*, 157:03015, 2017.

[76] E. Joffrin et al. Overview of the JET preparation for Deuterium-Tritium Operation. *Nuclear Fusion: IAEA 27th Fusion Energy Conference*, 2018.

[77] K.K. Kirov et al. Fast ion synergistic effects in JET high performance pulses. *Nuclear Fusion*, 59:056005, 2019.

[78] E. Lerche et al. ICRH options for JET-ILW DTE2 operation. *to be published in AIP*, 2019.

[79] P.M. Stubberfield et al. Multiple pencil beam. *JET-DPA*, (06)/87, 1987.

[80] J. Joly et al. Self-consistent modelling of heating synergy between NBI and ICRH in JET deuterium plasmas. *Plasma Physics and Controlled Fusion*, 61:075017, 2019.

Appendix A

Calculation of power absorption ratio

The local ion power absorption is calculated for fundamental and second and third harmonics. This allows us to compare their relative damping strength when several ion damping mechanisms compete in the same discharge. Here the calculation is carried out in 1D for simplicity. The calculation has also been carried out in cylindrical coordinates yielding the same result except for the value of constant factors that are not relevant for this exercise.

The distribution function considered here is a Fokker-Planck distribution in 1D defined as,

$$\frac{\partial f}{\partial t} = Q(f) + C(f), \tag{A.1}$$

where $Q(f)$ is the quasi-linear operator and $C(f)$ is the collisional operator. The 0^{th} moment of the distribution function is defined as:

$$n = \int_{-\infty}^{\infty} f dv \tag{A.2}$$

where n is the ion density of the distribution. The 2^{nd} moment is defined as:

$$W = \frac{m}{2} \int_{-\infty}^{\infty} v^2 f dv, \tag{A.3}$$

where the $m/2$ term has been added to yield the kinetic energy W. Taking the derivative over time,

$$\frac{dW}{dt} = \frac{m}{2} \int_{-\infty}^{\infty} v^2 \frac{df}{dt} dv \implies \frac{m}{2} \int_{-\infty}^{\infty} v^2 Q dv, \tag{A.4}$$

where the definition of the Fokker-Planck distribution (equation A.1) has been used. Notice that the derivative of the velocity has not been performed since it is a coordinate in the phase space and does not depend on space nor time. The RF operator Q is calculated as,

$$\begin{aligned} Q &= \frac{\partial}{\partial v}\left(D_{RF}\frac{\partial f}{\partial v}\right) \\ D_{RF} &\approx \left| J_{n-1}\left(\frac{k_\perp v}{\omega_{ci}}\right) + \frac{E_-}{E_+} J_{n+1}\left(\frac{k_\perp v}{\omega_{ci}}\right)\right|^2, \end{aligned} \tag{A.5}$$

where D_{RF} is the diffusion constant that depends on the Bessel functions of the first kind J_n of order n. The diffusion constant factors have been neglected since we are interested in the ratio of the power absorptions and they cancel out. The Bessel functions can be Taylor expanded as:

$$J_n(x) = \sum_{m=0}^{\infty} \frac{(-1)^m}{m!\Gamma(m+n+1)}\left(\frac{x}{2}\right)^{2m+n}, \tag{A.6}$$

where the gamma function is $\Gamma(n) = (n-1)!$.

The calculation follows as an integration by parts, $\int uv' = uv - \int u'v$ where $u = v^2$, $v' = \frac{\partial}{\partial v}\left(D_{RF}\frac{\partial f}{\partial v}\right)dv$, $u' = 2vdv$, $v = D_{RF}\frac{\partial f}{\partial v}$,

$$\begin{aligned} \int_{-\infty}^{\infty} v^2 \frac{\partial}{\partial v}\left(D_{RF}\frac{\partial f}{\partial v}\right) dv &= \left[v^2 D_{RF}\frac{\partial f}{\partial v}\right]_{-\infty}^{\infty} - \int_{-\infty}^{\infty} 2vD_{RF}\frac{\partial f}{\partial v}dv \\ &= 0 - \int_{-\infty}^{\infty} 2vD_{RF}\frac{\partial f}{\partial v}dv, \end{aligned} \tag{A.7}$$

the first term on the RHS vanishes as the Bessel functions tend to 0 at infinity and any distribution function f and its derivatives should decay at infinity.

A.1 Fundamental absorption

The Bessel functions in the diffusion constant for fundamental heating ($n = 1$) assuming small values of $x << 1$ ($x = k_\perp v/\omega_{ci}$) where k is the wavenumber, can be expressed as:

$$\begin{aligned} J_0(x) &\approx \frac{(-1)^0}{0!\Gamma(1)}\left(\frac{x}{2}\right)^0 = 1 \\ J_2(x) &\approx \frac{(-1)^0}{0!\Gamma(3)}\left(\frac{x}{2}\right)^2 = \frac{1}{2!}\frac{x^2}{4}, \end{aligned}$$

J_2 is neglected and $D_{RF} \approx 1$. Substituting in equation A.7 and integrating by parts, $u = 2v$, $v' = \frac{\partial f}{\partial v} dv$, $u' = 2dv$ and $v = f$,

$$\int_{-\infty}^{\infty} 2vD_{RF} \frac{\partial f}{\partial v} dv = [2vf]_{-\infty}^{\infty} - \int_{-\infty}^{\infty} 2f dv.$$

The first term at the RHS is 0 and the second term is $-2n_H$, the power absorption for fundamental heating is obtained by substituting back these terms,

$$p_1 = \frac{dW}{dt} = \frac{m}{2} \int_0^{\infty} v^2 Q dv = m_i n_i. \tag{A.8}$$

A.2 2nd harmonic absorption

A similar process follows except that now $n = 2$. The Bessel functions in this case give,

$$J_1(x) \approx \frac{(-1)^0}{0!\Gamma(2)} \left(\frac{x}{2}\right) = \frac{x}{2}$$
$$J_3(x) \approx \frac{(-1)^0}{0!\Gamma(4)} \left(\frac{x}{2}\right)^3 = \frac{1}{3!} \frac{x^3}{8},$$

Neglecting J_3, $D_{RF} \approx \frac{k_\perp^2 v^2}{4\omega_{ci}^2}$, substituting in equation A.7,

$$\int_{-\infty}^{\infty} v^3 \frac{k_\perp^2}{2\omega_{ci}^2} \frac{\partial f}{\partial v} dv = \frac{k_\perp^2}{2\omega_{ci}^2} \left[v^3 f\right]_{-\infty}^{\infty} - \frac{3k_\perp^2}{2\omega_{ci}^2} \int_{-\infty}^{\infty} v^2 f dv.$$

The first term on the RHS is 0 and the second term is the second moment of f (equation A.3), substituting back yields,

$$p_2 = \frac{dW}{dt} = \frac{m}{2} \int_0^{\infty} v^2 Q dv = \frac{3k_\perp^2}{2\omega_{ci}^2} W_i \tag{A.9}$$

The ratio for second harmonic absorption and fundamental absorption,

$$\frac{p_2}{p_1} = \frac{\frac{3k_\perp}{2\omega_{c2}^2} W_2}{m_1 n_1} = \frac{3k_\perp^2 W_2}{2n_1 m_1 \omega_{c2}^2} = c \frac{k_\perp^2 W_2}{n_1 m_1 \omega_{c2}^2}, \tag{A.10}$$

where the constant factors have been collected in c as they may vary with the dimensions and coordinates used but are unimportant for the statistical exercise carried out in chapter 5.

A.3 3rd harmonic absorption

For the third harmonic ($n = 3$) the Bessel functions are,

$$J_2(x) \approx \frac{(-1)^0}{0!\Gamma(3)}\left(\frac{x}{2}\right)^2 = \frac{1}{2!}\frac{x^2}{4}$$
$$J_4(x) \approx \frac{(-1)^0}{0!\Gamma(5)}\left(\frac{x}{2}\right)^4 = \frac{1}{4!}\frac{x^4}{16},$$

neglecting J_4 the diffusion constant becomes $D_{RF} \approx \frac{k_\perp^4 v^4}{64\omega_{ci}^4}$. Substituting in equation A.7,

$$-\int_{-\infty}^{\infty} 2vD_{RF}\frac{\partial f}{\partial v}dv = -\frac{k_\perp^4}{32\omega_c^4}\int_{-\infty}^{\infty} v^5\frac{\partial f}{\partial v}dv. \tag{A.11}$$

We can now solve the integral by parts,

$$\int_{-\infty}^{\infty} v^5\frac{\partial f}{\partial v}dv = \left[v^5 f\right]_{-\infty}^{\infty} - 5\int_{-\infty}^{\infty} v^4 f dv, \tag{A.12}$$

which yields,

$$p_3 = \frac{dW}{dt} = \frac{5m_i k_\perp^4}{32\omega_c^4}\int_{-\infty}^{\infty} v^4 f dv. \tag{A.13}$$

The ratio between third harmonic and fundamental or second harmonic is,

$$\begin{aligned}\frac{p_3}{p_1} &= c\frac{m_3 k_\perp^4}{m_1 n_1 \omega_{c3}^4}\int_{-\infty}^{\infty} v_3^4 f_3 dv \\ \frac{p_3}{p_2} &= c\frac{m_3 k_\perp^2 \omega_{c2}^2}{\omega_{c3}^4 W_2}\int_{-\infty}^{\infty} v_3^4 f_3 dv\end{aligned} \tag{A.14}$$